Functional Optical Coherence Tomography:

In Vivo Applications in Dermatology and Neuroscience

Utku Baran

A dissertation

submitted in partial fulfillment of the

requirements for the degree of

Doctor of Philosophy

University of Washington

2016

Reading Committee:

Ruikang K. Wang, Chair

Lih Y. Lin

Eric J. Seibel

Program Authorized to Offer Degree:

Electrical Engineering

University of Washington

Abstract

Functional Optical Coherence Tomography:

In Vivo Applications in Dermatology and Neuroscience

Utku Baran

Chair of the Supervisory Committee:

Professor Ruikang K. Wang

Bioengineering

Optical coherence tomography (OCT) is a revolutionary imaging technique commonly used in ophthalmology, and on its way to become a major tool in clinical dermatology and neuroscience. In this thesis, the non-invasive imaging capabilities of functional OCT are demonstrated in label-free detection of high-resolution, three-dimensional structural and microvascular features of *in vivo* human skin and mouse cerebral cortex, with various conditions. Moreover, new label-free methods for tissue injury mapping (TIM) and OCT-based lymphangiography (OLAG) with a clinical prospect are proposed. Based on the results, functional OCT is promising to become an indispensable, yet cost effective tool to monitor changes in tissue morphology and hemodynamics for diagnosis of various diseases or for following pharmacological interventions.

TABLE OF CONTENTS

TABLE OF CONTENTS iv

List of Figures 7

List of Journal Publications 8

Acknowledgements 9

Chapter 1. Introduction 12

1.1 Optical Coherence Tomography (OCT) 12

1.1.1 Spectral Domain OCT (SD-OCT) 13

1.1.2 Swept-Source OCT (SS-OCT) 15

1.2 OCT Angiography 16

1.2.1 Complex Signal Based Methods 16

1.2.2 Phase-based Methods 18

1.2.3 Intensity-based Methods 19

1.2.4 Capillary Flux and Velocity Mapping Methods 20

Chapter 2. New Algorithms and Methods for OCT 23

2.1 Tissue Injury Mapping (TIM) 23

2.1.1 Background and Motivation 23

2.1.2 System Description 24

2.1.3 Optical Attenuation Coefficient (OAC) Mapping 24

2.1.4 Contrast comparison between OAC mapping methods 27

2.1.5 Discussion and Conclusion 29

2.2 OCT-based Lymphangiography (OLAG) 31

2.2.1 Background and Motivation 31
2.2.2 System Description 32
2.2.3 Details of OLAG Protocol 33
2.2.4 Results 39
2.2.5 Discussion and Conclusion 41
Chapter 3. Functional OCT in Clinical Dermatology 44
3.1 Background and Motivation 44
3.2 System Description 45
3.3 OCT Imaging of Healthy Human Skin In Vivo 48
3.3.1 OCT Imaging of Human Nailfold 48
3.3.2 OCT Imaging of Human Facial Skin 49
3.4 OCT Imaging of Inflamed Human Skin In Vivo 51
3.5 High Resolution Imaging of Pathological Human Skin 54
3.5.1 OCT Imaging on Pathological Skin at Various Parts of Human Body 54
3.5.2 Monitoring Acne Development and Scarring on human skin 56
3.5.3 Monitoring Wound Healing on human skin 58
3.6 Discussion and Conclusion 60
Chapter 4. Functional OCT in Neuroscience 62
4.1 Review of OCT-Based Angiography Methods for Neuroscience 62
4.1.1 OCT Imaging of Healthy Rodent Brain 62
4.1.2 OCT Imaging of Rodent Brain during Stroke 65
4.1.3 OCT Imaging of Rodent Brain after Injury 67
4.2 Comparison of Cranial Window Implementations for OMAG 69

4.2.1 Background and Motivation 69
4.2.2 System and Methods 70
4.2.3 Results 74
4.2.4 Discussion and Conclusion 79
4.3 Vasodynamics of Cerebral Arterioles after Stroke 82
4.3.1 Background and Motivation 82
4.3.2 System and Methods 84
4.3.3 Results 87
4.3.4 Discussion and Conclusion 94
Chapter 5. Summary And Future Work 97
Bibliography 101

LIST OF FIGURES

Figure 1.1. A common setup of a spectral-domain OCT system. 14
Figure 1.2. A common setup of a swept-source OCT system. 15
Figure 2.1. OMAG, OCT structural and OAC mapping images during stroke. 25
Figure 2.2. Contrast comparison between various OAC mapping methods. 28
Figure 2.3. OLAG protocol for mapping lymphatic vessels within human dermis. 34
Figure 2.4. In vivo mouse ear imaging using OMAG and OLAG 35
Figure 2.5. En face mapping of lymphatic vessels within human lower arm skin 40
Figure 2.6. En face mapping of lymphatic vessels within human areola 41
Figure 3.1. Swept-source OCT system for in vivo human skin imaging. 46
Figure 3.2. OCT imaging of healthy human nailfold *in vivo*. 49
Figure 3.3. OCT imaging of healthy human facial skin *in vivo*. 50
Figure 3.4. Monitoring inflamed human skin *in vivo* using OLAG and OMAG. 51
Figure 3.5. Monitoring healing human skin *in vivo* using OLAG and OMAG. 52
Figure 3.6. OCT imaging of different skin lesions on human body *in vivo*. 55
Figure 3.7. Monitoring development of acne lesion over 51 days *in vivo* using OMAG. 57
Figure 3.8. OCT imaging of wound healing within human skin over 10 days *in vivo*. 58
Figure 4.1. Microscopic images of skull before and after cranial windows comparison. 72
Figure 4.2. OMAG MIP view of microcirculation network up to 1 mm depth. 75
Figure 4.3. Cross-sectional and MIP views of OMAG images through cranial windows.76
Figure 4.4. DOMAG MIP view of microcirculation network at 50–450 mm depth. 77
Figure 4.5. Vessel density comparison and total blood flow quantification. 78
Figure 4.6. Pial and Penetrating Arteriole Vasodynamics under Basal Conditions. 88
Figure 4.7. Pial and Penetrating Arteriole Vasodynamics during MCAO and reperfusion.90
Figure 4.8. The lumen diameter changes in the pial arterioles during stroke. 91
Figure 4.9. Comparison between regions where AAA is relatively stronger or weaker. . 92
Figure 4.10. Lumen diameter, RBC velocity and total blood flow comparison. 93

LIST OF JOURNAL PUBLICATIONS

Part of this dissertation has been published in the selected journal papers from the list below.

*: Equally Contributed Authors.

[1] **U. Baran***, E. Swanson* et al. "OCT-based microangiography for reactive hypermia studies within residual limb skin of amputees" (in preparation)

[2] **U. Baran**, et al. "Automated layer segmentation and enhancement of optical coherence tomography images of rodent cerebral cortex" (under review)

[3] **U. Baran**, et al. "Video-rate volumetric OCT-based angiography" Optical Engineering (2016)

[4] W. Wei, J. Xu, **U. Baran** et al. "Inter-volume analysis to achieve 4D optical micro-angiography for observation of dynamic blood flow" Journal of Biomedical Optics (2016)

[5] **U. Baran**, et al. "OCT based label-free in vivo lymphangiography within human skin and areola" Scientific Reports (2016) (*Partly used in Chapter 3 of this dissertation*)

[6] **U. Baran**, R. K. Wang, "Review of optical coherence tomography based angiography in neuroscience" Neurophotonics (2016) (*Partly used in Chapter 1 and 4 of this dissertation*)

[7] **U. Baran**, et al. "High resolution monitoring of acne lesion development on human face using optical coherence tomography", Lasers in Surgery and Medicine (2015) (*Partly used in Chapter 3 of this dissertation*)

[8] **U. Baran***, Y. Li*, and R.K. Wang, "Vasodynamics of pial and penetrating arterioles after focal stroke" Neurophotonics (2015) (*Partly used in Chapter 4 of this dissertation*)

[9] **U. Baran**, et al. "In vivo tissue injury mapping using OCT based methods", Applied Optics (2015) (*Partly used in Chapter 2 this dissertation*)

[10] **U. Baran***, WJ. Choi*, R.K. Wang, "Potential use of OCT-based microangiography in clinical dermatology", Skin Research and Technology (2015) (*Partly used in Chapter 3 of this dissertation*)

[11] W. Qin, **U. Baran**, R.K. Wang, "Lymphatic response to depilation-induced inflammation in mouse ear assessed with label-free optical lymphangiography", Lasers in Surgery and Medicine (2015)

[12] H. Wang*, **U. Baran***, R.K. Wang, "In vivo blood flow imaging of inflammatory human skin induced by tape stripping using optical microangiography", Journal of Biophotonics, (2014) (Editor's Choice)

[13] Y. Li*, **U. Baran***, R.K. Wang, "Application of thinned-skull cranial window to mouse cerebral blood flow imaging using optical microangiography", PLoS One (2014) (*Partly used in Chapter 4 of this dissertation*)

[14] H. Wang, **U. Baran**, et al. "Does optical micro-angiography provide accurate imaging of capillary vessels – validation using multiphoton microscopy", Journal of Biomedical Optics (2014)

[15] R. Reif, **U. Baran**, and R. K. Wang, "Motion artifact and background noise suppression on optical microangiography frames using a naïve Bayes mask" Applied Optics (2014)

[16] **U. Baran**, L. Shi, and R.K. Wang, "Capillary blood flow imaging within human finger cuticle using optical microangiography", Journal of Biophotonics (2013)

ACKNOWLEDGEMENTS

I cannot express how much I appreciate having this opportunity to be mentored by Prof. Ruikang K. Wang during my PhD studies. Although my previous background was not directly related to his research area, he trusted in my potential, provided me an adequate training, and patiently listened to my questions that I enthusiastically bugged him with. I always had the freedom to feed my curiosity by using the abundant resources in our lab, which sometimes led to interesting findings. He has always been supportive and nominated me for several awards without any reservations. My PhD experience and outcome would have been dramatically different if I was not a part of his group in bioengineering department.

I would like to thank my PhD dissertation committee members who spent their valuable time to review my work. Prof. Lih Y. Lin and Prof. Eric J. Seibel had to read and correct all of the >100 pages of my thesis. Also, Prof. Anant Anantram and Prof. Helen Sherk (GSR member) made room in their busy schedule to attend my final exam.

I sincerely extend my best regards to my colleagues and lab members. Particularly, Ms. Yuandong Li and Dr. Woo June Choi were instrumental partners and they deserve a significant credit for this dissertation. Dr. Siavash Yousefi was always helpful to me in every way, shared his life experience and knowledge. Dr. Lei Shi, Mr. Wei Wei and Dr. Shaozhen Song helped me modify and maintain our systems. Dr. Roberto Reif was a great mentor in my early days in the lab and we always had interesting discussions. I was also lucky to collaborate with and learn from clinical researchers Dr. Wenbin Zhu, Dr. Wenri Zhang, Ms. Kirsti Golgotiu, and Prof. Nabil Alkayed from OHSU and Mr. Jack Yang, Dr. Nishijama Nasu, and Prof. Jialing Liu from UCSF.

I want to highlight all the training and guidance I got from my former mentors Prof. Hakan Urey from Koc University and Dr. Wyatt Davis from Microvision. They have been indispensable in my early career and I owe them a lifelong gratitude for their support and mentorship.

Last but not the least, my mother, Dr. Pervin Baran, deserves my utmost appreciation. It has been a long journey for us starting from my childhood in Ankara and all of this would not be possible without her sacrifices and unlimited support as a single mother. I am also blessed with love and support from all Baran family relatives, especially Prof. Abdullah Baran, Ms. Hayriye Baran, Ms. Beyhan Baran, Mr. Suleyman Baran, Mr. Turhan Baran, Dr. Nermin Baran, and Dr. Mesut Baran. It was my inspiration to make them proud.

To my dear mother,

Chapter 1. INTRODUCTION

1.1 Optical Coherence Tomography (OCT)

Optical coherence tomography (OCT) is a non-invasive method for in vivo volumetric imaging of biological tissues with high resolution (<10μm) without administration of contrast agents (Tomlins and Wang 2005). OCT can image up to a depth of several millimeters, at an imaging speed up to 1.6 MHz (line scan rate) (Wieser et al. 2014). Human eye is a great sample for OCT imaging due to its relatively transparent optical properties. Accordingly, ophthalmology field has been revolutionized by benefiting from desirable in vivo capabilities of OCT imaging in the last decade. In vivo structural and functional OCT imaging of posterior (Wang et al. 2010) and anterior segments of the eye (Choi et al. 2014b) have been proven useful both in clinical and research settings. Other emerging applications of OCT are endoscopic imaging, dermatology and rodent cerebral cortex imaging, among many others.

Currently, there are two types of OCT implementations, the time-domain OCT (Drexler et al. 1999) and the Fourier domain OCT (FD-OCT) (Wojtkowski et al. 2004). FD-OCT brings distinct advantages in its sensitivity and imaging speed as compared to its time-domain counterpart (Leitgeb et al. 2003). Even though the idea of using OCT in biomedical imaging applications was proposed in the 1990's (Huang et al. 1991a), it is the introduction of FD-OCT that triggered the recent development of vast array of OCT applications in several fields. FD-OCT theory states that the spectral power amplitude of the backscattered wave is equal to the Fourier transform of the axial distribution of the object scattering potential. The simplest advantage of FD-OCT over time-domain OCT is that the sample depth information is obtained in parallel without a need to move the reference mirror, resulting in enhanced system sensitivity to measure the backscattering light,

typically with > 20 dB as compared to its time domain counterpart. Due to this advantage, it affords faster imaging speed with a limited light power allowed for imaging living tissue (as set by the safety standard for the use of lasers).

The high speed of the FD-OCT systems has enabled to image not only tissue structural information, but also to investigate functional parameters, for example, in vivo blood flow information using OCT-based angiography (OMAG) (Wang et al. 2007a). The inherent contrast for blood flow imaging comes from the endogenous light scattering from moving blood cells; therefore, no exogenous agent is required for imaging. FD-OCT system can be in two versions: Spectral-domain OCT (SD-OCT) and swept-source OCT (SS-OCT) (Choma et al. 2003). In SD-OCT, the optical frequency components are captured simultaneously with a dispersive element and a linear array detector (e.g. line scan camera); however, in SS-OCT, the optical frequency components are captured by a single detector (e.g. photodiode) in a time-encoded sequence by sweeping the frequency of the laser source.

In this chapter, I summarize today's technology alternatives of OCT and available OMAG methods. The aim is to be as inclusive as possible regarding methods, but then focus more on the ones that have produced the most promising results. I've utilized both SD-OCT and SS-OCT systems in this dissertation, depending on their inherit trade-offs, which are discussed in the following sections.

1.1.1 *Spectral Domain OCT (SD-OCT)*

A common SD-OCT system contains a broadband light source that emits light with low temporal coherence. The light is coupled into a 2x2 Michelson interferometer that divides the light into two arms. One arm, known as the reference arm, transmits the light towards a reference mirror. On the other hand, the sample arm directs the light towards the tissue of interest. This arm contains

an objective lens that delivers and focuses the light onto the sample, and scanners. The light that is backscattered from the tissue structures is recombined with the reference light, producing an interference pattern. This combined light is captured by a line-scan camera in the spectral domain, after passing it through a diffraction grating. The resulting data is called an A-line. To reconstruct the 3D objects, the beam is scanned in two dimensions across the sample surface, and the resulting A-lines are combined to create cross-sectional B-frames and volumetric OCT data cube. Figure 1.1 presents a typical implementation of a SD-OCT system.

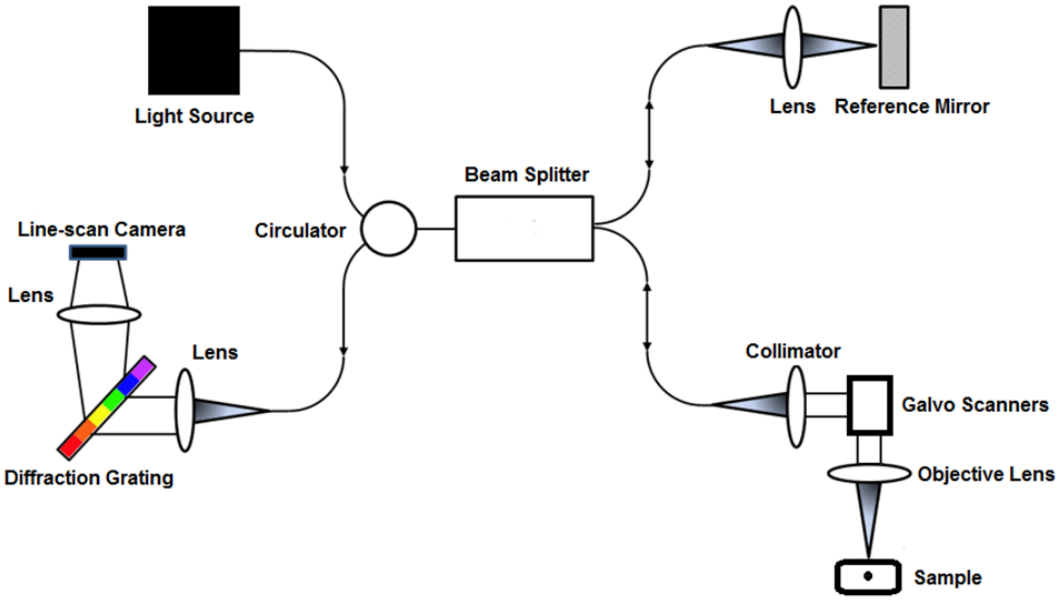

Figure 1.1. A common setup of a spectral-domain OCT system.
(Baran and Wang 2016)

The major bottlenecks of a standard SD-OCT system are the optical ranging distance and the line-scan camera speed. The sampling theorem (Bracewell 2000) states that the optical ranging distance is limited by the number of spectrometer element detectors (pixels on the line-scan camera) while depth resolution is limited by the spectral bandwidth of the light source. Moreover, available line-scan speed for cameras that work with 1300nm light sources is around 100-200 kHz, which limits the SD-OCT systems for applications where fast data acquisition is important. On the

bright side, SD-OCT systems are more stable, easier to maintain and can be cost-effective compared to SS-OCT systems.

1.1.2 *Swept-Source OCT (SS-OCT)*

SS-OCT systems eliminate the requirement of line scan cameras that are needed SD-OCT systems, and they can still be used in the 1,300 nm wavelength range. In SS-OCT systems, the most critical component is the light source that can sweep the wavelength of the laser across a broad spectral range. There are several types of swept-source lasers such as VCSEL or FDML. A Mach–Zehnder interferometer (MZI) built in the laser module provides real-time optical clocking, from which the MZI signal was detected by a dual-balanced detector connected to an external clock input of a data acquisition (DAQ) card. Rest of the system is similar to SD-OCT, includes reference and samples arms as shown in Figure 1.2.

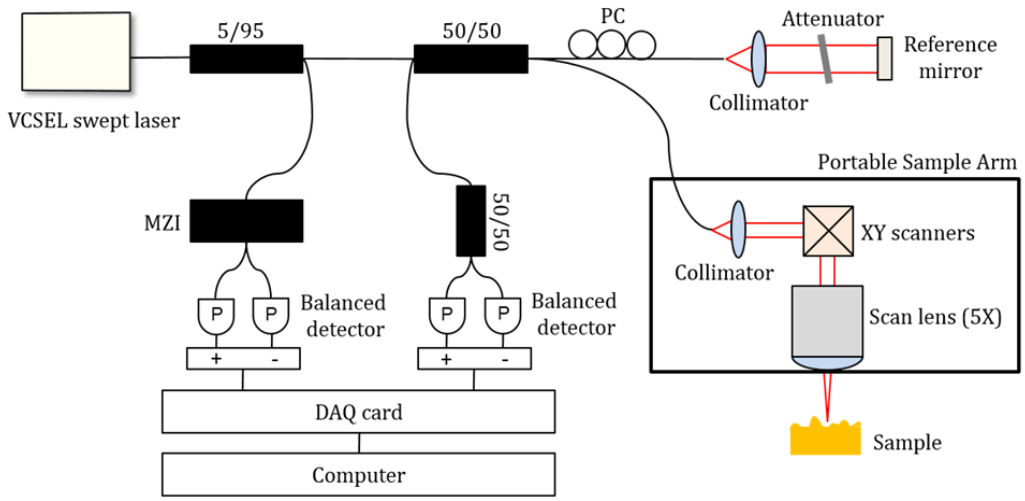

Figure 1.2. A common setup of a swept-source OCT system.

MZI: Mach–Zehnder interferometer; P: Photo-detector; DAQ card: Data acquisition card; PC: Polarization controller. (Baran et al. 2016)

Overall, SS-OCT offers several advantages over SD-OCT such as, above MHz A-line scan rate, longer imaging range, less depth-dependent signal roll-off, and less motion-induced signal loss due to fringe washout (Potsaid et al. 2010). They can be especially more useful for providing

good contrast in highly scattering human skin tissue, where fast data acquisition and sensitivity are important. However, SS-OCT systems typically contain high phase noise, which is introduced from the cycle-to-cycle tuning and timing variability (Tsai et al. 2011), and could be more expensive. I believe, they can become a popular choice of OCT system in the future, if more stable and cost-effective swept-sources are introduced to the market.

1.2 OCT ANGIOGRAPHY

OCT signal's temporal and spatial statistics contain the information of the movement of the scattering particles. Moving particles inside a sample have a larger signal variance compared to static particles. By studying these differences through analyzing the phase and/or intensity of complex OCT signals, blood vessels can be differentiated from the surrounding static tissue.

During the last decade, several OCT angiography techniques have been developed using FD-OCT systems. These techniques can be summarized into 4 broad categories: 1) Phase based methods that are sensitive to axial flow velocity, 2) Intensity based methods, which are sensitive to dynamic speckle formed by a moving particle, 3) The complex based methods, which are sensitive to both axial flow and dynamic speckles, including those induced by transverse moving particles, and 4) Capillary flux and velocity mapping methods, which use various statistical analyses of OCT signal to estimate the red blood cell (RBC) flux and velocities in capillaries. In this section, I provide brief summaries of these methods. A detailed comparison between prominent OCT angiography protocols using a single system can be found in (Zhang et al. 2015).

1.2.1 *Complex Signal Based Methods*

The complex signal based methods include OCT-based microangiography (OMAG) (Wang et al. 2007a) and complex variance based angiography (Nam et al. 2014). These methods analyze the

temporal changes in A-lines from the same location or highly overlapping locations over the sample to contrast blood flow. The sensitivity to blood flow velocities depends on the time interval between A-lines that are used for analysis. To contrast blood flows within larger vessels, a shorter time interval is used which is sensitive to faster velocities. However, in small vessels, including capillaries, the flow velocity is relatively slow (a few mm/s); therefore, a longer time interval between A-lines is required to have the adequate sensitivity. Hence these methods might not be the best alternative for time-sensitive imaging applications if it is required to quantify blood flow with a large dynamic range. It is also important to note that if the time interval, and thus the total data acquisition time, is too long, the system will be susceptible to motion artifacts due to sample motion.

The analysis of OMAG in the slow axis has been known as ultra-high sensitive OMAG (UHS-OMAG) (An et al. 2010a). In this method, the signal processing is done between A-lines across different B-frames instead of between adjacent A-lines. The proposed OMAG scanning pattern involves performing repeated B-scans (typically two or more) at one transverse location, then move to next transverse location to do the same until the last location is reached in the slow scan axis of 3D data cube. To obtain the signals that represent the blood flow, a high-pass filter is used as a differential operation on the complex OCT signals, C(t, x), to eliminate the static tissue signals:

$$C_{Flow}(t_j, x) = | C(t_j, x) - C(t_{j-1}, x) | \tag{1.1}$$

where j represents the index of the B scan in the slow scan direction, and x is the location of the A-line in B scan. The magnitude of differentiated signals in Eq. (1.1) represents the strength of the flow signals, proportional to the particle concentration within interrogated focal volume (Wang and Wang 2010; Yousefi and Wang 2014).

Using this method, 300 Hz frame rate can achieve necessary sensitivity to image slow flows in capillaries up to ~4μm/s (An et al. 2010a). Accordingly, it is possible not to compromise between the fast imaging speed advantage in FD-OCT and the requirement of relatively long time interval between A-lines to image smaller vessels, e.g. capillary vessel. A similar algorithm was also proposed by (Srinivasan et al. 2010a), in which the angiogram was obtained by taking the difference of the weighted OCT signals acquired between adjacent B-scans.

1.2.2 *Phase-based Methods*

Phase-based methods evaluate the axial velocity of flowing particles within a scattering medium, such as blood cells within biological tissues, by studying the Doppler effect on signals coming from moving particles. Accordingly, the phase difference between adjacent A-lines are calculated (Chen et al. 1997). The phase difference between sequential A-lines, $\Delta\varphi(z)$, is linearly related to the flow axial velocity (v_{axial}) by:

$$v_{axial}(z) = \frac{\lambda\Delta\varphi(z)}{4\pi n\Delta t} \tag{1.2}$$

where Δt is the time interval between adjacent A-lines and n is the refraction index of the tissue. Accordingly, longer Δt is required for detecting slow velocities, which might still be in sufficient to detect irregular and slow RBC flow in capillaries.

Several variations of phase-based methods for angiography have been reported where the absolute value of the phase difference (Makita et al. 2006), squared phase difference (i.e., Doppler power) (Kurokawa et al. 2012) or the variance of several adjacent A-line phase differences (Kim et al. 2011) are used. The comparison between different methods can be found here (Liu et al. 2012).

The recent work of You et.al showed great promise in quantitative capillary flow detection by using a phase summation method and vessel tracking (You et al. 2014). Moreover, Doppler optical microangiography (DOMAG) (Wang and An 2009) has been proposed to improve the performance of phase-based methods. DOMAG first utilizes OMAG to separate the static from the dynamic signal to reduce the noise produced by the optical heterogeneous properties of the sample, and then analyzes the phase differences between adjacent A scans. Moreover, a variation of DOMAG is recently introduced (Shi et al. 2013) by choosing A-lines at various time points, to have change multiple Δts, for analyzing the Doppler signal. This method is important in the investigation of impaired blood flow within microcirculatory tissue beds, because it can provide Doppler analyses over a wide velocity range from capillaries to arterioles and venules, providing useful information to aid in the assessment of whether the blood flow within injured region of interest is compromised or ceased to flow. Overall, the performance of phase-based methods is deteriorated by two main factors: 1) the optical heterogeneity of the sample (Wang and Ma 2006), and 2) the phase instability caused by the light source or the sample motion artifacts (Yun et al. 2004).

1.2.3 *Intensity-based Methods*

In some cases the flow of particles induces the change in the phase of OCT signal, primarily. Hence, removal of the phase information from the OCT signal might have a negative effect. However, using only intensity amplitude to generate angiography maps of tissue beds has been very popular, since phase noise is a major challenge to overcome in complex or phase-based methods. The intensity-based methods include correlation mapping (Jonathan et al. 2011), split-spectrum amplitude decorrelation (Jia et al. 2012), speckle variance (Mariampillai et al. 2010), and correlation masked speckle variance (Choi et al. 2014a) techniques.

These techniques utilize the strong speckle effect in the vicinity of functional vascular regions compared to surrounding non-flow regions to contrast blood flow. By calculating correlation coefficients or speckle variance across the pixels, blood vessel morphology can be visualized. Contrast is achieved since flow regions exhibit low correlation coefficient values and high speckle variance values while the bulk tissue give high correlation and low speckle variance values. Dense scanning is usually required for the success of these techniques. This feature was first discovered in OCT signals by Barton et al. in 2005 and engineered to image blood flow within in vivo tissue beds (Barton and Stromski 2005).

1.2.4 *Capillary Flux and Velocity Mapping Methods*

Although the above OCT angiography methods are very powerful for larger blood vessels, it is not trivial to map RBC flux and velocity in capillaries using them. This is mainly due to the low hematocrit counts in the capillaries and the angle dependency of Doppler measurements. New methods that measure the statistical changes in the OCT signal have been developed for this purpose.

Firstly, Ren et al. developed particle counting Doppler OCT technique to estimate RBC flux and velocity within a single capillary in rodent cortex (Ren et al. 2012). The authors counted the Doppler phase transients induced by the passage of a RBC through a single capillary and estimated the mean RBC flux (~19/s) and velocity (~0.72 mm/s). Moreover, researchers at Martinos Center for Biomedical Imaging developed similar methods to acquire RBC flux and velocity values at multiple capillaries. The first method (Lee et al. 2013) monitors the time course of the OCT intensity signal at the capillaries where individual RBC passage is believed to cause a peak in the signal, and the width of the peak would be negatively correlated with the speed. Capturing these peaks was made by fitting Gaussian functions to them. The accuracy of this method is tested by a

traditional stripe pattern-based estimation. The caveat of this method is the long imaging time due to the need for a large number of measurement points.

As an alternative, the same group also proposed a technique called statistical intensity variation (SIV) imaging (Lee et al. 2014) where they claimed that more RBCs passing from a certain location will create a statically higher SIV. Here, SIV between two consecutive frames is computed by:

$$SIV(z,x,y) = \frac{E[I(z,x,t_2;y) - I(z,x,t_1;y)]^2}{E[\frac{1}{2}[I^2(z,x,t_2;y) + I^2(z,x,t_1;y)]]} \tag{1.3}$$

where I(z,x,t1;y) and I(z,x,t2;y) are the first and second B-scans at a given Y-position, respectively, and E[] denotes ensemble averaging which can be implemented by averaging over neighboring voxels and/or repeated volumes. This ensemble averaging minimizes the stochastic speckle effect in the OCT intensity. The computed SIVs are then compared between various points at a capillary segment to estimate RBC flux in that segment. Although this technique overcomes the problem of long data acquisition time of previous methods, it requires a complicated 3D Hessian matrix analysis based capillary vectorization, thus is computational demanding.

Benefiting from these methods, they mapped heterogeneous flux distribution in cerebral capillaries with the mean RBC flux of ~20 RBCs/s in healthy rat brain. The dynamic range of RBC flux is a function of the time gap between measurement points, in this case the frame rate. The upper limit in the measured capillary RBC flux in these studies (40 RBCs/s) were relatively lower than those in the literature where the reported values range from 40-45 RBC/s (Stefanovic et al. 2008b) to 80 RBC/s (Kleinfeld et al. 1998). Considering this high variability across the literature, possibly due to the differences in the animal species, anesthesia and physiology, higher frame rates should be utilized for more accurate RBC flux estimations.

Moreover, Wang et al. demonstrated an autocorrelation method for mapping transverse particle-flow velocities by estimating the dwell time of flowing particles crossing the probe beam (Wang and Wang 2010). They showed that the slope of the normalized autocorrelation function of the backscattered light is proportional to the transverse velocity. Same authors also applied another method analogous to widely used fluorescence correlation spectroscopy technique (Krichevsky and Bonnet 2002) which correlate the fluctuations of the OCT signals to the fluctuations of the particle numbers flowing through the detection volume (Wang and Wang 2011). These techniques have been verified with flow phantoms. Moreover, Srinivasan et al. used complex field autocorrelation function as a metric for capillary velocities in rodent cortex and correlated with the velocity measurements obtained from TPM (Srinivasan et al. 2012). Differently from (Wang and Wang 2010, 2011), the analysis was performed on A-lines along the slow axis of repeated B-scans.

Chapter 2. NEW ALGORITHMS AND METHODS FOR OCT

2.1 TISSUE INJURY MAPPING (TIM)

2.1.1 *Background and Motivation*

The diseased state or injury alter the physical characteristics of tissue. This alteration causes observable changes in the received signal (either optical or acoustic), primarily through absorption and scattering. Changes in the signal attenuation decay within tissue, measured as an attenuation coefficient, can be used for non-invasive differentiation of various in vivo tissue with pathological conditions. The first use of this idea goes back to 1980s where an acoustic attenuation coefficient was used in ultrasonic tissue characterization (Lizzi et al. 1987) for a wide range of applications including liver (Kuc 1980) and breast (Berger et al. 1990).

Since the introduction of OCT in the early 1990s (Huang et al. 1991b), measuring optical attenuation coefficient (OAC) using OCT signals has been a popular way for *in vivo* characterization of various tissue injury or disease types, i.e. atherosclerosis (Xu et al. 2008), burn scar (Gong et al. 2013), glaucoma (Vermeer et al. 2014), and ischemic brain (Srinivasan et al. 2013a). Moreover, OMAG technique has also been intensively used to study the microvascular changes within various pathological tissue, *in vivo*. For example, OMAG has been recently used to investigate the vascular abnormalities in human facial skin with acne vulgaris (Baran et al. 2015b) and to visualize mouse cerebral vasodynamics after stroke (Wang et al. 2014).

Tissue injury affects both microvasculature and cellular structure (Gong et al. 2013). OAC reconstruction alone can only provide the information about structural changes in tissue and cannot connect it with the microvascular remodeling during the injury and the recovery periods. Here, we

combine the OAC reconstruction method recently developed by Vermeer et.al with OMAG for more detailed tissue injury mapping (TIM) (Vermeer et al. 2014). OMAG provides an important additional information about the extent of injury by generating a high resolution map of microvasculature. We also propose a sorted average intensity projection (sAIP) algorithm for en face mapping of the reconstructed OACs belonging to different tissue types. The results demonstrate that TIM results provide improved tissue contrast over standard en face OCT images.

2.1.2 *System Description*

We used a SD-OCT system (Reif et al. 2014) with a superluminescent diode (Thorlabs Inc.) that has a central wavelength of 1340 nm with a bandwidth of 110 nm, providing a ~7 μm axial resolution in the air. In the sample arm, 10X scan lens (Thorlabs Inc.) was used to achieve ~7 μm lateral resolution. The linescan camera (Goodrich Inc.) used in the spectrometer had 92 kHz line rate. The OCT images of the mouse cerebral cortex were taken through the open skull cranial window (Li et al. 2014). The area under the window (parietal cortex) corresponded to the supplying territory of distal branches of both the middle cerebral artery (MCA) and anterior cerebral artery (ACA), and was subjected to imaging during baseline, MCA occlusion (Koizumi et al. 1986), and reperfusion periods. The animal procedures performed in this study are approved by the Institute of Animal Care and Use Committee (IACUC) of the University of Washington.

2.1.3 *Optical Attenuation Coefficient (OAC) Mapping*

Simple single backscattering of light is typically assumed for OCT systems using the following equation:

$$I(x) = I_0 \rho e^{-2\mu x} \tag{2.1}$$

where I represents the value of the detected intensity, I_0 is the intensity of incident light, ρ is the backscattering coefficient, μ is the decay constant, x is the depth. Factor of 2 is due to the fact that light travels a round trip. OAC can be calculated by extracting μ by fitting an exponential curve to the backscattered signal. However, this basic approach cannot accurately separate different layers of tissue without pre-segmenting and pre-averaging. In addition, the RBCs passing through vessels generate a shadowing effect through forward scattering, causing artificially high OAC (Gong et al. 2013), which cannot be differentiated using this basic method.

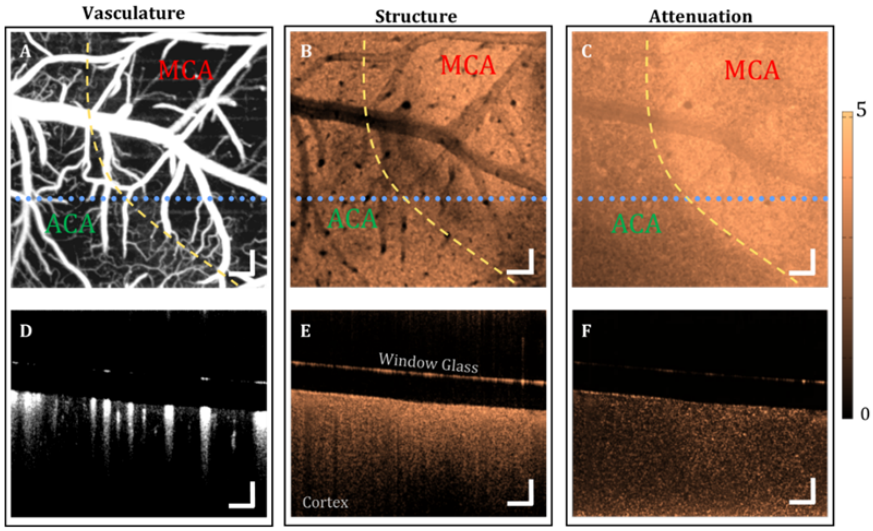

Figure 2.1. OMAG, OCT structural and OAC mapping images during stroke.

(a) En face maximum intensity projection (MIP) of OMAG image. (b) En face AIP of OCT structural image. (c) En face sAIP of OAC image. (d-f) Cross sectional views of OMAG, OCT structural image and OAC image, respectively, at a location delineated with blue dashed line. Yellow dashed line point out the border between healthy and infarct region. Scale bar represents 0.2 mm. (Baran et al. 2015c)

Alternatively, OACs can be estimated locally where every pixel in the OCT data is converted into a corresponding OAC pixel using the following relationship (Vermeer et al. 2014):

$$\mu[i] \approx \frac{I[i]}{2\Delta \sum_{i+1}^{\infty} I[i]} \tag{2.2}$$

where $I[i]$ is the OCT signal at a certain pixel, Δ is the pixel size and $\mu[i]$ is the OAC at that pixel. This method can be used for both homogeneous and heterogeneous tissue and does not require

pre-segmenting or pre-averaging of OCT data. It also suffers less from the shadowing artifacts, since it calculates the OAC separately at each pixel in contrast to fitting a curve along the depth in the region of interest.

Here, we propose an en face sAIP method to accurately map calculated OACs for delineation of potential tissue injury. Firstly, we select the interested volume from the 3D OAC data and then sort the OACs in the each A-line in an ascending order. Finally, we use one of the following equations to calculate the average OAC at a specific en face location, defined as $\mu_{average}[y]$:

$$\mu_{average\_1}[y] = \frac{\sum_{i=(N/2)-(M/2)}^{(N/2)+(M/2)} \mu_{sorted}[i]}{M} \tag{2.3}$$

$$\mu_{average\_2}[y] = \frac{\sum_{i=N-M-D}^{N-D} \mu_{sorted}[i]}{M} \tag{2.4}$$

Here, $\mu_{sorted}[i]$ is the value of the i^{th} OAC and N is the total pixel number in the selected portion of the each A-line. M and D are adjustable parameters that determine the number of pixels to be averaged and the number of pixels to skip, respectively.

Fig. 2.1 compares the AIP of OCT structural and OAC 3D data sets during MCA occlusion in mouse cerebral cortex. Fig. 2.1a shows the en face maximum intensity projection (MIP) of microvasculature in the pial layer. As can be seen in Fig. 2.1a, most of the capillaries disappear from the MCA side during occlusion, which lead to a potential infarct development. The progression of this region causes scattering changes in the tissue which can be distinguished from the healthy region. TIM image in Fig. 2.1c shows a clear difference between MCA and ACA sides after MCA occlusion. On the other hand, the en face AIP of the structural data in Fig. 2.1b comes with the blood vessel shadowing artifacts and provides a non-uniform map of tissue characteristics. This can also be observed from the cross-sectional images in Fig. 2.1e-f.

First sorting and then averaging several OACs helps removing possible fluctuations in individual OACs and produces a smooth en face map as in Fig. 2.1c. However, M parameter should be picked carefully, based on the volume size. Averaging excessive number of pixels would make the detection of small OAC changes difficult. On the other hand, D parameter can be used to remove the unwanted portion of the data, such as surface reflections. Both parameters depend on the system sensitivity, the optics, and the tissue.

We average the middle pixels in the sorted data using Eq. 2.3 to remove the possible inaccurate part due to noise and multiple scattering effects for a relatively homogeneous tissue, e.g. cortex. However, for a heterogeneous tissue, e.g. skin, we use Eq. 2.4 to average the pixels close to the highest intensity, after removing the possible surface artifacts, which correspond to dermal layer.

2.1.4 *Contrast comparison between OAC mapping methods*

To shows the advantages of sAIP for TIM, we compared the contrast of OAC en face maps generated by different projection methods, sAIP, AIP, and MIP, in Fig. 2.2. Here, contrast ratio, C, is defined in Eq. 2.5:

$$C = \frac{I_{injured} - I_{healthy}}{I_{healthy}} \tag{2.5}$$

where $I_{injured}$ and $I_{healthy}$ are mean pixel intensity values in windows (3x3 pixels) collected from 25 different parts of the potentially injured and healthy areas in the image, respectively.

Results in Fig. 2.2 show that sAIP provides a better C value to AIP method and comparable to MIP method for a relatively homogeneous tissue such as cortex using Eq. (2.3). However, sAIP method using Eq. (2.4) is clearly superior in terms of C value to both alternative methods for imaging a relatively heterogeneous tissue such as human skin. Moreover, average C values are

calculated less than 0.02 within the same tissue types in images acquired using sAIP, which lead to visually uniform images.

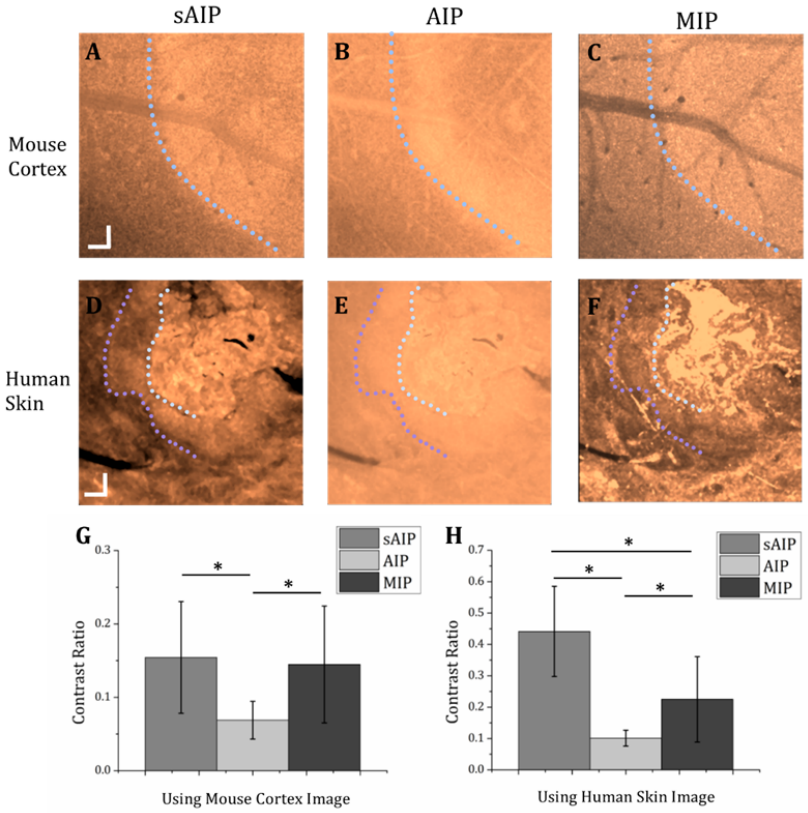

Figure 2.2. Contrast comparison between various OAC mapping methods.

(a-c) En face OAC images of mouse cortex during MCA occlusion generated using (a) sAIP with Eq. 3, (b) AIP, and (c) MIP. (d-f) En face OAC images of human skin with acne generated using (d) sAIP with Eq. 4, (e) AIP, and (f) MIP. (g-h) Contrast ratio comparison between projection methods using (g) cortex data, (h) human skin data. Dashed lines point out the borders between injured and healthy tissues. *$P<10^{-5}$ significantly different data sets (paired t-test). Scale bar represents 0.2 mm. (Baran et al. 2015c)

Scattering and absorption are typically higher in dermis compared to epidermis in human skin. When we sort the data in an ascending order, the first few pixels (highest intensity pixels) typically belong to the surface reflection and the rest are expected to belong to dermis. In Eq. 2.4, parameter D is used to skip the surface reflection pixels from the averaging. MIP projection method picks the surface reflection pixels over dermis ones, and AIP method mixes the dermis and epidermis signals which reduce the contrast.

2.1.5 *Discussion and Conclusion*

TIM is a promising tool to provide high resolution in vivo imaging of rodent brain during stroke. The results of TIM imaging on mouse cortex during MCA occlusion (Fig. 2.1) indicate that the OAC and OMAG may be successfully combined as an indicator to show the status of brain tissue, providing useful information on the critical time zone for treatment to rescue the part of cortex exposed to severe hypoxia. Detailed studies can be conducted using TIM imaging to discover new therapeutic methods for stroke.

In addition to stroke research, TIM can also be used in the investigation of human skin diseases like acne vulgaris. The in vivo TIM imaging results clearly demonstrate the tissue structural and microvascular states within an acne lesion in a great detail. As shown in Fig. 2.2d, breakage of dermis naturally leads to hypertrophic scarring observed with increased optical scattering.

Using en face sAIP of OACs, without requiring pre-segmentation and complicated image processing algorithms, we are able to provide high contrast map of injured and healthy tissue tissue regions. However, it is important to note that the OAC reconstruction method used in our work is based on two major assumptions: the most of the light is attenuated within the recorded imaging depth range, and only the fixed ratio of the probing light backscatters from the attenuated light, i.e., backscattering coefficient is constant. Due to the limited penetration depth of OCT signal in tissue, the first assumption is generally reasonable. On the other hand, second assumption is not valid for heterogeneous tissue types like human skin, and this might lead to inaccurate estimate of OAC. Nevertheless, it still effectively delineates different tissue types (Vermeer et al. 2014). The dashed lines are provided in the figures to point out the observable changes but further studies are required to correlate local contrast changes with histology results.

Moreover, based on the results presented, it is reasonable to hypothesize that the TIM imaging can be used to utilize OAC and vascular density as biomarkers in the monitoring, therapeutic treatment and management of other prevalent skin diseases in general, e.g. port wine stain (PWS), psoriasis, skin burn, and skin cancer. For instance, replacing a standard visual inspection of the skin burn, the scar vascular density and scattering property map can be potential indicators to assess the scar progression, and might help improve the accuracy of diagnosis and treatment of pathological scarring. Furthermore, skin cancer can be better visualized and understood for treatment and research purposes without using invasive techniques.

In summary, in vivo non-invasive TIM imaging can show the structural and microvascular changes in pathological tissue. The results demonstrated capabilities of OCT-based TIM to visualize functional changes during stroke on mouse cerebral cortex and acne lesion development on human skin. Although further well-designed studies are required to systematically investigate and establish the benefits of this technique, earlier results are promising that TIM can become a useful tool for the clinical management and development of new treatment alternatives for various diseases.

2.2 OCT-BASED LYMPHANGIOGRAPHY (OLAG)

2.2.1 *Background and Motivation*

Lymphatic system plays a critical role in tissue fluid homeostasis by draining lymph fluid from the extracellular space through unidirectional, thin-walled capillaries and collecting vessel network. Its dysfunction causes symptoms like edema (Sevick-Muraca et al. 2014). Early detection of dysfunctional lymphatic system could enable better diagnoses and more effective treatments.

Most of the available *in vivo* lymphatic imaging methods require the administration of exogenous contrast agents either directly into lymphatics via the cannulation of a lymphatic vessel or indirectly into lymphatic plexus via intradermal injection. Most of these existing contrast agents can induce side effects to patients (Morcos 2005). In addition, locating and cannulating a lymphatic vessel can be significantly invasive for patients and not practical in preclinical setting using transgenic mouse models due to their small size (Lee et al. 2015). On the other hand, X-ray (Kos et al. 2007), magnetic resonance imaging (Liu et al. 2009), near infrared fluorescence imaging (Polom et al. 2011) and lymphoscintigraphy8 techniques provide a body imaging, albeit with poor resolution, so they are used for imaging the larger vessels and the lymph nodes. An alternative technique, fluorescence microlymphography (Bollinger and Amann-Vesti 2013), provides a limited penetrating imaging depth (~200 μm) in tissue but with a relatively higher resolution (~50 μm). Thus, it is used in the visualization of initial lymphatics near injection site.

Surprisingly, there are only few non-invasive methods reported in the literature (Vakoc et al. 2009a; Martinez-Corral et al. 2012; Yousefi et al. 2014) for imaging the response of lymphatics within *in vivo* animal models. Unfortunately, none of these techniques has shown its potential in clinical translation. Previously, OCT has been used for label-free imaging of lymphatic vessels on an in vivo mouse ear model using OCT (Vakoc et al. 2009a; Yousefi et al. 2014; Qin et al. 2015).

The optical scattering properties of lymph fluid, which is nearly transparent, and tissue, which is highly scattering, are significantly different. Hence, the lymphatic vessels appear as low-scattering (darker) regions in the OCT images and can be contrasted from the surrounding tissue. Moreover, volumetric connectivity between lymphatic vessels and characteristic lymphangion morphology can help identifying lymphatic network from other possible low-scattering features inside the skin. The result of lymphangiography maps acquired by OCT were confirmed by intra-dermal injection of Evan's blue dye to mouse ear and monitoring the uptake pathway by surrounding lymph vessels into the lymph nodes (Vakoc et al. 2009a; Yousefi et al. 2014).

OCT-based lymphangiography (OLAG) have been realized by applying a threshold to the OCT intensity images (Qin et al. 2015), or using vesselness models based on Hessian multi-scale filters (Yousefi et al. 2014). These methods work well on in vivo mouse ear models, however, not as successful on *in vivo* human skin. This is due to the thicker and higher scattering nature of human skin compared to mouse ear skin. In OCT images of human skin, the contrast of the dark areas to the surrounding tissue becomes poor and the aforementioned algorithms fail to differentiate these areas.

In this work, we developed a set of methods to contrast these dark areas within highly scattering tissue by reducing light attenuation effect on OCT cross-sectional images and extracting lymphatic vessels through re-arranged enface OCT images of human skin. Without using contrast agents, we are able to non-invasively visualize lymphatic networks along with microvasculature within *in vivo* human skin, for the first time.

2.2.2 *System Description*

In this study, we chose using SS-OCT over SD-OCT system for its longer imaging range and less depth-dependent signal roll-off (Potsaid et al. 2010) for lymphatic imaging application within

highly scattering *in vivo* human skin. The system operates at 1310 nm central wavelength with a swept light source containing a MEMS-tunable vertical cavity surface-emitting laser (VCSEL) (Thorlabs Inc.). This source is able to sweep the wavelength of the laser at a fixed repetition rate of 100 kHz, with a long coherence length (>50 mm), ~15 μm axial resolution in tissue, and 2 mm imaging penetration depth in human skin. The sample arm consists of a probe imaging head (including galvanometric scanners) and a 5X objective lens (LSM03, Thorlabs Inc.), giving 22 μm lateral resolution.

The optical power of incident light upon the sample was ~5.2 mW, well below the American National Standards Institute (ANSI) standards (Z136.1) for the safe use of near infrared light at 1310 nm on skin. A mineral oil was topically applied to the skin surface to mitigate the strong specular reflection. For animal experiments, the procedures were approved by the Institute of Animal Care and Use Committee (IACUC) of the University of Washington. The use of OCT/OMAG laboratory instrumentations on volunteer human subjects was reviewed and approved by the Institutional Review Board of the University of Washington, and informed consent was obtained from all subjects before imaging. This pilot study followed the tenets of the Declaration of Helsinki and was conducted in compliance with the Health Insurance Portability and Accountability Act.

2.2.3 *Details of OLAG Protocol*

As explained above, OLAG relies on the fact that the lymphatic vessels appear dark in OCT images compared to the surrounding tissue. Hence, good contrast between in OCT images is important for accurate detection of lymphatic vessels within human skin. However, highly non-uniform intensity distribution within the OCT images of human skin make it difficult to extract lymphatic vessels. This occurs due to the light attenuation and the heterogeneous tissue properties.

In order to mitigate this problem, we propose to enhance the contrast of OCT images of human skin both in axial and lateral directions using the protocol described below.

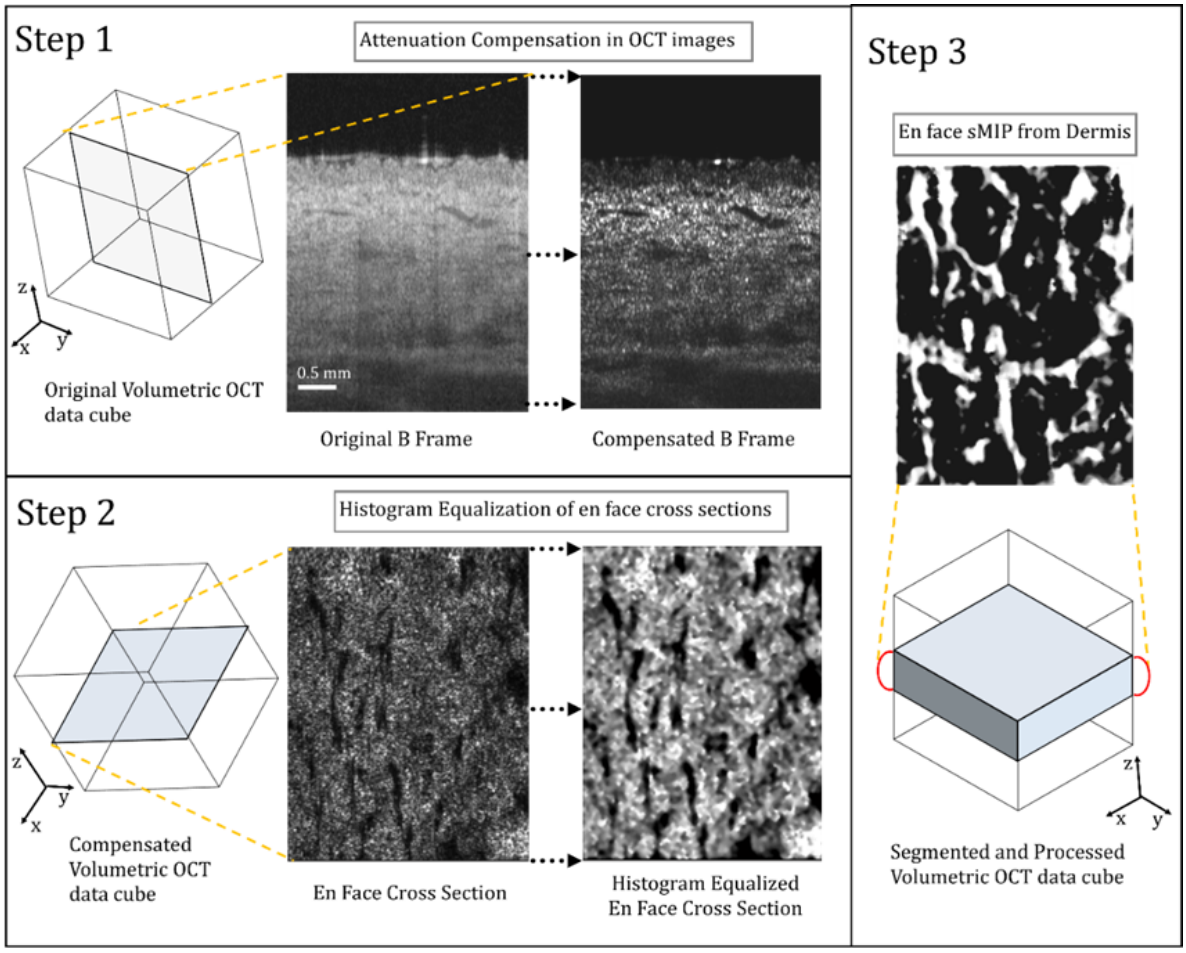

Figure 2.3. OLAG protocol for mapping lymphatic vessels within human dermis.
(Baran et al. 2016)

The Fig. 2.3 shows the proposed protocol and the resulting OLAG image. As a first step, the contrast of the original OCT structural images in coronal plane (i.e. B-scan) are enhanced by compensating light attenuation (explained in Section 2.2.3.1). This procedure serves two purposes: 1) Delineating dermis from epidermis (epidermis looks brighter), and 2) Increasing contrast between the lymphatic vessels from the surrounding tissue. The dermis is then separated from epidermis through automatic segmentation. In step 2, the compensated and segmented volumetric data is sliced in en face cross-sections in transverse plane and then the contrast of these slices is

further improved using the histogram equalization algorithm (explained in Section 2.2.3.2). Finally, in step 3, the lymphatic vessels (dark areas) in the volumetric data are mapped using sorted minimum intensity projection (sMIP) method, where pixels are sorted and the ones with lower intensities are selected for projection map (explained in Section 2.2.3.3). Here, white color is used to map lymphatic vessels.

To compare our method with the previous results, we applied proposed OLAG protocol to image *in vivo* mouse ear after 5-minute depilation using a hot water. The images acquired using our proposed method matches with the earlier reported results in literature (Vakoc et al. 2009a; Yousefi et al. 2014), which were validated using blue dye injection.

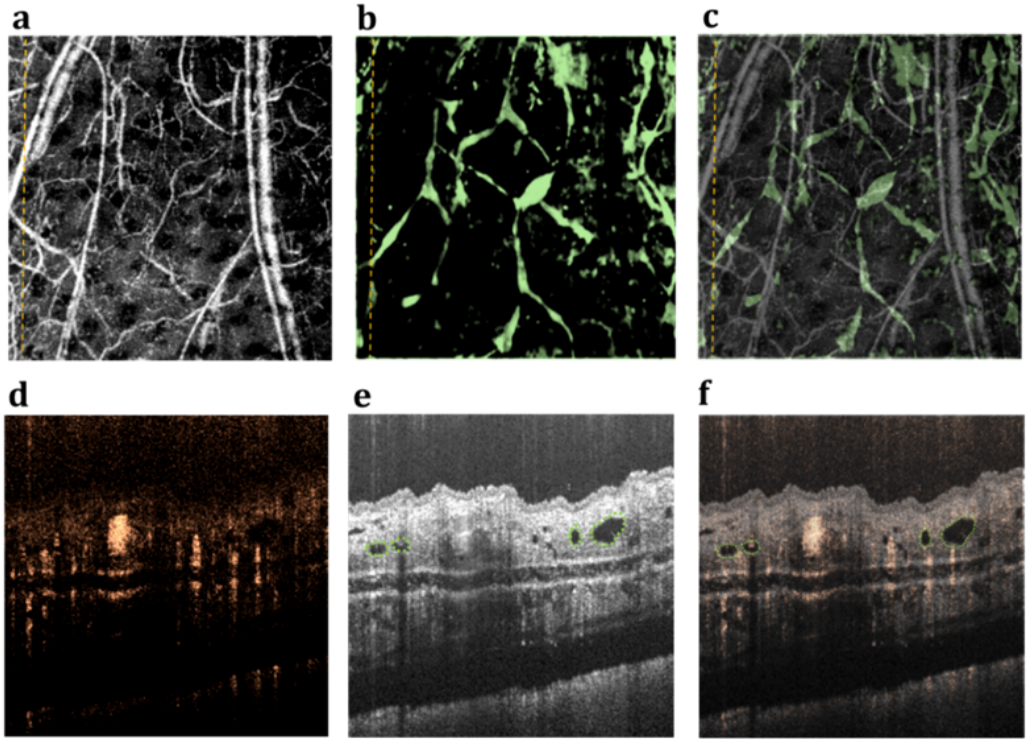

Figure 2.4. In vivo mouse ear imaging using OMAG and OLAG

(a) En face MIP of the 3D OMAG image. (b) En face sMIP of the 3D OCT lymphangiography. (c) Overlay of (a-b). (d-f) Cross-sectional views of corresponding OCT data sets from a location delineated with the orange dashed line where (d) OMAG image, (e) OCT structure image where lymphatic vessels are shown with green dashed circles, and (f) overlay of (d-e). The field of view of images is 2×2 mm^2. (Baran et al. 2016)

2.2.3.1 Contrast enhancement in OCT A-scans through attenuation compensation

The output, I, in the standard SS-OCT system can be described as below (Choma et al. 2003):

$$I[k_m] = \frac{1}{2}\rho S[k_m](R_R + R_S + 2\sqrt{R_R R_S}\cos(2k_m \Delta x)) \quad (2.6)$$

where, k is the optical wavenumber, ρ is the detector responsivity, $S[k_m]$ is the source spectral density, Δx is the optical path length difference between the reference and the sample arms, and R_R and R_S are the reflectivity of the reference and the sample arm, respectively. The acquired signal ideally has values at M evenly spaced wavenumbers, so $k = \{k_1, k_2, \ldots, k_m, \ldots, k_M\}$. The cross correlation term $H[k_m]$ is derived after removing the constant offset terms from Eq. 2.6:

$$H[k_m] = \frac{1}{2}\rho S[k_m]\sqrt{R_R R_S}\cos(2k_m \Delta x)) \quad (2.7)$$

After taking a discrete inverse Fourier transform of Eq. 2.7, OCT A-scan, D[z], as a function of depth, is obtained as below:

$$D[z] = \sum_{k=1}^{M} H[k_m] e^{-2k_m z} \quad (2.8)$$

However, when light penetrates within the tissue, it attenuates through the absorption (μ_a) and scattering (μ_s). Accordingly, OCT A-scan signal is modified as below in its continuous form:

$$D_A(z) = D(z) e^{-2\alpha \int_0^z A(\mu) d\mu} \quad (2.9)$$

where α is the backscattering coefficient, and $A(\mu) = \mu_a + \mu_s$. When A(μ) is large at a certain depth, such as at a blood vessel, the remaining depth in that A-scan is shadowed. This effect contributes to the poor contrast between the tissue and the lymphatic vessels in the deeper sections. To compensate for the attenuation in the OCT images, this decay term can be removed by using the following operation (Girard et al. 2011; Vermeer et al. 2014):

$$\int_{z=d}^{\infty} D_A(z) = \int_{z=d}^{\infty} D(z) e^{-2\alpha \int_0^z A(\mu) d\mu} = \frac{e^{-2\alpha \int_0^z A(\mu) d\mu}}{2\alpha}$$

$$\rightarrow e^{-2\alpha \int_0^z A(\mu) d\mu} = 2\alpha \int_{z=d}^{\infty} D_A(z) \quad (2.10)$$

substituting Eq. 2.10 into Eq. 2.9 and discretizing:

$$D[z] = \frac{D_A[z]}{2\alpha \sum_{z=d}^{\infty} D_A[z]} \approx \frac{D_A[z]}{2\alpha \sum_{z=d}^{F} D_A[z]} \quad (2.11)$$

Here, the backscattering coefficient, α, should be adjusted (0<α<1) based on tissue characteristics, and assumed to be constant. F is the final depth in the A-scan where most of the light is assumed to be attenuated. Extracting attenuation coefficients μ_a and μ_s is not required. Nevertheless, D[z] in Eq. 2.11 is the compensated A-scan signal that produces cross-sectional OCT images with better intensity uniformity.

2.2.3.2 Contrast enhancement of the en face OCT cross sections through histogram equalization

Although the attenuation compensation step helps increasing contrast in A-scans, due to the non-uniform mineral oil distribution topically applied onto the skin and the non-flat surface of the skin, the OCT image intensity is still non-uniform in en face cross sections. This non-uniformity gets more apparent when a relatively larger field of view is used. Hence, we use an additional OCT image enhancement step on en face images before mapping the lymphatic vessels.

Histogram of an image is the defined as the probability distribution function of the grey intensity levels in that image. Histogram equalization method increases the global contrast of images when the gray levels are not distributed uniformly. It works by mapping input intensities into an output image where its probability distribution function is uniform and its cumulative distribution function histogram is the same as the input image. This way, the contrast of the image is stretched to be distributed uniformly in the dynamic range. On the other hand, it may produce unrealistic images and amplify background noise in homogenous regions.

As a solution, high peaks in the histograms, which correspond to homogenous regions in the image, are clipped and probability distribution function is non-uniformly reconstituted with

Rayleigh distribution to enhance the foreground and suppress the noise using equation below (Yousefi et al. 2013).

$$I = I_{min} + \sqrt{2\beta^2 \ln\left(\frac{1}{1-P_{input}(x)}\right)} \tag{2.12}$$

Here, I is the output intensity, x is the input intensity, I_{min} is the low bound, β is the Rayleigh parameter and $P_{input}(x)$ is the cumulative probability of the input image. A higher β value creates higher contrast in the image but also increases saturation and noise levels. This technique transforms non-uniform, low-contrast en face OCT images into a uniform, high-contrast images to differentiate the dark areas (supposedly lymphatic vessels) in the OCT images.

2.2.3.3 Mapping of lymphatic vessels from a volumetric OCT image

Functional vasculature resides in the dermis of human skin, hence epidermis is needed to be segmented out from the OCT images. By extracting the first peak of each A-line, we first detect the first layer of epidermis. Then, we skip the epidermal layer starting from this first peak until the dermal-epidermal junction is reached by using a pre-determined number of pixels. After skipping the epidermal layer, we segment the pre-determined number of pixels correspond to the papillary and reticular dermal layers in each A-scan. Repeating this procedure for every A-line captures the interested volume automatically without the use of an additional treatment.

Furthermore, we sort the pixels in each A-scan based on their intensities in ascending order. Then we average the first N number of pixels (with minimum intensities) and map the averaged value on to an en face plane. In summary, $I_{en\_face}[x, y]$ is calculated as:

$$I_{en\_face}[x, y] = \frac{\sum_{i=1}^{M} I_{sorted}[x,y,i]}{M} \tag{2.13}$$

Here, $I_{sorted}[x,y,i]$ is the value of the i^{th} pixel in ascending order and M is the number of averaged pixels. This method is called sorted minimum intensity projection (sMIP). Final en face image is produced in inverted colors. The above procedures are illustrated in Fig. 2.3.

2.2.4 *Results*

2.2.4.1 OLAG within in vivo human arm skin

Using OCT, we imaged the skin in the ventral side of the human lower arm, and presented the OMAG and OLAG results in Fig. 2.5. To achieve a large field of view, the final en face image is formed by mosaicking 9 images, each with 3mm x 3mm area. Depth-resolved MIP image of OMAG shows the blood vessel network within human arm skin in Figure 2.5c. Figure 2.5a shows the cross-section of the dermis after the compensation and the segmentation. The lymphatic vessels in the corresponding portions of the dermis are presented with en face sMIP in Figure 1d-f. The results show that the lymphatic vessels are in smaller shapes in the top layers of dermis and it becomes larger in the deeper layer, which is consistent with the literature (LUBACH et al. 1996). Unlike blood vessels, lymphatic vessels are loosely attached together.

2.2.4.1 OLAG within in vivo human areola

The areolar dermis consists of highly active lymphatic plexus. Subareolar lymphatic plexus contains a rich network of lymphatic capillaries that originates in the dermis of the nipple–areolar complex, and ultimately terminates in regional lymph nodes. Because of its many interlymphatic connections, the subareolar lymphatic plexus is a great region for utilizing OLAG.

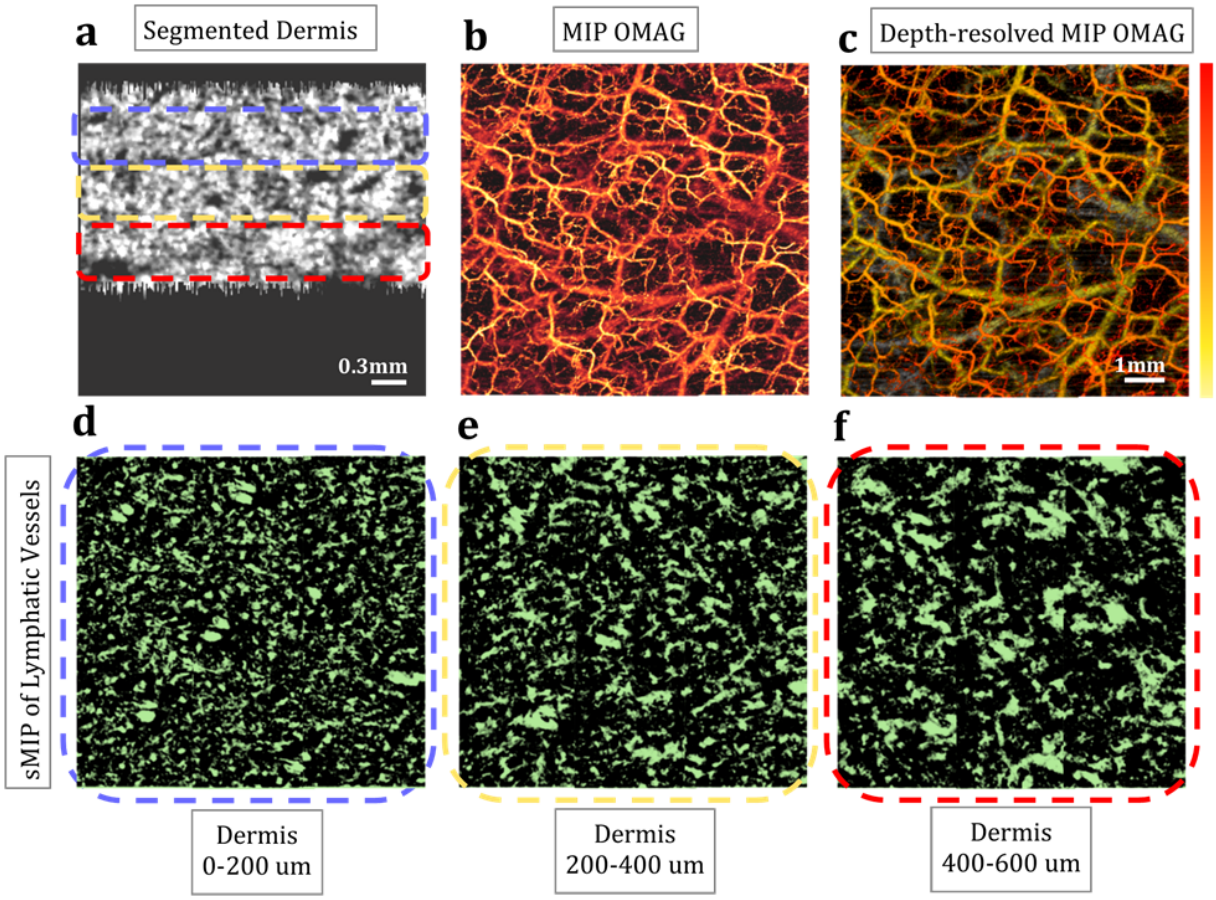

Figure 2.5. En face mapping of lymphatic vessels within human lower arm skin

(a) Segmented and processed OCT cross section of dermis. (b-c) En face OMAG images with MIP and depth-resolved MIP. (d-f) OLAG images from different depths of dermis. Field of view is 8 mm x 8 mm. (Baran et al. 2016)

Figure 2.6 shows the results of OMAG and OLAG for human areola with 5mm x 5mm imaging area. Depth-resolved MIP OMAG image shows the rich blood vessel network within human areola in Figure 2d. Figure 2c shows the cross-section of the dermis after the compensation and the segmentation. The lymphatic vessels in the corresponding portions of the dermis are shown with en face sMIP in Figure 2f-h. Compared to arm skin, lymphatics in areola are visualized with better interconnections. This can be attributed to smaller epidermal layer and more active lymphatic plexus in areola.

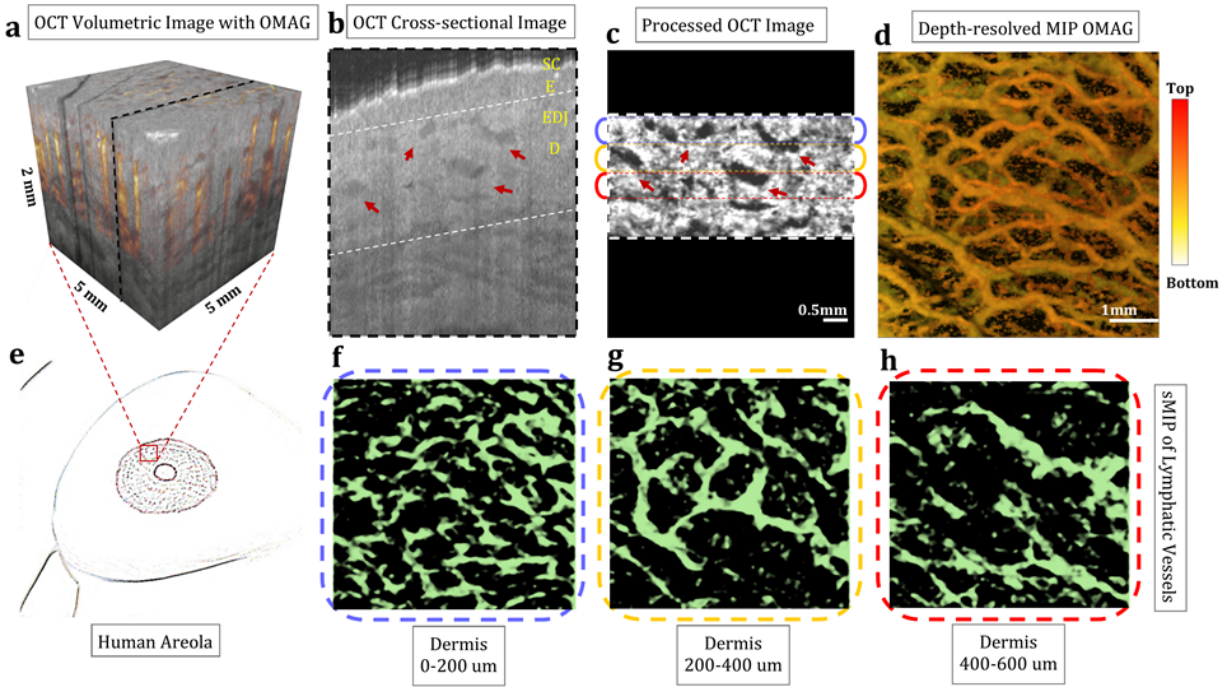

Figure 2.6. En face mapping of lymphatic vessels within human areola

(a) OCT volumetric structural image overlaid with volumetric OMAG acquired within in vivo human areola. (b) OCT cross-sectional image taken from the OCT volumetric data, pointed with dashed black line in (a). SC: Stratum Corneum, E: Epidermis, EDJ: Epidermal-dermal junction, D: Dermis. (c) Segmented and processed cross section of dermis, pointed out at (b) with white dashed lines. (d) En face OMAG image with depth-resolved MIP. (e) Sketch of human areola where OCT image is taken from. (f-h) En face sMIP of lymphatic vessels from 0-200 um of dermis (f), 200-400 um of dermis (g), and 400-600 um of dermis (h). Red arrows point out some of the lymphatic vessels seen as low-scattering (dark) regions. Field of view is 5 mm x 5 mm. (Baran et al. 2016)

2.2.5 *Discussion and Conclusion*

There are no truly non-invasive ways to assess the in vivo status of tumor induced lymphangiogenesis and to monitor the treatment modalities on lymphatics. Currently, subdermal injection of contrast agents is required for imaging lymphatic vessels in clinics, but they can create complications in patients so it is considered as significantly invasive in the clinical care as well as in the clinical research (Lee et al. 2015). Injection itself might also initiate an inflammatory response which in return affects the results. In addition, it only shows a specific pathway depending on the injection site.

Here, we succeeded to visualize lymphatic vasculature within human skin and areola in vivo, in the absence of exogenous contrast agents. We also observed the variations in the dynamics of lymphatic vessels in the case of inflammation that has been developed by acne vulgaris. To the best of our knowledge, this is the first study imaging the lymphatic system within human skin without any interventional radiology procedures. Our technique offers a unique ability to quickly visualize the microvascular and lymphatic response to stimulation, non-invasively. It may be used to image functional and constitutional changes through lymphangiogenesis and angiogenesis in the patients with cancer in response to tumor growth. OLAG results from subareolar lymphatic plexus may offer an opportunity for early diagnosis of carcinoma without using invasive methods.

Nevertheless, our method also comes with some limitations. Firstly, the current lateral resolution of our system was ~22 μm. This makes it harder to resolve small blood and lymphatic capillaries. However, with this resolution, this technique would be sufficient for comparison studies where errors in the measurements do not affect the differential conclusions. Secondly, hair follicles might create false positives due to their strong absorption to the OCT light source. Finally, although the accuracy of this technique has been shown and validated on mouse models before (Vakoc et al. 2009a; Yousefi et al. 2014), additional studies with histopathological comparisons have to be made with human subjects to further validate and refine OLAG for human skin.

Several improvements can be made to our methods in the future. Firstly, the spatial resolution of the system needs to be improved so that smaller blood and lymphatic vessels can be imaged. However, with the increase of the system resolution, there will be penalty paid to the depth of field of the system that would ultimately render a reduced ability to see deep vessels. This issue may be mitigated, on the other hand, by the use of dynamic focus control so that the lateral resolution can be maintained throughout the imaging depth without creating an out of focus image. Secondly, in

this study, we elected to image areas with few to none hair for the demonstration of proposed method. However, for haired skin, the histogram equalization method can be improved by selectively disregarding the areas with hair follicles in enface images, automatically. Finally, improving the accuracy of segmentation warrants further investigation for improved quantification of the results in various other applications aimed to understand the mechanisms how the lymphatic system responds to the disease or its treatment regimen.

In summary, we have reported an OCT based label-free optical lymphangiography for the first time within *in vivo* human skin and areola. We demonstrated the capabilities of this technique to image the microvasculature and lymphatic vessels within human skin up to capillary level without a need for exogenous contrast agents. The lymphatic circulatory system has important functions in immune surveillance and play a key role in several diseases. The currently available techniques require contrasting material being administered into human body, which can lead to complications. Label-free imaging of blood and lymphatic vessels with high resolution within human skin and areola using OMAG and OLAG may be useful in improving the patient care, and in addition, it could open up opportunities to better understand tissue response to various pathological cases such as inflammatory diseases and cancer, and consequently facilitating new treatment options targeting lymphatic system. More studies should be conducted to better understand the nature of lymphatic system's involvement in cases such as wound healing, diabetes, and autoimmune diseases.

Chapter 3. FUNCTIONAL OCT IN CLINICAL DERMATOLOGY

3.1 BACKGROUND AND MOTIVATION

The visual input has been the most important information for dermatologists in clinic. Typical diagnostic steps used in clinics (Abramovits and Stevenson 2003) are following: 1), recognition of patterns in the cutaneous tissue; 2), study of the patient history; and 3), analyses of tissue histopathology in laboratory through biopsy, if necessary. Because of its invasiveness and inconvenience, the skin biopsy is usually not desirable if not necessary. Hence, the first step of visualization of the skin is key to a comprehensive examination and accurate diagnosis. This approach is still commonly used by visual inspection of dermatologist using a magnified glass under "cold light", relying heavily on subjective assessment.

Recently, emerging non-invasive imaging methods such as dermoscopy (Kittler et al. 2002), confocal microscopy (González et al. 2003), and high resolution ultrasound imaging (Kumagai et al. 2012) offer a comprehensive set of tools that dermatologists can utilize for state-of-the-art patient care. Dermoscopy is the most popular imaging tool used in practice. It provides magnified images of skin up to papillary dermis using high-resolution prismatic loupes and a camera. It is typically used after the application of water drop with a faceplate to increase light penetration into tissue. Unfortunately, it only provides two dimensional images. On the other hand, the higher resolution (~1 um), three dimensional images of skin up to ~150 um depth can be acquired using confocal microscopy. High resolution ultrasound imaging can penetrate deeper into the tissue but usually cannot provide adequate resolution for accurate quantification. However, it can be useful in detecting abnormalities in the deeper layers of the skin, which would not be possible with the

previously mentioned methods. Still, an alternative non-invasive imaging technique with both high resolution and good penetration depth capabilities would be instrumental in dermatology clinics.

OCT has gained more and more attention in dermatology research. By delineating wound re-epithelialization, reformation of the dermoepidermal junction, and dermal remodeling (Cobb et al. 2006), OCT has been successfully used to study non-melanoma basal cell carcinoma (Gambichler et al. 2007), actinic keratosis (Mogensen et al. 2009), inflammatory diseases (Yano et al. 2004), to quantify structural changes in human skin during acne development (Baran et al. 2015d), and wound healing (Greaves et al. 2014).

In addition to its microstructural imaging capability, OCT signal can also be utilized to provide 3D blood and lymphatic angiography down to capillary level in tissue beds in vivo using methods called optical microangiography (OMAG) (Wang et al. 2007b), and optical lymphangiography (Yousefi et al. 2014), respectively. Over the past few years, OMAG technique has been intensively used to study in vivo microvasculature of a variety of biological tissues in pre-clinical and clinical settings.

The aim of this chapter is to further explore the feasibility of functional OCT in clinical dermatology use and demonstrate its potential and limitations. Here, microvascular and structural maps of healthy and abnormal human skin types are demonstrated in vivo, using OCT based techniques. The system and methods are described in Section 3.2. The experimental results are shown in Section 3.3-5. Section 3.6 provides a discussion of the implications of our results and the potential and future challenges for OCT in clinical dermatology, and concluding remarks.

3.2 System Description

We used a SS-OCT system to image microvasculature, structure and lymphatic network within human skin with various conditions. The OCT system uses a swept light source containing a

MEMS-tunable vertical cavity surface-emitting laser (VCSEL) (Fig. 3.1). This VCSEL source is able to sweep the lasing wavelength across a broad spectral range near 1310 nm at a fixed repetition rate of 100 kHz, giving a long coherence length (>50 mm) with 15 µm axial resolution in tissue and an extended imaging range (nominally ~12 mm in air). The output beam (28 mW in power) exiting from the VCSEL laser was fiber-coupled into a Mach-Zehnder interferometer built in the imaging module, where the light was evenly split into two beams by a 50:50 broadband fiber coupler that were directed to a reference arm and a sample arm, respectively. The sample arm was consisted of a probe imaging head (including a fiber collimator and X-Y galvanometric scanners) and a 5X objective lens (LSM03, working distance = 25.1 mm, Thorlabs Inc.), giving 22 µm lateral resolution. The probe was attached to an articulating arm to make it easy to access to a sample (Fig. 3.1a). In order to mitigate strong specular reflection from the skin surface, a mineral oil was topically applied to the skin surface. The optical power of incident light upon the sample was ~5.2 mW well below the American National Standards Institute (ANSI) standards (Z136.1) for the safe use of near infrared light at 1310 nm.

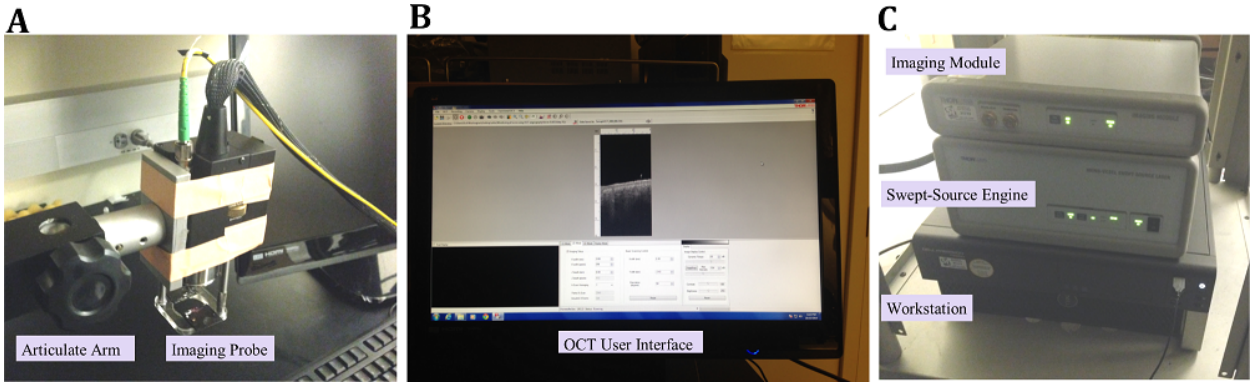

Figure 3.1. Swept-source OCT system for in vivo human skin imaging.

Photographs of the swept-source OCT (SS-OCT) system used for in vivo human skin imaging. (a) Picture of the probe attached to the articulating arm. (b) User interface of the SS-OCT system. (c) Portable bench top SS-OCT system on the wheeled cart. (Baran et al. 2015b)

For vascular mapping of the skin tissues, we utilized the algorithms of OMAG (An et al. 2011) and correlation mapping masked OMAG (Choi et al. 2014a). As the scanning protocol, 3D OCT imaging was performed on human skin using a raster scanning of the galvanometric scanners. For fast B-scan (in X direction), a B-frame contained 256 A-lines. In the slow C-scan (in elevational Y direction), total of 2048 B-frames were captured with 8 repetitions at the each location, which took ~20 s with a 100 frames/s imaging rate. A cross-correlation-based image registration method was applied for the adjacent B-frames in the 3D amplitude data set to compensate axial displacement induced by possible tissue bulk motion. To acquire a large field of view, this imaging protocol was repeated to create a mosaic image.

Subject volunteers were used in this study to demonstrate the usefulness of OMAG to delineate skin microvascular features in normal skin and skins with pathological conditions. The use of OCT/OMAG laboratory instrumentations on volunteer subjects was reviewed and approved by the Institutional Review Board of the University of Washington, and informed consent was obtained from all subjects before imaging. This pilot study followed the tenets of the Declaration of Helsinki and was conducted in compliance with the Health Insurance Portability and Accountability Act.

3.3 OCT IMAGING OF HEALTHY HUMAN SKIN IN VIVO

3.3.1 *OCT Imaging of Human Nailfold*

We firstly demonstrate imaging human nailfold using OCT. It is a good choice of sample for vascular imaging because of easy access and well-known vessel morphology of which disposition is in parallel to the skin surface as opposed to other tissue vascularity normal to the surface (Cutolo et al. 2003). In particular, we examined nailfold of fourth finger (ring finger) because of greater transparency of the skin (Cutolo et al. 2003). A healthy volunteer was comfortably seated at room temperature and his left hand was placed onto the sample stage under the scan lens for imaging.

Figure 3.2 shows OCT imaging result of the nailfold of fourth finger. A representative OCT structural cross-section (Fig. 3.2(a)) delineates internal layers of proximal nailfold such as stratum corneum (SC), dermis (D), nail matrix (NM) and root of nail (RN). Corresponding blood flow image is shown in Fig. 3.2(b) in which bright signals are attributed to blood perfusion through functional capillaries and small vessels. To visualize vessel network of the nailfold, the vasculature was reconstructed from 3D OCT angiography dataset using a rendering software coded with Matlab language to create en face image. Figs. 3.2(d-f) are en face images (2mm × 2mm) of 3D rendered vasculatures obtained from three different depth ranges (280μm-430μm, 430μm-600μm, 600μm-880μm), representing nail bed networks in depth. At the papillary dermis below the SC (280μm-430μm), it is observed that hair-pin looking capillary loops are regularly distributed and oblique to the skin surface (Fig. 3.2(d)) (Smith et al. 2013). At deeper dermis (430μm-600μm and 600μm-880μm), arborizing vessel plexus is visible, branching into finer secondary vessels and the capillary loops (Figs. 3.2(e) and 3.2(f)). Overlay of Figs. 3.2(d-e) with different colors (green, blue, and red, respectively) delineates typical vessel morphology of normal nailfold in Fig. 3.2(c).

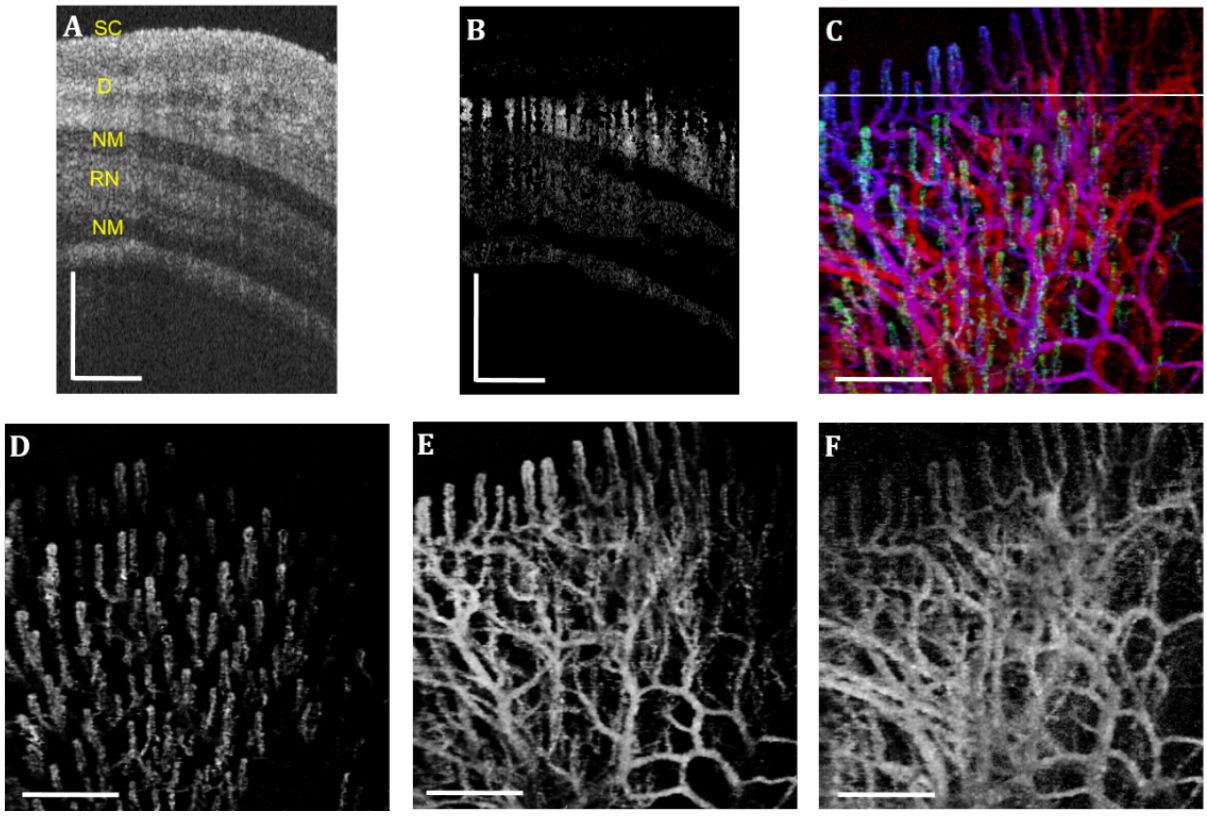

Figure 3.2. OCT imaging of healthy human nailfold *in vivo*.

(a) A representative OCT structural cross-section of nailfold of fourth finger. SC, stratum corneum; D, dermis; NM, nail matrix; RN, root of nail. (b) A blood flow image corresponding to (a). (c) Color coded en face OCT angiography image where the horizontal line indicates the location of (a) and (b). (d-f) En face images of vasculatures obtained from different depth ranges: (d) 280µm-430µm, (e) 430µm-600µm, (f) 600µm-880µm. Scale bars represent 0.5 mm. (Baran et al. 2015a)

3.3.2 *OCT Imaging of Human Facial Skin*

We further imaged a facial skin of another healthy volunteer using our OCT system. In this work, we employed handheld probing scheme for easy access of light beam to the facial regions. For forehead imaging, the subject laid in supine position on a mattress with his head on a pillow and then the handheld OCT probe was gently touched on the forehead. However, the cheek imaging of the subject in seated position was conducted with contact mode of the same OCT probe. A top panel of Fig. 3.3 represents *en face* structure image of forehead (a), its vasculature image (b), and their overlay (c), respectively. From the overlaid image in Fig. 3.3(c), it is noted that hair follicles

are encircled by small vessels to possibly supply nutrients necessary for hair growth. Likewise, a bottom panel of Fig. 3.3 shows *en face* structure image of cheek (d), its vasculature image (e), and their overlay (f), respectively. Unlike in Fig 3.3(b), vessels appear larger in diameter and less dense in Fig 3.3(e). Multiple horizontal lines on the cheek angiogram (Fig. 3.3(e)) are image artifacts, which were caused by either involuntary head motion of the subject or hand shaking of the observer or both of them during imaging. Field of view of all images is 3mm × 3mm.

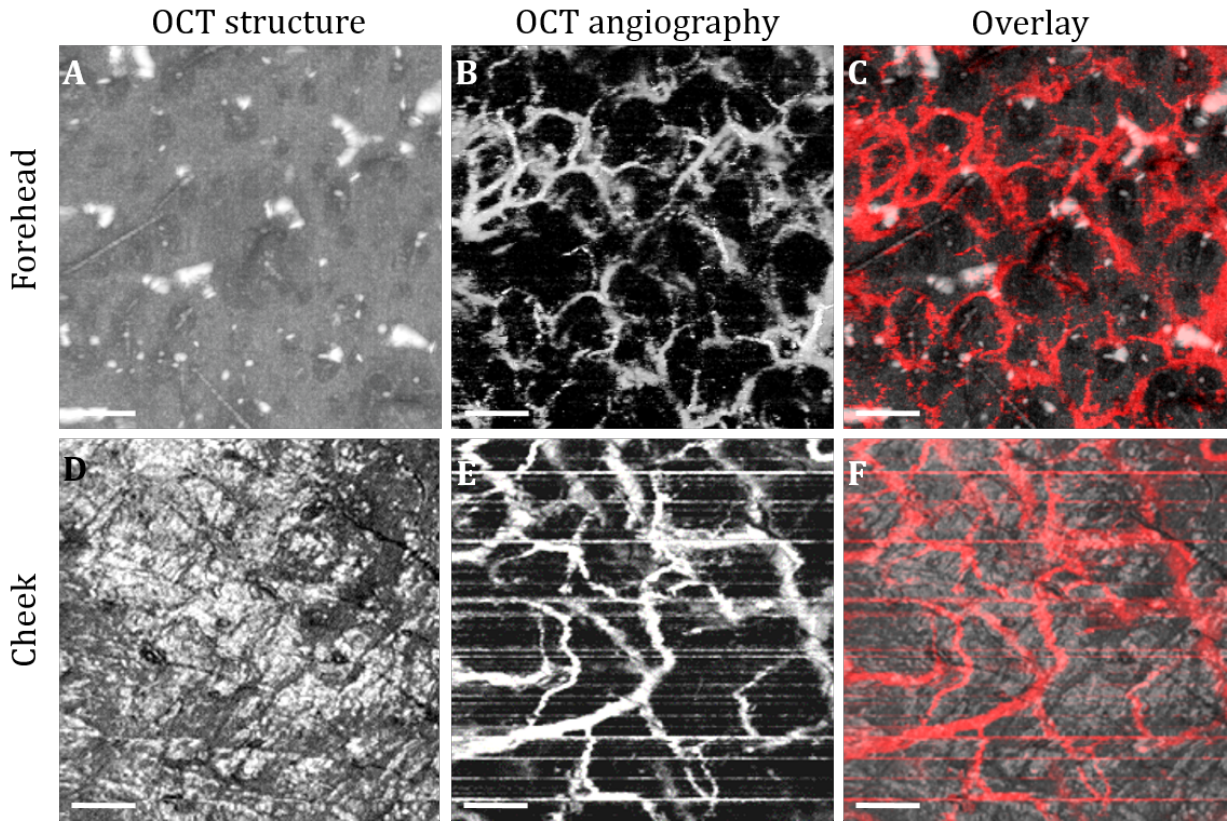

Figure 3.3. OCT imaging of healthy human facial skin *in vivo*.

Top panel: (a) En face structure image (3mm ×3mm) of forehead, (b) Its corresponding vasculature image, (c) Overlay of (a) with (b). Bottom panel: (d) En face structure image (3mm × 3mm) of cheek, (e) Its corresponding vasculature image, (f) Overlay of (d) with (e). Scale bars represent 0.5 mm. (Baran et al. 2015a)

3.4 OCT Imaging of Inflamed Human Skin In Vivo

During inflammation, the lymphatic drainage is activated along with the vascular remodelling. Therefore, the monitoring of a simple inflammation phenomenon could be a good surrogate for demonstrating the usefulness of the proposed OLAG technique (Section 2.2). Here, human skin's inflammatory state and its recovery are monitored for 7 days within an acne lesion using OMAG and OLAG and shown in Fig. 3.4 and Fig. 3.5. In these figures, the results for certain days are presented in each row. Accordingly, photograph, depth-resolved MIP OMAG, and the OLAG images from various depths are included in this figure. Field of view for OCT imaging is 5 mm x 5 mm.

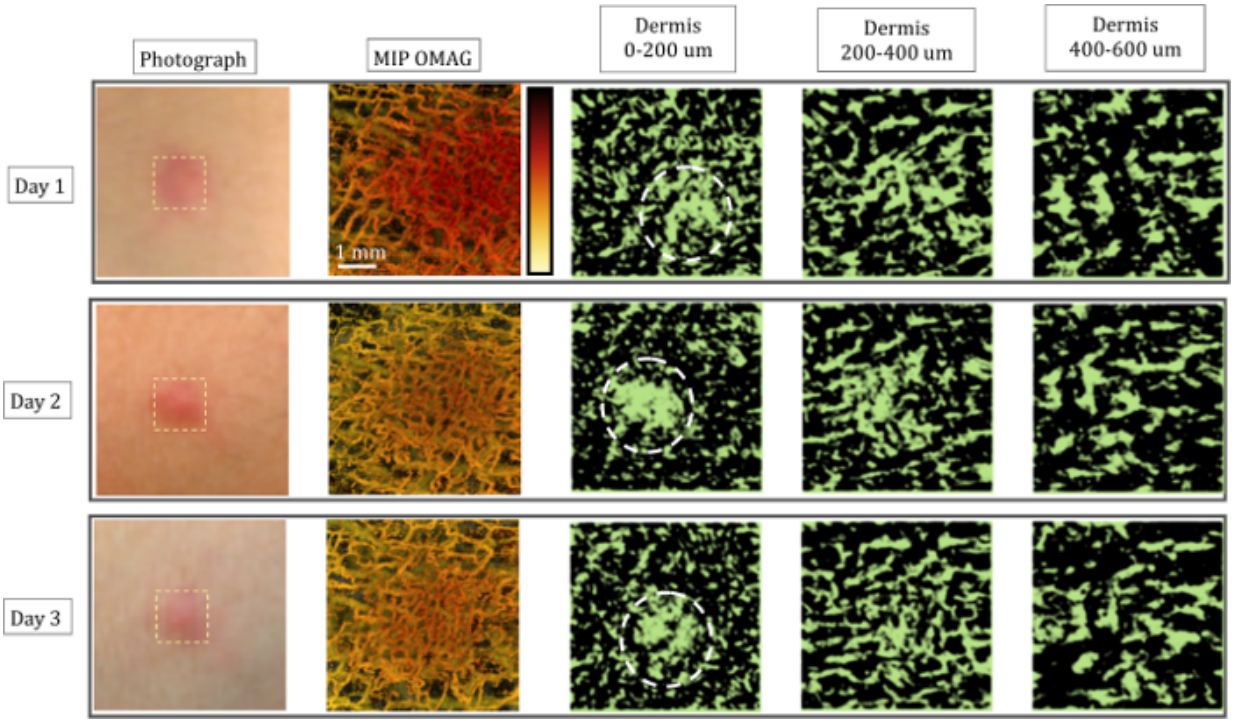

Figure 3.4. Monitoring inflamed human skin *in vivo* using OLAG and OMAG.

En face depth-resolved MIP of OMAG and sMIP of OLAG images with 5 mm x 5mm field of view are shown for day 1, 2, and 3 of acne lesion development. Blood vessels are color coded according to their position in depth and lymphatic vessels are shown in green. Imaged areas are pointed out on photographs of acne lesion. While circles are highlighting the areas with edema. (Baran et al. 2016)

The volumetric depth-resolved MIP of OMAG images clearly show the changes in microvascular activity within the region of interest. In the first 3 days, inflammation causes edema in the tissue, which is circled in Fig. 3.4. Edema region consists of inflammatory cells and water. Since there is less light scattering in this region compared to surrounding tissue, it looks darker on the OCT image, and hence appearing as an artifact in the final en face OLAG image. However, it can be differentiated from the lymphatic vessels since it is not part of the connected network. On the other hand, lymphatic vessel network is very active during the inflammatory state of acne development and lymphatic vessel density decreases as acne lesion heals, as shown in Fig. 3.5b.

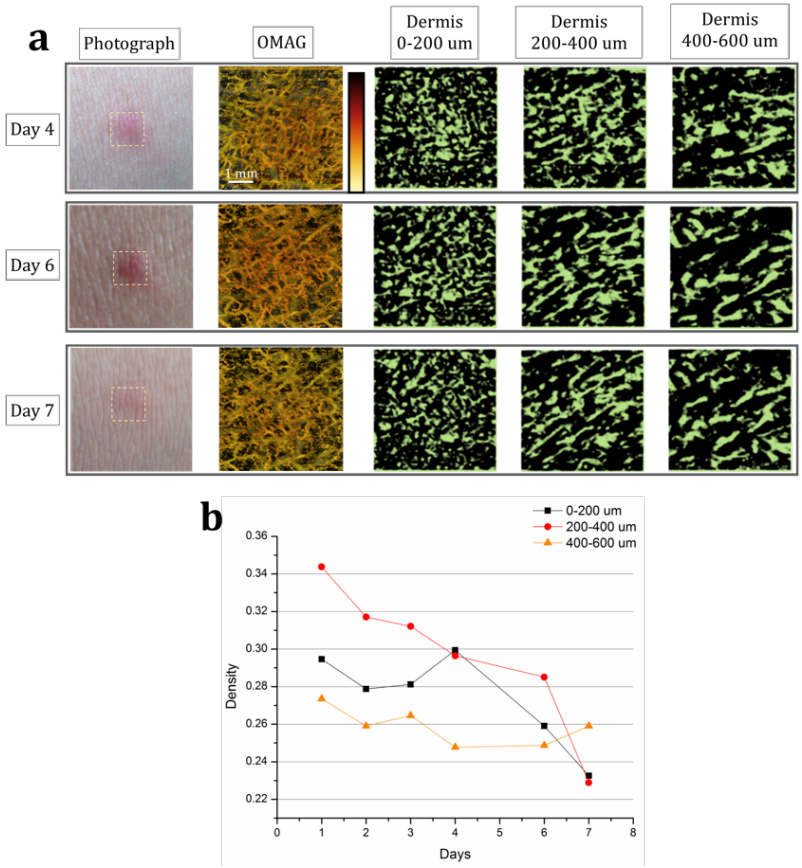

Figure 3.5. Monitoring healing human skin *in vivo* using OLAG and OMAG.

(a) En face depth-resolved MIP of OMAG and sMIP of OLAG images with 5 mm x 5mm field of view are shown for day 4, 6, and 7 of acne lesion development. Blood vessels are color coded according to their position in depth and lymphatic vessels are shown in green. Imaged areas are pointed out on photographs of acne lesion. (b) Comparison of lymphatic vessel density change observed in OLAG images for different layers over 7 days (n=4). (Baran et al. 2016)

Breakage of dermal balance and inflammatory response leads to dense microvasculature in Fig 3.4, by activating the reserve blood vessels during the inflammatory stage of acne development (Baran et al. 2015b). With the decreased inflammation at day 4, blood and lymphatic vessel densities decrease and eventually go back to normal as shown in Fig. 3.5.

In this study, we observed structural changes in the lymphatic vascular system over time during inflammation and monitored lymphatic flow changes in the skin as a result of new vessel formation (Fig. 3.4-5). Since the similar changes are observed in the inflammatory disorders, these results give an opportunity to assess these diseases in the level of diagnosis, course and the response to the treatment. The grade of lymphatic vascular activation can be a biological marker for the severity and activity of these chronic inflammatory skin diseases. Therefore, we would expect that the ability of OLAG to delineate the lymphatic vessels in vivo, at the level of capillaries, could provide useful quantitative metrics for monitoring and assessing the consequences of treatment in these disorders.

3.5 HIGH RESOLUTION IMAGING OF PATHOLOGICAL HUMAN SKIN

3.5.1 *OCT Imaging on Pathological Skin at Various Parts of Human Body*

There has been growing evidence suggesting that microvasculature plays a predominant role in pathogenesis of skin conditions such as acne, psoriasis, and skin cancer (Braverman 2000). To improve our understanding of the involvement of vascular abnormality in skin conditions, visualization and identification of vessels with a characteristic morphology are essential to assess many types of skin lesions. Hence, there is a need of noninvasive imaging tool to visualize the tissue microcirculation. In Sec. 3.3, functional imaging ability of OCT on human skin tissues is shown, allowing us to observe the vascular features of various normal skin tissue beds *in vivo*. In this section, the functional OCT imaging is expanded to the underlying skin conditions to explore vessel morphology in the cutaneous lesions.

Figure 3.6 shows OCT imaging results of three types of cutaneous conditions; acne, papules, and nevus, taken from different individual subjects. First to fourth columns of each panel in Fig. 3.6 represent a picture including the skin lesion, OCT structure image of the lesion (3mm × 3mm), corresponding OCT angiogram (3mm × 3mm), and their overlay. In the first panel, a picture shows acne at early stage, appearing small elevation of reddish skin. It has a pustule, containing a purulent material consisting of necrotic inflammatory cells. The OCT structure image is similar to the acne appearance in the picture. The OCT angiogram reveals a microvessel network in the acne region, consisting of dotted vessels corresponding to papillary dermal vessel and complex upper dermal plexus. Note that the OCT angiography signals were not observed at the pustule, implying no functional blood vessels innervating this region, probably due to that the fluid in pustule may be stagnant with limited Brownian motion of inflammatory cells.

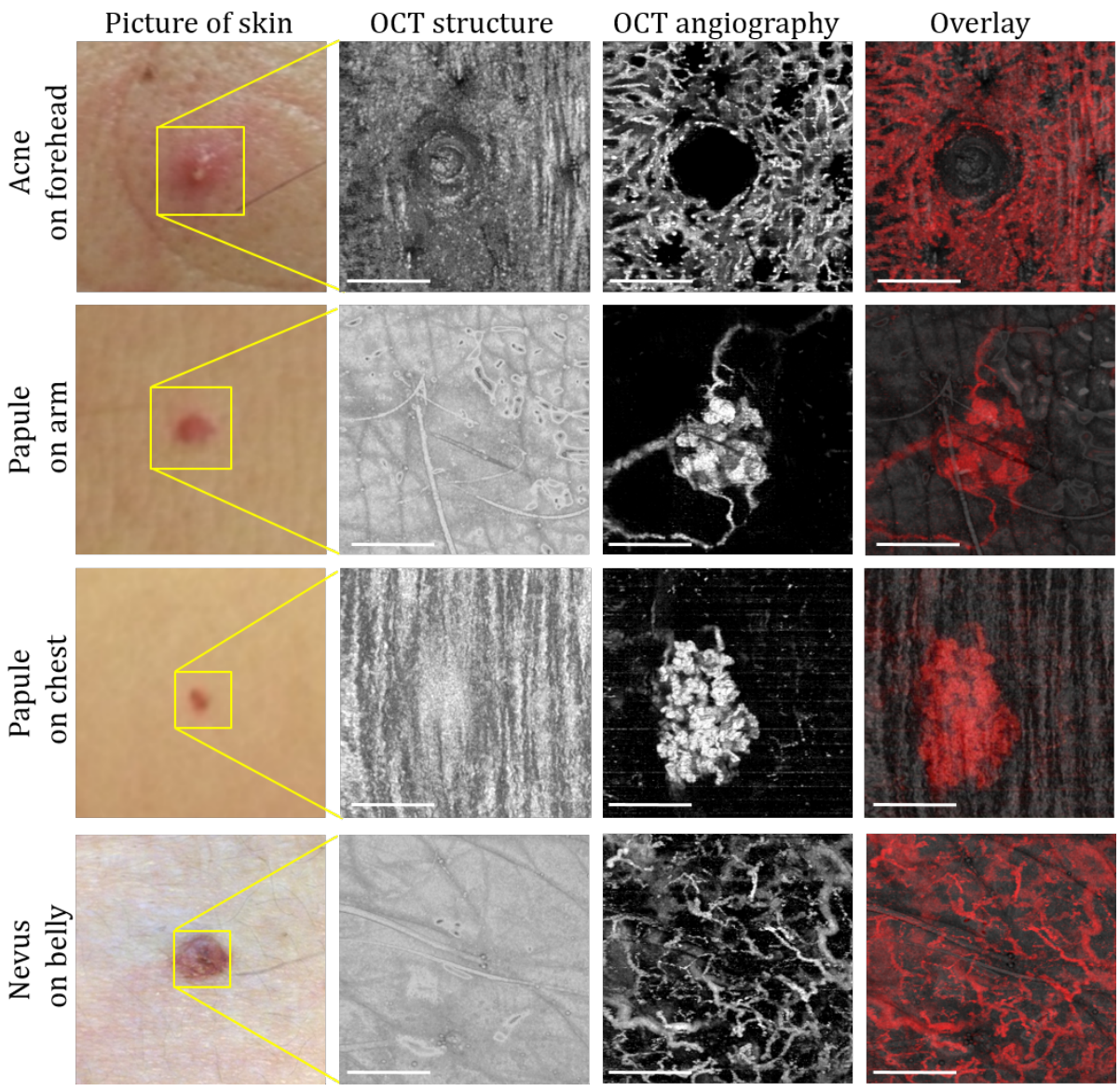

Figure 3.6. OCT imaging of different skin lesions on human body *in vivo*.

Top panel: acne on forehead. Second panel: red papule on arm. Third panel: red papule on chest. Bottom panel: nevus on belly. First to fourth columns for each panel are photograph of the skin lesion, OCT structure image, corresponding blood flow image, and their overlay, respectively. Size of all images (except for pictures) is 3mm × 3mm and scale bars represent 1.0 mm. (Baran et al. 2015a)

Second and third panels in Fig. 3.6 show papules on arm and chest, appearing circumscribed, raised reddish spots on the skins with distinct borders as shown in pictures and OCT structure images. In their OCT angiograms, it is interesting to observe the vessel distribution patterns. The appearance of blood vessels in the papule on arm (second panel) is thick, irregular in shape with

minimal branching. However, vessels in the papule on the chest (third panel) look curled up and clustered through the lesion, resembling the glomerular apparatus.

Furthermore, nevus was examined on a subject's belly and its OCT results are described at bottom panel in Fig. 3.6. Nevus is an unusual benign mole with distinct boundary that may resemble melanoma (Arumi-Uria et al. 2003). In the OCT angiogram, the vascular pattern of nevus was identified having irregular linear vessels that barely branch, which gives a favorable agreement to a result by classical dermascopy (Martín et al. 2012).

3.5.2 *Monitoring Acne Development and Scarring on human skin*

Acne scarring involves microvascular changes and fibrosis in the initial acne lesion. To understand the transition from acne lesion initiation to scarring, longitudinal changes in a selected acne lesion is monitored using OMAG. Fig. 3.7 shows the structural and microvasculature changes in the acne lesion throughout 51 days. In Fig. 3.7, the results from each day are arranged in clusters, in which photograph image (upper left), en-face AIP (upper right), depth-encoded en-face MIP of microvasculature (lower left) and MIP of microvasculature (lower right) of the acne lesion are given and compared to those from the other days within the natural development of the acne lesion and scarring.

Moreover, to provide quantitative biomarker about acne scarring, vessel density is calculated for each day and plotted in Fig 3.7. To calculate the vessel density changes, vessel segmentation algorithm (Reif et al. 2012) is applied to each en-face MIP blood flow image. Briefly in this method, MIP images of microvasculature are binarized, and vessel density is calculated by dividing the number of ones with the total pixel number. Consistent with the wound healing process, after the damage caused by the inflammation, vascular density in the acne region increases at the early development stage and then decreases at the later stage.

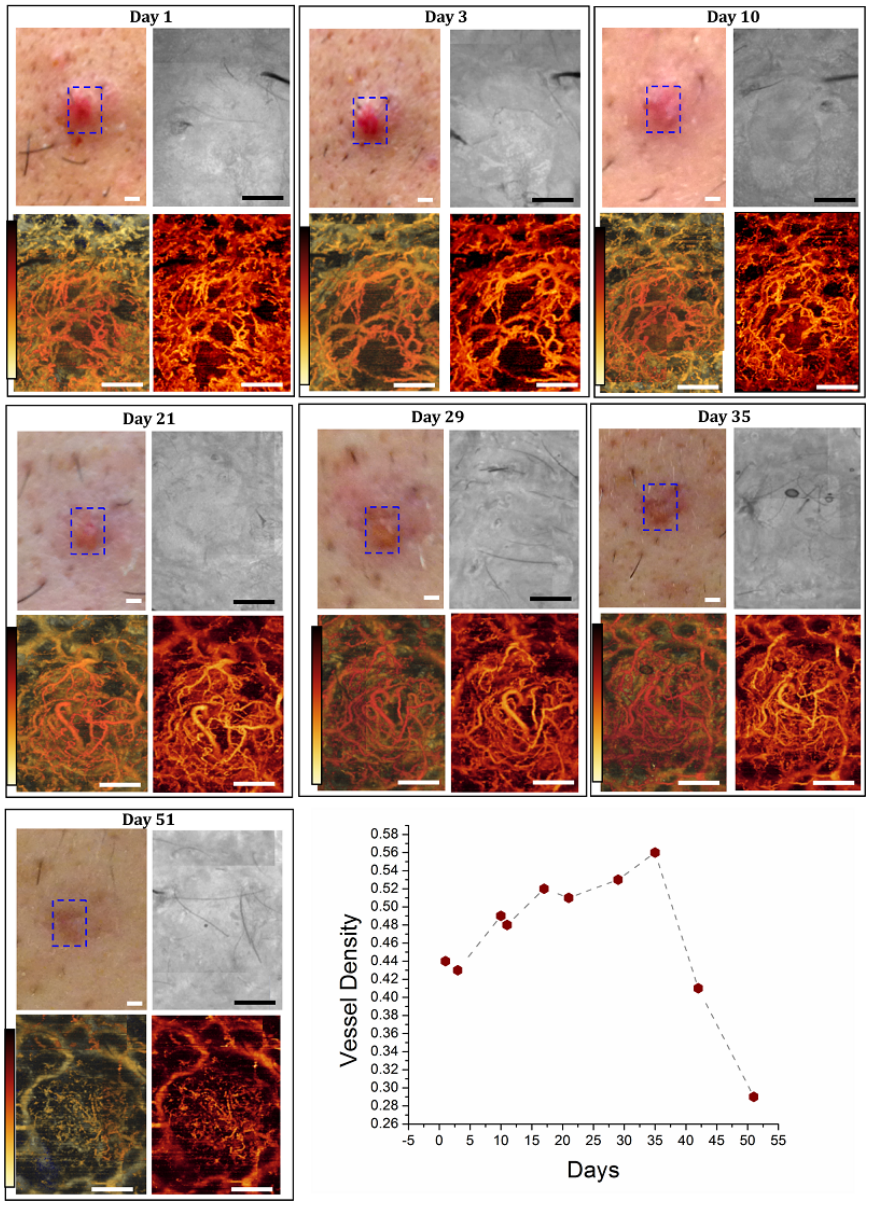

Figure 3.7. Monitoring development of acne lesion over 51 days *in vivo* using OMAG.

En face MIP images of microvascular and structural changes within acne lesion on human facial skin over 51 days. Bottom right figure shows the vascular density change in the MIP images of microvasculature over time. Scale bar represents 1 mm. (Baran et al. 2015b)

At the day 51, Fig. 3.7 shows that the acne lesion turns into a scar. The en face MIP of volumetric microvasculature image shows that the vessel density in the original lesion area is

decreased to a level similar to the surrounding healthy area. On the other hand, the en face MIP of OCT structural data of the lesion appears more uniform compared to the previous stages.

3.5.3 *Monitoring Wound Healing on human skin*

Disruption of cutaneous epidermal-dermal continuity is defined as a wound. Following the occurrence of a wound, skin integrity is rapidly restored through multiple interrelated overlapping biological phases known as inflammation, cellular proliferation and maturation. During the healing process, characteristics of structural and microvascular changes in the tissue are unique to each stage of healing.

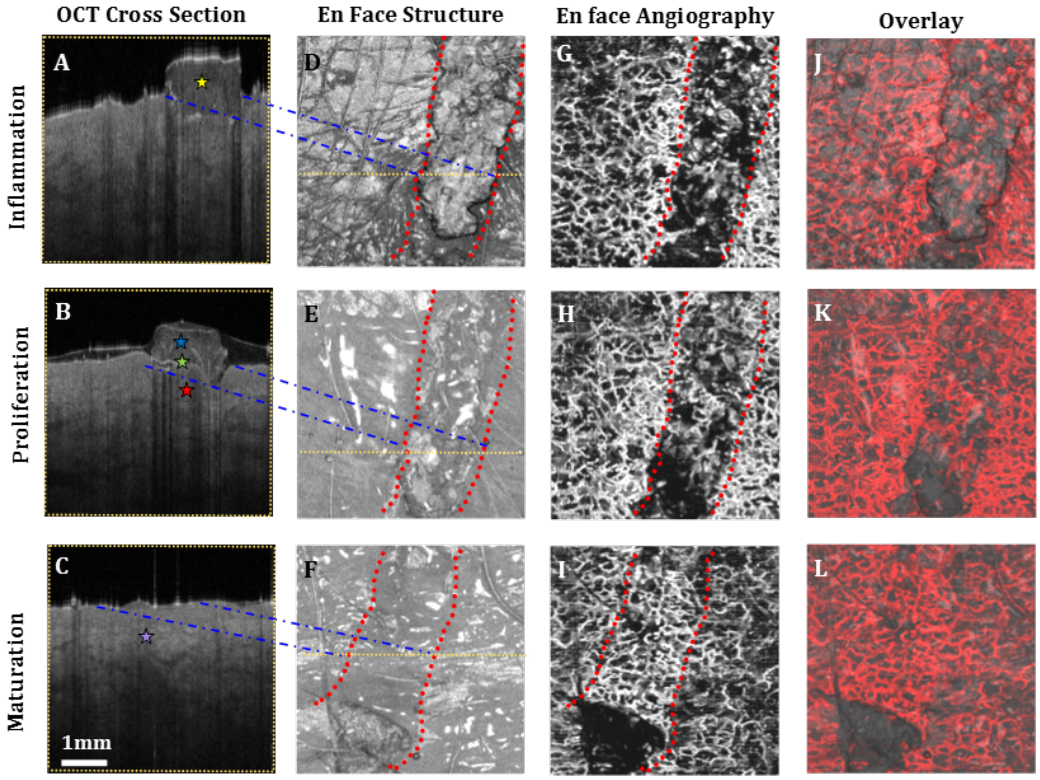

Figure 3.8. OCT imaging of wound healing within human skin over 10 days *in vivo*.

(a-c) OCT cross sectional views of the areas marked with yellow dashed lines in en face images (d-f). In (a), yellow dot points to inflammatory edema formation. In (b), blue, green and red dots point to haemostatic crust, re-epithelialization, and dermal regeneration, respectively. In (c), purple dot points to healed dermal layer. (d-f) MIP of OCT en face structural images. (g-i) OMAG MIP of microvasculature at 0–1 mm depth. Red dotted lines show the wound area. (j-l) Overlay of (d-f) with (g-i). (Baran et al. 2015a)

The OCT images of a wounded human skin during healing stages are shown with great detail in Fig. 3.8, thanks to the large field of view (5 mm x 5 mm). Here, cross sectional OCT images in Fig. 3.8(a-c) show the structural remodeling in the epidermis and dermis. OCT en face structural (Fig. 3.8(d-e)) and microvascular images (Fig. 3.8(g-i)) are used to better visualize and locate the wound lesion borders. In the early stages of wound healing microvasculature is sparsely organized in wound region than those in the surrounding normal tissue as shown in Fig. 3.8(g, h), however it becomes progressively denser in the maturation stage. Structural images are merged with the microvasculature and shown in Fig. 3.8(j-l).

3.6 Discussion and Conclusion

Cutaneous wound is usually created as a result of damage to the skin after an injury, and its healing process consists of overlapping multiphase processes including hemostasis, inflammation, tissue formation, and tissue remodeling. Understanding this complicated healing process and developing strategies for better wound healing outcomes have been active fields of research (Menke et al. 2007). Various growth factors such as vascular endothelial growth factor (VEGF), transforming growth factor-b (TGF-b) and fibroblast growth factor (FGF) are currently attracting clinical interests to promote the healing process (Frank et al. 1995). OCT microangiography could provide direct visualization and quantification of the in vivo microvascular changes during wound healing and may be utilized in the studies involving these growth factors. Similarly, it may also be applied to other studies with topical drugs and stem cell therapies, in which OMAG can serve as a real time monitor tool to provide feedbacks to the treatment strategy about the therapeutic effects on wound healing, thus improving the treatment outcomes.

Furthermore, cutaneous microcirculation is usually first to malfunction in several diseases such as primary Raynaud's phenomenon (Tooke 1995), systemic sclerosis (Sulli et al. 2008), port wine stain (Liu et al. 2013), psoriasis (Qin et al. 2011), and skin cancer (Johnson and Wilgus 2012). With OMAG, vessel density of various parts of the normal and abnormal skins can easily be calculated (Reif et al. 2012), and used as a prognostic or diagnostic marker to assess progression and regression of the skin lesions, replacing a standard visual inspections. Various non-invasive microvascular reactivity tests have been utilized in clinics i.e. mechanical/thermal/electrical stimuli (Minson 2010) or subdermal injections of pharmacological agents (Cracowski et al. 2006). However, due to the limitations of the current available blood perfusion imaging techniques such as laser Doppler imaging (Clark et al. 1999) and laser speckle contrast imaging (Roustit et al.

2010), they are often used to provide gloss assessment of skin blood perfusion. OCT microangiography would make these tests possible to be assessed more accurately and objectively with its unprecedented capability of visualizing detailed microvascular network innervating skin tissue, at a level of capillary vessels.

Although OCT technology has made great progress over the last decade, there are still some caveats. Firstly, motion induced noise can deteriorate the angiography quality significantly. The use of a vacuum cushion is a simple, commonly-used method to limit the motion at the hand and forearm, but a motion tracking systems should be employed for clinical dermatology applications on other parts. Moreover, the limited penetration depth of OCT prevents its applications from imaging the desired location that is more than 2 mm in depth. Luckily, the development of endoscopic probes using MEMS scanners (Holmstrom et al. 2014) are surging and it can extend the use of OCT in clinics.

Based on the presented results, functional OCT methods promise significant advantages compared to alternative imaging methods used in clinical dermatology. Here, we have shown the use of OCT on different parts of human body, with or without abnormality, and demonstrated the capabilities of OMAG for better visualization of cutaneous wound healing process on human. Future well-designed clinical studies will be required to systematically investigate and establish the benefits of this technology, contributing to the clinical management and improvement of new treatment alternatives.

Chapter 4. FUNCTIONAL OCT IN NEUROSCIENCE

4.1 Review of OCT-Based Angiography Methods for Neuroscience

4.1.1 *OCT Imaging of Healthy Rodent Brain*

The cortex of the brain is layered, and each layer contains various neuron sub-types and different input or output connection to the other regions of the central nervous system. The blood supply to the cortex include large vessels over the surface of the brain and smaller diving vessels that penetrate almost perpendicularly to the surface to feed the dense networks of capillaries in deeper layers (Harrison 2002). The capillary beds deliver blood to vital parts of the cortex that are metabolically active during neuronal firing. The signals observed in superficial arteries and veins are related to the in-flow and out-flow of blood to these capillary beds and can have a different behavior compared to their capillary counterparts. The dynamics of the capillary responses are most interesting given that they are expected to be more closely related to the functional behavior of the responding neurons.

First demonstration of FD-OCT based angiography on a rodent cerebrovascular model was made in 2007 using OMAG technique (Wang et al. 2007b). Here, Wang et.al demonstrated the capabilities of OMAG technique for visualizing microvasculature in the brain cortex of mouse models using 820nm (Wang et al. 2007b) and 1300nm (Wang and Hurst 2007) central wavelength light sources. Due to the enhanced imaging depth provided by the latter light source, OMAG was able to visualize pial vessels with the scalp left intact (Wang and Hurst 2007). However, due to the sensitivity limitation in the original OMAG protocol, capillaries were not distinguished clearly.

In 2009, Vakoc and Lanning et.al presented a comprehensive view of mouse cerebral vasculature bearing a human glioblastoma tumor through a cranial window using phase based OCT angiography (Fig. 2c), and combined these results with multi-photon microscopy images (Vakoc et al. 2009b). Here, the smallest superficial capillaries were visualized with multi-photon microscopy, and OCT angiography provided superior view of vessels deeper within the central regions of the tumor and in regions where fluorescent tracers leaked outside of vessels. However, relatively slow frame rate (~16 Hz) was used to be able to capture slow flow in this work, which can be problematic for time-sensitive experiments.

Following year, real time imaging of cerebral microvasculature became popular using high-pass filters on complex signals as explained in Section 1.2.1. Thanks to the higher sensitivity provided by UHS-OMAG, Yali et.al managed to visualize cerebral microvasculature up to capillary level within the meninges and cortex in mice with the cranium left intact (Jia et al. 2010). Using a thrombotic mouse model, longitudinal measurements of meningeal vascular responses to the insult and the responses in the cortex are provided (Jia and Wang 2010).

In addition, Srinivasan et al. utilized high-pass filtered intensity based OCT angiography for rapid comprehensive imaging of the surface pial vasculature and capillary bed in cerebral cortex through a cranial window in approximately 12s (Srinivasan et al. 2010a). Benefiting from the higher quality images provided by the cranial window, the authors were able to study the changes in vessel diameters and connections during hypercapnia. Similar work also monitored microcirculation responses during hypoxia through intact skull (Jia et al. 2011b).

Although high quality angiograms are useful to detect changes in the microvasculature, quantitative cerebral blood flow (CBF) information is needed in most cases to draw clinical implication. Srinivasan et al. utilized Doppler OCT to calculate total CBF and velocity changes in

the rat cortex (Srinivasan et al. 2010b). By the use of a popular method in Doppler ultrasound community (Gill 1985), the authors demonstrated that the total blood flow within a vessel can be evaluated by integrating en face Doppler signals, which does not require explicit knowledge of Doppler angles. Their measurement in rat somatosensory cortex yielded average blood flow of ~1.07 x 10^{-3} ml/mm^2/min, which is consistent with results acquired using autoradiography in similar rats and anesthesia conditions (Nakao et al. 2001). Using this method, they also compared CBF changes with simultaneous hydrogen clearance in rats (Srinivasan et al. 2011).

However, typical Doppler OCT methods suffer from limited dynamic velocity range and necessary sensitivity to measure capillary flows (see Section 1.2.2). To overcome the first limitation, Shi et.al (Shi et al. 2013) proposed a wide velocity range DOMAG to visualize fast and slow flows within one scan in a mouse cortex. Using this method, the authors demonstrated that using multiple velocity ranges a comprehensive map of blood flow dynamics can be acquired without sacrificing sensitivity for slow flow and dynamic range for fast flow. Moreover, You et.al presented a phase summation method to enhance slow capillary flow detection sensitivity, using Doppler OCT (You et al. 2014). Using this method, they studied the blood flow response in cortex to cocaine administration up to capillary level. Accordingly, they discovered a decrease of blood flow velocity within capillaries from 0.31 mm/s in control mouse, consistent with (Kleinfeld et al. 1998), to 0.15 mm/s in the chronic cocaine mouse even though there were no significant changes in capillary density.

RBCs pass one by one in cerebral capillaries, often with a large separation between them. This makes it hard to accurately quantify the RBC flux in capillaries using Doppler OCT methods. To address this problem, Lee et.al proposed new methods recently (See Section 1.2.4). Benefiting from these methods, they mapped heterogeneous flux distribution in cerebral capillaries with the

mean RBC flux of ~20 RBCs/s in healthy rat brain, similar to (Ren et al. 2012). The dynamic range of RBC flux is a function of the time gap between measurement points, in this case the frame rate. The upper limit in the measured capillary RBC flux in these studies (40 RBCs/s) were relatively lower than those in the literature where the reported values range from 40-45 RBC/s (Stefanovic et al. 2008a) to 80 RBC/s (Kleinfeld et al. 1998). Considering this high variability across the literature, possibly due to the differences in the animal species, anesthesia and physiology, higher frame rates should be utilized for more accurate RBC flux estimations.

Over the last few years, multi-modal imaging systems are proposed to combine advantages of OCT with other imaging modalities. Dziennis et.al used dual wavelength laser speckle contrast imaging (DWLS) as a guiding tool for OMAG (Dziennis et al. 2015). Here, DWLS enabled rapid prediction of infarct area and hemoglobin oxygenation over the whole mouse brain, and OMAG system the detailed information about blood perfusion dynamics down to capillary level in a region of interest pertaining to ischemia. Recently, Gagnon et al. combined two-photon laser scanning microscopy (TPLSM) angiography with Doppler OCT to acquire a more accurate 3D volumetric blood flow map by reconstructing TPLSM angiogram from the model with constraints from the Doppler OCT measurements (Gagnon et al. 2015). Moreover, TPLSM is also utilized in other studies to confirm the accuracy of capillary measurements of OCT angiography images (Wang et al. 2014).

4.1.2 *OCT Imaging of Rodent Brain during Stroke*

Stroke is caused by blockage (ischemic) or rupture (hemorrhagic) of a blood vessel within the brain. This injury leads to a series of functional and structural changes that may result in an infarct or a peri-infarct brain tissue. The peri-infarct tissue region, also called as penumbra, is potentially recoverable if it can be identified and treated appropriately. Cells often work in synchrony as a

neurovascular unit in response to stroke. To improve the understanding of this complex response and to develop better strategies to help recover from stroke, OCT angiography has been utilized over the last few years to study real time vascular dynamics in vivo on rodents after stroke.

The most common stroke model used on rodents is the intraluminal middle cerebral artery occlusion (MCAO). Accordingly to this model, a nylon filament with a silicone-coated tip is inserted into the right internal carotid artery via the external carotid artery until it blocks middle cerebral artery. Three years after the introduction of OMAG, Yali et al. (Jia and Wang 2011) presented the first preliminary stroke study using OCT angiography. They imaged both ipsilateral and contralateral sides of MCAO through intact skull on mice. Here, it was observed that the occlusive components of ischemic stroke still existed in the ipsilateral side after reperfusion from MCA. A more comprehensive study of vasodynamics after focal stroke was presented by Srivinasan et.al. The authors used a multi-parametric OCT platform for longitudinal imaging of ischemic stroke in mice, through thinned-skull (Srinivasan et al. 2013a). Capillary non-perfusion, CBF deficiency, and altered cellular scattering were quantified and correlated with histology. On the other hand, Yu et al. applied photodynamic therapy to study dynamic blood circulation before and after a localized ischemic stroke in a mouse model using Doppler OCT (Yu et al. 2010).

Developments in OCT angiography paved a way to several discoveries in stroke recovery research over the last couple of years. Berny-Lang and Hurst et.al managed to increase neurological outcome after stroke by administrating thrombin mutant W215A/E217 to mice (Berny-Lang et al. 2011). Later, Sun et.al utilized UHS-OMAG to reveal that conditional ablation of neuroprogenitor cells does not affect the functional blood flow during reperfusion, one hour after stroke, although it impeded the recovery of cognitive function (Sun et al. 2013). Moreover, another study showed that impaired collateral status due to diabetes leads to a worse stroke

outcome, and modulation of collateral flow has beneficial effects on these subjects (Akamatsu et al. 2015).

4.1.3 *OCT Imaging of Rodent Brain after Injury*

Traumatic brain injury (TBI) often causes alterations in cerebral blood flow, which are thought to influence secondary pathophysiology and neurologic outcome in human brain. Inadequate cerebral blood flow is an important contributor to mortality and morbidity after TBI; however, it is poorly studied. The ability to noninvasively map the variations of cerebral blood flow over a long period of time using OCT angiography would contribute to the understanding of the complex mechanisms related to TBI recovery.

The first demonstrations of OCT angiography for monitoring TBI recovery were conducted by Yali et al. (Jia et al. 2009) and Cetas et al. in 2009 (Cetas et al. 2009). Yali et al. demonstrated that OCT angiography can be used to capture the capillary response to a TBI in the cortex of a mouse model for a period of 10 days with the cranium left intact. In this study, TBI was induced by puncturing a hole with a 1.5mm depth into cortex through the skull.

Moreover, same group used OCT angiography to study the therapeutic effect of soluble epoxide hydrolase (sEH) gene deletion in revascularization after TBI (Jia et al. 2011a). The results showed that the restoration of blood volume at the lesion site was more pronounced in sEH knockout mice than in wild-type mice. These OCT angiography measurements were also confirmed by histology.

Subarachnoid space plays critical roles in both the regulation of intracranial pressure and maintenance of the brain's extracellular environment (Johanson et al. 2008). Blood leakage into that space, mostly triggered by TBI, is called subarachnoid hemorrhage (SAH) and it can cause serious complications (van Gijn et al. 2007). Unfortunately, these complications remain poorly

understood. The first study of SAH using OCT angiography focused on the role of the rostral ventromedial medulla (RVM) in modulating cerebral perfusion at rest and following an experimental SAH in rats (Cetas et al. 2009). Changes in CBF were measured using laser Doppler flowmetry and OCT angiography. RVM was activated or inactivated using a GABAA receptor agonist or antagonist. The results showed that RVM contributes to restoration of cerebral perfusion following a SAH. Failure in RVM could lead to acute perfusion deficits seen in patients following SAH.

Blood clots within the subarachnoid space impair cerebrospinal fluid (CSF) flow, which contributes to the increased intracranial pressure (ICP) and impaired cortical perfusion during the early phase (24 h) after SAH. Siler et al. showed that intracisternal administration of tPA immediately after SAH lowered ICP, increased CBV, and partially restored CSF flow at 24 h after SAH (Siler et al. 2014). Lowering ICP without tPA, by draining CSF, improved CBV at 1 h, but not 24 h after SAH. These findings suggest that blockade of CSF flow by microthrombi contributes to the early decline in cortical perfusion in an ICP-dependent and ICP-independent manner. Intracisternal tPA administration immediately after SAH partially restores CSF flow, reduces ICP, and improves cortical perfusion.

4.2 COMPARISON OF CRANIAL WINDOW IMPLEMENTATIONS FOR OMAG

4.2.1 *Background and Motivation*

In vivo imaging of brain microstructure and microcirculation has been a valuable approach to understand vascular function under normal and pathologic conditions. Within the complex vascular network, the pial vessels are intracranial vessels on the surface of the brain within leptomeninges layer of the cortex, which give rise to smaller penetrating arterioles that supply blood to the corresponding region of cerebral cortex (Jones 1970). The pial vessels form an effective collateral network, which comprises distal anastomoses from branches of anterior, middle, and posterior cerebral pial arteries (Cipolla 2009). Such network is responsible for the redistribution of flow when there is a constriction or an occlusion at one of the arteries/arterioles, which serves as a vital element in rescuing an ischemic region (Liebeskind 2003). In experimental stroke research, the examination of pial vessels on the brain cortex during acute injury and chronic recovery provides critical information for studying the mechanisms underlying ischemic stroke (Hossmann 2006).

Tissue scattering is one of the greatest obstacles faced by all optical imaging modalities (Wang 2002). The resolution, imaging depths and image quality are strongly affected by the light absorption and high scattering at cranial tissue during brain imaging. Therefore, two distinct types of cranial window techniques are developed to overcome these problems: the traditional cranial window, also known as open-skull window technique, in which part of the skull is removed and replaced with a glass coverslip (Holtmaat et al. 2009, 2012; Stetter et al. 2013), and the thinned-skull technique, in which a selected area of the skull is thinned down to a thickness of ~15-50 um (Drew et al. 2010; Szu et al. 2012). Although both methods have shown their ability to visualize structural and functional change in brain tissue, the invasive nature of open-skull window

technique is more likely to create changes in basal conditions in the cerebral blood flow (CBF), which makes it difficult to interpret experimental data.

There has not been any established preference in literature between thinned-skull and open-skull cranial window techniques for mouse CBF imaging. In this work, using OMAG and DOMAG imaging modalities, we compare these two cranial window techniques concerning surgical invasiveness and efficiency, as well as their ability to reveal pial microvasculature on mouse brain. Moreover, we improve thinned-skull techniques by combining protocols with thinning procedure (Szu et al. 2012) and polishing procedure (Drew et al. 2010) together, a large imaging window with a smoother surface is created to greatly reduce the cranial tissue scattering. As a result, thinned-skull cranial window achieves higher resolution of pial vessels compare to intact skull case, and have advantages over the open-skull cranial window in the efficiency of the surgical procedure and the available imaging area. More importantly, thinned-skull technique is found to apply minimal changes to the basal condition in the cerebral blood flows, and therefore, is recommended in studying hemodynamics in pial vessels during stroke studies.

4.2.2 *System and Methods*

4.2.2.1 Animal Model

Total 5 mice are used in the study. Three-month-old C57/BL6 mice weighing 23-25 g are obtained from Charles River Laboratories. The mouse is deeply anesthetized using 1.5-2% isoflurane (0.2 L/min O2, 0.8 L/min air) through a nose cone and placed on a stereotaxic frame and supported by a heating pad to maintain body temperature during the entire experiment process. After the disappearance of the toe pinching response, the skin and periosteum is removed to expose the skull, and a microscopic image is taken (Figure 4.1a). The skull is then subjected to a baseline imaging by OMAG (see Section 4.2.2.4). Drops of saline are applied to the skull constantly to keep wet

during imaging process. After the OMAG baseline is taken, the two types of cranial window procedures are performed on each side of parietal bone (see Section 4.2.2.2). Brain cortex transparency produced by application of cranial windows is demonstrated under microscope (Fig. 4.1b), and the two cranial windows are imaged by OMAG with the same imaging protocol used for the baseline imaging (see Section 4.2.2.4).

4.2.2.2 Cranial Window Techniques

Before starting cranial window procedures, dexamethasone sodium phosphate (0.02 ml at 4 mg/ml; ~ 2ug/g dexamethasone) is administered by subcutaneous injection to prevent cerebral edema. The skull surface is cleaned and dried with sterile saline and cotton swaps. Then, a drop of 1% Xylocaine (Lidocaine 1% + epinephrine 1:100,000 solution) is applied directly onto the skull to minimize the bleeding of the skull.

In preparation of the thinned-skull window, a selected area (4x4 mm) on the left parietal bone ~1.5 posterior and lateral to bregma is thinned down to 20~30 μm. The skull is thinned by a high-speed surgical hand drill (Foredom Electric Co., Ethel, CT, USA) with a round carbide bur (0.75 mm) followed by a green stone bur (Shofu Dental Corp., San Marcos, CA, USA). The skull is constantly wetted with sterile saline to remove the bone dust and to prevent overheating. When the thickness of the skull reaches ~ 30 μm with the pial vessels clearly visible through wetted bone, a polishing step is followed. The skull is sequentially polished with size 3F grit followed by size 4F grit (Convington Engineering, Redlands, CA, USA). A slurry of grid and saline was agitated with a custom made silicone coated drill bit. The polished skull is finally washed with sterile saline and the remaining bone dust are picked up by saline-soaked gelfoam.

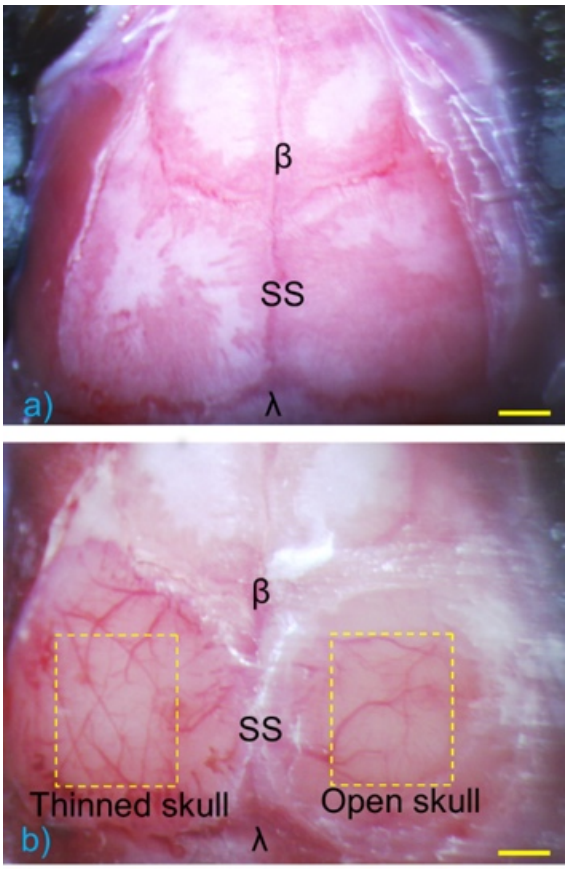

Figure 4.1. Microscopic images of skull before and after cranial windows comparison.

(a) Baseline of the skull where cranial windows are applied later, showing bregma lambda, and sagittal suture. (b) Left: Thinned- skull window with 464 mm available imaging area. Right: Open-skull cranial window with 363 mm available imaging area. The left cortex, thinned to 20 to 30 um, is comparably transparent under microscope compare to the right side of the cortex with open-skull window. Scale bar represents 1 mm. (Li et al. 2014)

For the open-skull cranial window, a circular piece of skull (~4x4 mm) at the region of interest ~1.5 posterior and lateral to bregma is removed and replaced with a round coverglass (Thermo Scientific, Waltham, MA, USA). To do so, a circular groove is first thinned with a shaft drill (Foredom Electric Co., Ethel, CT, USA). The groove is drilled slowly and saline is applied regularly to avoid heating. In the end, the central island of skull bone was lifted and removed with help of saline and replaced with a circular coverglass and sealed with cyanoacrylate glue, leaving the available imaging area with ~3x3 mm.

4.2.2.3 System Setup

A fiber-based SD-OCT system is used for the experiments (Tomlins and Wang 2005). A superluminescent diode (Thorlabs Inc., Newton, NJ, USA) is used as the light source, which has the central wavelength of 1340 nm and bandwidth of 110 nm that provided a ~7 μm axial resolution in the air (~5 μm in tissue if the refractive index of tissue is taken as 1.35). In the sample arm, 10X scan lens (Thorlabs Inc., Newton, NJ, USA) was used to achieve ~10 μm lateral resolution with 0.12 mm depth of view. The output light from the interferometer was routed to a home-built spectrometer, which had a designed spectral resolution of ~0.141 nm that provided a detectable depth range of ~3 mm on each side of the zero delay line. The line rate of the linescan camera (Goodrich Inc., Princeton, NJ, USA) was 92 kHz. The system had a measured dynamic range of 105 dB with the light power of 3.5 mW at sample surface. The operations for probe beam scanning, data acquisition, data storage and hand-shaking between them were controlled by a custom software package written in Labview.

4.2.2.4 Imaging Protocol

To visualize the volumetric microvasculature, OMAG scanning protocol was applied (An et al. 2010b). Briefly in this method, microvasculature down to capillary level is visiualized by separating structural tissue from dynamic scatters (e.g., moving red blood cells within patent vessels) using ED-based clutter filtering algorithm (Yousefi et al. 2011). In this protocol, each B-frame consists of 400 A-lines covering a distance of ~2.0 mm. The imaging rate was 180 fps. In the slow axis (C-scan), a total number of 2000 B-frames with 5 repetitions in each location were performed also covering a distance of ~2 mm. Hence the data cube of each 3D image was composed of 1024 by 400 by 400 (z-x-y) voxels, which took ~11 s to acquire.

After each OMAG scan, DOMAG measurement performed covering the same area to show the axial velocity map of CBF (Shi et al. 2013). Each B-scan in DOMAG protocol consisted of 10000 A-lines by acquiring 25 A-lines at each 400 discrete steps. In the elevational direction, there were 300 discrete points, i.e., 300 B scans. Three A-lines are skipped during Doppler processing to increase the time interval, T, between processed A-lines, and frame rate is set to 6 fps which gives an axial velocity range of ±6.1 mm/s. The data cube of each 3D image (C scan) was composed of 1024 by 400 by 300 (z-x-y) voxels, which took ~100 s to acquire with 6 fps imaging speed.

To acquire the CBF images over a large area of the cortex, the scan was repeated to create a mosaic image. This imaging protocol is firstly applied to intact skull case. After creating the cranial windows, same imaging protocol is repeated over the same area by keeping the discrepancies between those two cases minimum in terms of the focus of the probe beam and positioning and orientation of the sample.

4.2.3 *Results*

The volumetric OMAG MIP result of capillary network in the pial region of mouse brain is presented in Fig. 4.2, corresponding to the yellow dashed area in the microscopic image (Fig. 4.1b). Surface vessel dynamics play an important role in CBF regulation. Hence, the microcirculation at up to 200μm depth is targeted, which is arranged to cover the depth of focus of the lens. The final image, representing the CBF over the mouse cortex in the area of interest, is obtained by stitching and cropping 4 images together, for each side of the parietal bone. This procedure is applied both to baseline with intact skull (Fig. 4.2a-b) and to two cranial window cases (Fig. 4.2c-d) to compare the visible vessel density changes regarding to two different window opening methods.

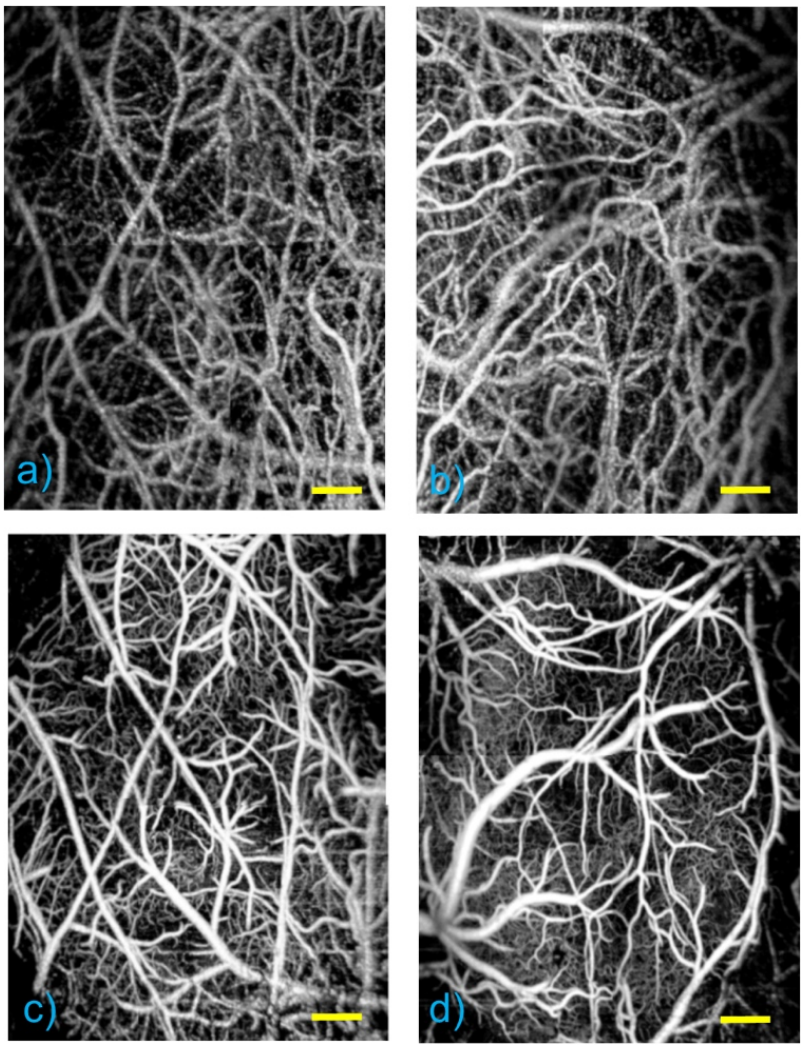

Figure 4.2. OMAG MIP view of microcirculation network up to 1 mm depth.

(a, b) With intact skull (baseline). (c) With thinned-skull cranial window. (d) With open-skull cranial window. Scale bar represents 0.4 mm. (Li et al. 2014)

To identify the location of the blood vessels and to determine the remaining thickness of the thinned-skull, OMAG images are merged with structural OCT images for both before and after cranial windows. Figure 4.3 presents maximum projection view of OMAG images of intact skull (Fig. 4.3a), thinned-skull (Fig. 4.3b) and open-skull cranial windows (Fig. 4.3c). Moreover, the cross sectional blood perfusion and structural images corresponding to the positions marked by the dash yellow lines are presented in Fig. 4.3(d-f) and Fig. 4.3(g-i), respectively. From the cross sectional structural images remaining thickness of the thinned-skull is estimated ~20-30 μm.

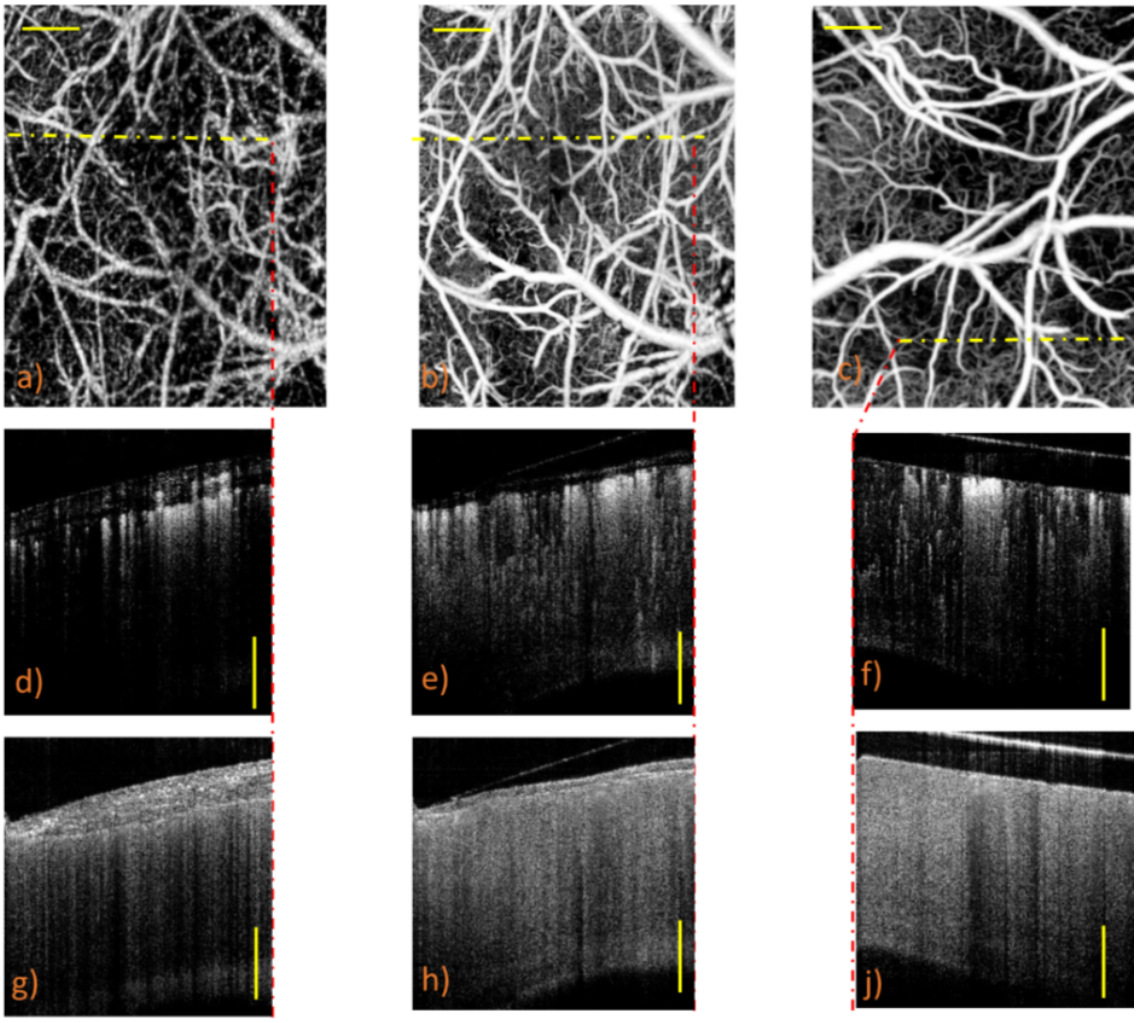

Figure 4.3. Cross-sectional and MIP views of OMAG images through cranial windows.

(a) Before thinned-skull (baseline). (b) After thinned-skull cranial window procedure. (c) After open-skull cranial window procedure. (d–f) The blood perfusion images of the cross-sections located at dotted yellow lines. (g–i) The structural images of the same cross-sections. Scale bar is 0.3 mm. (Li et al. 2014)

Furthermore, the same area is imaged using DOMAG protocol to obtain CBF axial velocity mapping. The bidirectional en face MIP images in Fig. 4.4 show the diving and rising vessels as green and red lines, respectively, where RBC axial velocity information is coded with a color bar in a range of ±6.1 mm/s. The diving arterioles and rising venules appear as green and red isolated spots. This is because their flow directions are mainly parallel to the beam axis, giving their axial velocity large enough to be detected at this range. However, the surface vessels connected to them,

whose flow nearly perpendicularly to the probe beam, escaped the detection due to their small axial velocity. Few out-of-range flows are also observed as phase-wrapped signals, seen as yellow color (combination of red and green).

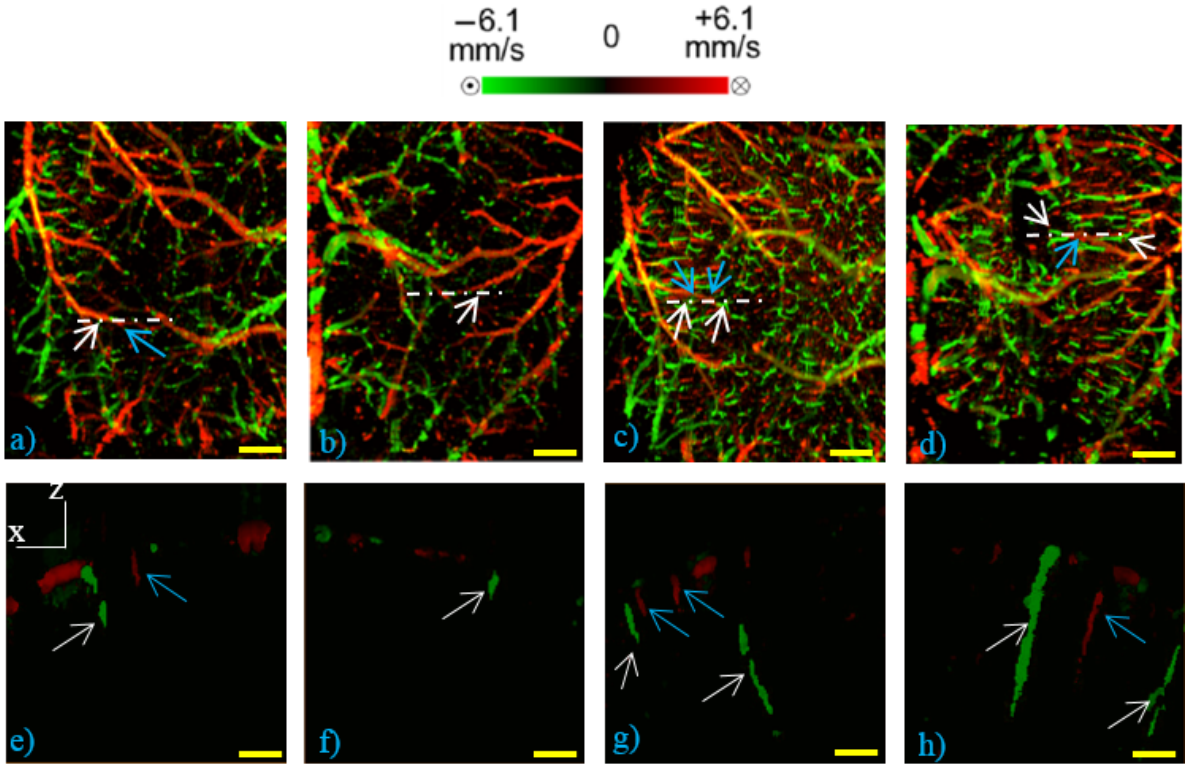

Figure 4.4. DOMAG MIP view of microcirculation network at 50–450 mm depth.

(a–b) Shows baseline before the application of cranial windows to intact skull. (c) With thinned-skull cranial window (d) With open- skull cranial window. The white dashed lines represent the location of the cross sectional views (along x–z planes) shown in (e–h). White arrows point the diving arterioles and blue arrows point the rising venules. Scale bar represents 0.5 mm in (a–d) and represent 0.15 mm in (e–h). (Li et al. 2014)

Figure 4.4 (a-b) demonstrate the CBF axial velocity mapping of intact-skull (baseline) case whereas Fig. 4.4(c-d) show the result of after applying two distinct cranial windows to each side of the mouse head. Moreover, cross sectional views of the areas corresponding to white dashed lines are shown in Fig. 4.4(e-f) for each case. For the intact-skull case, although the bigger vessels can be visualized, the diving arterioles or rising venules are harder to detect as seen in Fig. 4.4(e-f). On the other hand, Fig. 4.4(g-h) show that both type of cranial windows provide better

visualization of the diving arterioles and rising venules. Furthermore, similar to the OMAG case shown in Fig. 4.2-3, thinned-skull cranial window provides larger area with a better visibility.

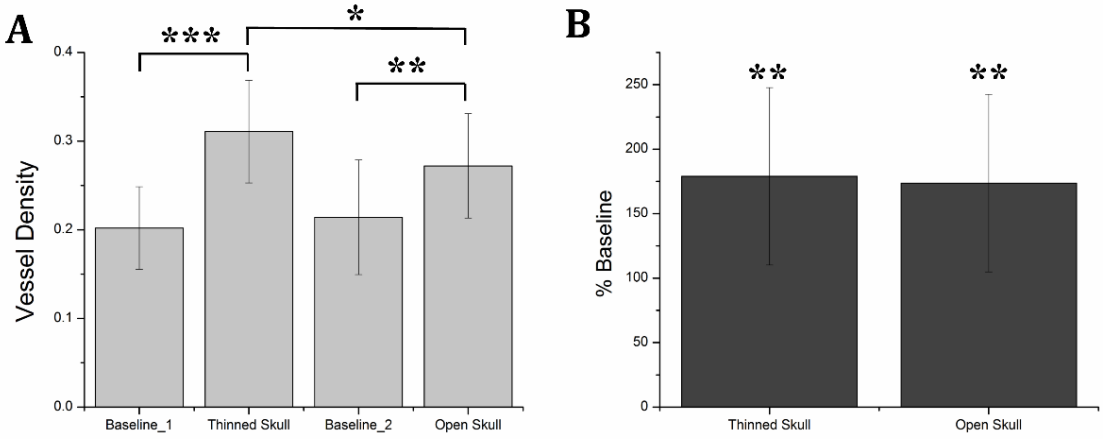

Figure 4.5. Vessel density comparison and total blood flow quantification.

(a) Comparison of detectable vessel density. Baseline_1 refers to basal condition before the thinned skull cranial window and baseline_2 refers to basal condition before the open skull cranial window. (b) Comparison of total blood flow among penetrating arterioles in thinned skull and open skull with respect to intact skull case. There is no significant differences between thinned- skull case and open-skull case. Data represent mean ± s.e.m. ***P, 0.01, **P, 0.05, and *P, 0.3 significantly different data sets (paired t-test). (Li et al. 2014)

In order to quantify the change in the quality of the blood perfusion image, the vessel densities of images from identical areas for each case is calculated using segmentation algorithm. Briefly in this method, firstly the identical areas are selected from the whole images and registered using the function, imregister, available in MATLAB®. Then, registered images are segmented for the blood vessels by creating a binary black and white image with an adaptive threshold technique specifically designed for OMAG blood flow images (Reif et al. 2012). Briefly in this method, first, a low-pass filter is used to minimize the elements that are smaller than a specific radius size. Then, a global threshold is used to set to zero all the pixels below a certain threshold. Finally, a local adaptive threshold is implemented to binarize the image based on the mean pixel value within a

predefined window size. The vessel density is calculated by dividing the number of ones with the total pixel number. Figure 4.5 shows the mean visible vessel densities of 5 samples for each case. The results indicate that mean values of visible vessel densities of baselines (intact-skull) are similar for both left and right sides of mouse brain. Moreover, thinned-skull provides 60% more details compare to baseline case and %15 more details than the open-skull case, in average.

4.2.4 *Discussion and Conclusion*

In our experiments, we demonstrated the feasibility of OMAG imaging through a thinned-skull window in a mouse model in vivo, and showed that the thinned-skull technique achieves same imaging quality as the open-skull cranial window for pial blood flow imaging, and has significant advantages over the open-skull cranial window regarding to surgical procedure and invasiveness to the animal. From our results, the skull is thinned to approximately 20-30 μm and the penetration depth is obtained at approximately 1 mm with image resolution of 7 μm and 10 μm in the axial and lateral direction, respectively. In the signal intensity profile, OMAG imaging through a thinned-skull window increases the signal intensity and depth penetration as compared to normal skull (Figure 4.3). Even though both a thinned-skull and an open-skull window can reach imaging depths of ~1 mm below pial surface in OMAG imaging, the available imaging area differs in two cranial windows, which could be crucial when accessing one or more anastomosis connections between major cerebral arteries during a stroke process. In our experience, an open-skull cranial window tends to accumulate more dirt around the window edge due to the dental cement, which further deteriorates the available imaging area and image quality. As a result, a thinned-skull technique creates a larger imaging window in a measure of ~4x4 mm compare to an open-skull window available imaging size of ~3x3 mm. Overall, OMAG imaging with thinned-skull window is proved to be a promising modality, permitting a great depth penetration for pial vessel

visualization, while providing a larger available imaging area when compared to an open-skull cranial window.

We further compare the invasiveness of these two window opening techniques by assessing the effects on vascular density within the imaging window. Our data has shown that in average, the thinned-skull method greatly reduces the invasiveness of the surgical procedure and preserves 15% more details in pial vessel imaging than open-skull. One of the reasonable explanation of loss of vessel in the open-skull case is that while employing a craniotomy on the skull, we encounter some bleeding owing to tearing of the vascular plexus in the trabecular section of the cranial bone. Under ideal circumstances the dura should not bleed. However, in our own experience, as the dura is attached to the inner table of the cranium, some superficial capillaries might tear during the removal of the cranial bone and small focal bleeding occur occasionally. Hence, the imaging quality and detailed vasculature network in the open-skull window is deteriorated.

Another advantage of the thinned-skull over the open-skull method is the surgical efficiency. From our experience, thinned-skull method consumes less surgical time (15 min) compared to the open-skull cranial window method (30 min). Since the thinned-skull method does not require a craniotomy, there is less complications to deal with during the surgery, such as excessive bleeding or swollen of the dura mater, which may result in the loss of capillaries when imaged by OMAG. The thinned-skull cranial window technique takes less effort to master the surgery procedure and create a higher successful rate overall.

Nevertheless, there are limitations when using the thinned-skull technique for brain vessel imaging. Since the remaining thinned skull lacks vasculature, it starts to become opaque within hours after surgery. Thinning, therefore, needs to be repeated before every imaging session for long-term observation, and the result can vary in imaging quality between sessions. For short term

imaging, a plastic food wrap can be placed on the wetted window surface to preserve best clarity of the thinned skull. For chronic study, a variation of the thinned-skull technique, reinforced thinned skull, needs to be applied for long term imaging purpose (Drew et al. 2010). Moreover, sub-dural hemorrhage can occur sometimes due to vibrations of drilling and interfere with OCT imaging. In such cases, a new animal model should be obtained for best experimental turnout.

We made the effort to keep all the crucial parameters, such as the focus of the probe beam and positioning and orientation of the target to be the same among different samples. The image registration steps performed in the post-processing are crucial to have a reliable quantitative comparison between the images of the same area for various cases. Although this study is carried out using OMAG technique, it is reasonable to believe that the results apply to all other OCT-based blood flow imaging modalities.

In summary, we evaluated the thinned-skull and open-skull cranial window techniques for CBF imaging using OMAG. We applied both techniques on the skull of the same animals and compared the procedure time, the risk to cause surgical complications, and their ability to reveal the pial microvasculature on mouse brain. The results proved that an improved thinned-skull cranial window has advantages in visualizing functional microvasculature within cerebral tissue using OMAG with better time efficiency and less damage to the cerebral tissues. Utilizing OMAG through thinned-skull cranial window can be helpful in tracking structural and flow changes in the cerebral cortex during stroke studies.

4.3 VASODYNAMICS OF CEREBRAL ARTERIOLES AFTER STROKE

4.3.1 *Background and Motivation*

The change in blood perfusion in highly interconnected pial arterioles is strongly related to the neural activities in the cerebral cortex (McCaslin et al. 2011), thus the ability to measure this change can provide important insights about the vascular reaction in the case of an ischemia (Schaffer et al. 2006). Pial arterioles are responsive to a disruption of blood flow (Shih et al. 2009) in various ways depending on their sizes and their spatial locations with respect to anastomoses. Penetrating arterioles are other important components of blood flow regulation, as they play an essential role in delivering blood from a highly collateralized pial arteriole network to capillaries in cerebral cortex. The blood flow regulation in penetrating arterioles is crucial for the subsequent survival of tissue within penumbra region. Interestingly, penetrating arterioles are not interconnected. Hence, in the case of a disruption of blood flow such as in stroke, the source of blood to the vital pathways to the penumbra is regulated by pial arterioles (Shih et al. 2009). Failure in supplying penetrating arterioles can cause a direct change in downstream capillaries and lead to a region of neuronal death (Shih et al. 2012).

Within the highly collateralized pial arteriole network, the major cerebral arteries, such as middle cerebral artery (MCA) and anterior cerebral artery (ACA), are interconnected by arteriolo-arteriolar anastomoses (AAAs), with penetrating arterioles attaching to them as T-junctions (Toriumi et al. 2009). The combined blood flow from MCA and ACA sources descends into the cortex after passing through T-junctions on the surface. However, little is known about AAA's role in the hemodynamic compensation through penetrating arterioles. Thus, evaluating the vessel diameter, the red blood cell (RBC) velocity and total flow changes in a significant number of pial

and penetrating arterioles in relation to the AAAs can provide a valuable insight about the active hemodynamic regulation during focal stroke.

Two-photon excited fluorescence microscopy (2PM) has been a well-accepted tool for quantifying RBC flow dynamics in single vessels in cerebral microvasculature. It has been widely applied for investigating neuronal connectivity (Denk et al. 1994), as well as blood flow activity by labeling RBCs (Schaffer et al. 2006). However, it has several limitations. It provides a small field of view and only measures the RBC velocity in vessels that are oriented parallel to the imaging plane. Additionally, the measurements need to be made one vessel at a time, which is time consuming. As a result, it is difficult to acquire large data sets during the time-constrained experiments, such as in the investigation of middle cerebral artery occlusion (MCAO) models in rodents.

In this work, we apply OMAG technique to evaluate the vessel diameter, the RBC axial velocity and total blood flow changes in a large number of pial and penetrating arterioles across the penumbra region in the parietal cortex before, during and after the MCAO. We focus on analyzing vasodynamics at different spatial locations with respect to the AAA territory between the MCA and ACA distal branches. The open-skull cranial window is applied to the region of interest (ROI) to achieve high quality images up to 500μm depth within 3x3 mm area (Li et al. 2014). OMAG images are taken during 60 minutes of the MCAO and the reperfusion periods and compared with the basal conditions. The following questions are being investigated: How does the AAAs re-distribute blood in response to MCAO, and how is it related to the changes in the pial and the penetrating arterioles? Our system and methods provide significant advantages to investigate these important questions. Thanks to the highly sensitive OMAG, we are able to resolve pial microvasculature up to capillary level, and provide the clear images of penetrating arterioles

up to 500μm depth. In contrast to 2PM, our techniques make it possible to image a larger number of vessels in a short time period during time-constrained MCAO experiment, thus providing the ability to compare various regions within the penumbra.

4.3.2 *System and Methods*

4.3.2.1 Animal Model

All experimental animal procedures performed in this study are approved by the Institute of Animal care and Use Committee (IACUC) of the University of Washington (Protocol number: 4262-01). Six male 12-week-old C57/BL6 mice weighing between 23 to 25 g were purchased from Charles River Laboratories (Seattle, WA, USA). The mice were deeply anesthetized using 1.5-2% isoflurane (0.2 L/min O2, 0.8 L/min air) during the experiments and euthanized at the end of the experiments. The body temperature of the animal was maintained at 36.8 C through homeothermic blanket system (507220-F, Harvard Apparatus, MA, USA). All the mice were subjected to three imaging sessions (baseline, MCA occlusion, and reperfusion) through a cranial window, covering the distal branches of MCA and ACA, as well as the AAAs. Surgical procedure is briefly described as follows: First, a standard 3x3 mm cranial window (Holtmaat et al. 2009) was created on the left parietal cortex 1 mm lateral from sagittal suture and 1 mm posterior from bregma by drilling a circular groove and lifting the central island. A circular cover-glass was placed over the exposed brain surface and sealed onto the bone with dental cement. Then, the cranial window was subjected to a baseline imaging by OMAG (see 4.3.2.3). After the baseline imaging was taken, the mouse was subjected to an MCAO using the Longa method (Longa et al. 1989), which involves an intraluminal filament insertion from isolated external carotid artery (ECA) and a temporary ligation of the ipsilateral common carotid artery (CCA). The occluding filament was slowly advanced through internal carotid artery (ICA) toward the cranial base until a mild resistance was

felt. A laser Doppler flowmeter microtip was placed perpendicular to the calvarium from superior nuchal line to the nasion as the guidance to a successful occlusion. Another set of OMAG images were taken at the same region under the window during the occlusion period of 60 minutes. For reperfusion, filament was removed so that MCA could be reperfused, and OMAG images were again acquired to represent the reperfusion. However, due to the time constraint of the experiment, we were unable to image reperfusion without untying the CCA. For this short time period to untie the CCA, we used the laser Doppler flowmetry to monitor. There was about 28% decrease in total flux with ligated CCA compared to the baseline, in average of 6 mice.

4.3.2.2 System Setup

A fiber-based SD-OCT system was used for the experiments (Reif et al. 2014). Briefly in this system, a superluminescent diode (Thorlabs Inc., Newton, NJ, USA) was used as the light source, which has a central wavelength of 1340 nm with a bandwidth of 110 nm, providing a ~7 μm axial resolution in the air. In the sample arm, 10X scan lens (Thorlabs Inc., Newton, NJ, USA) was used to achieve ~7 μm lateral resolution (full width half maximum of the point spread function) with 0.12 mm depth of field. The output light from the interferometer was routed to a home-built spectrometer, which had a designed spectral resolution of ~0.141 nm that provided a detectable depth range of ~3 mm on each side of the zero delay line. The line rate of the linescan camera (1024 pixel detector-array, Goodrich Inc., Princeton, NJ, USA) employed in the spectrometer was 92 kHz. The system had a measured dynamic range of 105 dB with the light power of 3.5 mW at the sample surface. The operations for probe beam scanning, data acquisition, data storage and hand-shaking between them are controlled by a custom software package written in Labview.

4.3.2.3 Imaging Protocol

To visualize the volumetric microvasculature, OMAG scanning protocol was applied to obtain detailed cerebral microvasculature and flow velocities in the arterioles. Briefly in this protocol, 400 A-lines covering a distance of ~1.5 mm constituted each B-frame (fast axis). In the slow axis (C-scan), there are 400 steps, also covering a distance of ~1.5 mm. At each step, 8 repeated B-frames are acquired. With this scanning protocol, the data cube of one complete 3D scan was composed of 1024 by 400 by 3200 (z-x-y) voxels, which took ~18 s to acquire with an imaging rate of 180 fps. To obtain microvasculature down to capillary level at the each step, an ED-based clutter filtering algorithm (Yousefi et al. 2011) was used to separate structural tissue from flowing RBCs from the 8-repeated B-frames. Hence the final 3D vascular image was composed of 1024 by 400 by 400 (z-x-y) voxels. The lumen diameters of vessels were calculated manually from OMAG images using a MATLAB graphical user interface. Accordingly, the full-width half maximum of the pixel intensities are located on the vessels and the diameters are calculated between these locations based on the ~2μm/pixel resolution.

After each OMAG scan, DOMAG scanning was performed covering the same area to show the axial velocity map of cerebral blood flow (CBF) (Shi et al. 2013). Each B-scan in DOMAG protocol consisted of 10000 A-lines by acquiring 25 A-lines at each 400 discrete steps. In the slow scan direction (C scan), there are 600 discrete steps, i.e., 600 B scans. The data cube of each processed 3D vascular image was composed of 1024 by 400 by 600 (z-x-y) voxels, which took ~100 s to acquire with 6 fps imaging speed. We integrated DOMAG images in en face plane (Srinivasan et al. 2013b) to calculate flow in penetrating arterioles.

To acquire the CBF images over a large area of the cortex, these imaging protocols are repeated to create a mosaic image. OMAG and DOMAG algorithms are first applied to the datasets

acquired at the basal condition. After applying MCAO to the mouse, the imaging protocol was repeated over the same area during occlusion and reperfusion by keeping the discrepancies minimum between the three imaging sessions in terms of the location of the focus of the probe beam and the positioning and orientation of the sample.

The data are presented as mean ± s.e.m among six animal experiments. The differences between the experimental means of basal, occlusion and reperfusion conditions are tested with a two-tailed paired t-test.

4.3.3 *Results*

4.3.3.1 Pial and Penetrating Arteriole Vasodynamics under Basal Conditions

Pial and penetrating arteriole vasodynamics in the mouse cortex are imaged through a cranial window ($9mm^2$) using the OMAG technique. The volumetric en face average intensity projection (AIP) of 3D OCT structural image is used here to better visualize and localize the diving and rising vessels. Because of the light absorption and the strong scattering effect from RBCs, the vessels parallel to the probing beam appear as darker spots in the en face AIP of structural image in contrast to other regions and the vessels that are approximately perpendicular to the probe beam. This phenomenon helps the detection of penetrating vessels easily, especially at the T-junctions that are mostly invisible in the en face maximum intensity projection (MIP) of OMAG images. Figure 4.6a shows the mosaic image of 9 en face AIP of 3D OCT structural images.

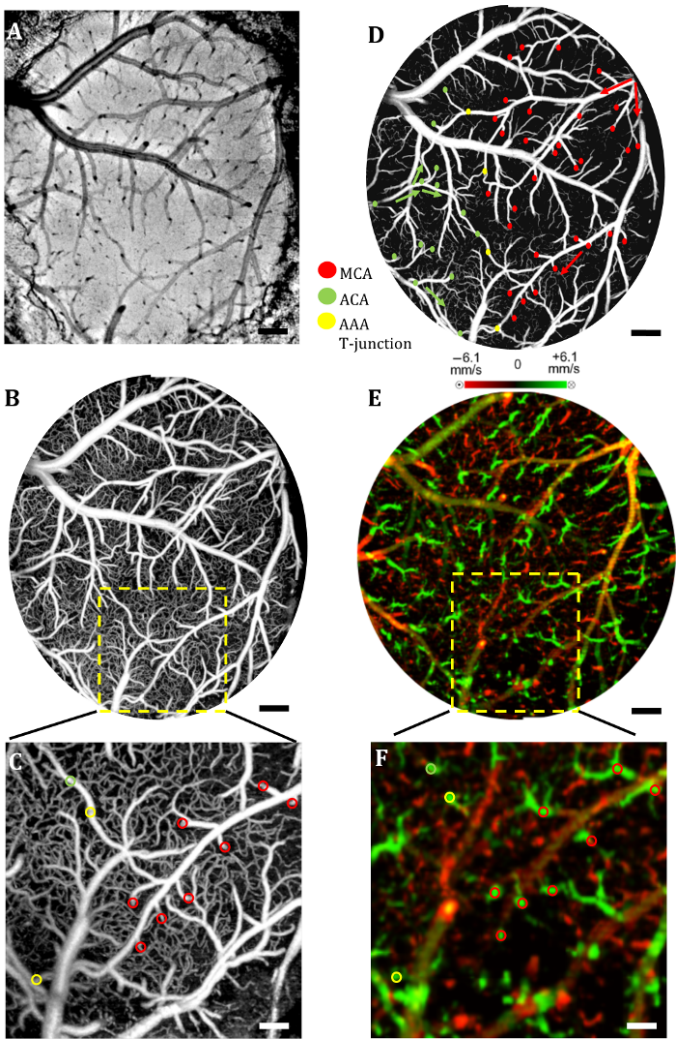

Figure 4.6. Pial and Penetrating Arteriole Vasodynamics under Basal Conditions.

(a) Pial and penetrating arteriole vasodynamics under basal conditions: (a) En face AIP of the cortical structure through the cranial window. (b) En face MIP of OMAG within 100μm in depth from the cortical surface. (c) Closer view of a region marked by a dashed yellow box in (b). (d) En face map to show penetrating arterioles in OMAG image. Red, green and yellow dots correspond to MCA, ACA and AAA T-junction sourced arterioles. (e) En face MIP of DOMAG that shows axial velocity distribution within 500μm depth from cortical surface. (f) Closer view of a region marked by a dashed yellow box in (d). In (c) and (f), penetrating arterioles are marked by circles. Scale bar represents 0.35 mm in (a,b,d,e) and 0.15 mm in (c,f). (Baran et al. 2015e)

The penetrating arterioles are located manually in the high contrast version of Fig. 4.6b and are shown in Fig 4.6d. In doing so, the en face AIP of OCT structural image (Fig. 4.6a) is used as a guide to detect the locations of the penetrating arterioles and then the DOMAG image (Fig. 4.6e) is employed to differentiate the MCA and the ACA branches from veins and to localize the AAA

T-junctions. In the particular case presented in Fig. 4.6, the penetrating arterioles that are identified as the MCA and the ACA branches are marked with red and green dots, respectively (Fig. 4.6d). Moreover, the AAA T-junctions are found in between the ACA and the MCA branches and are denoted with yellow dots in Fig 4.6d. The penetrating arterioles that have connections to ACA are chosen from the clear part of cranial window. We did not make selections based on speed or diameter. The corresponding arterioles are also pointed out in the ROI images with circles in Fig. 4.6(c, f). After random sampling (n=6 animals), average lumen diameter of 143 pial and 127 penetrating arterioles are calculated to be 40.7μm and 25.6μm, respectively.

4.3.3.2 Pial and Penetrating Arteriole Vasodynamics in Response to MCA Occlusion

Changes in the pial and penetrating arteriole vasodynamics in response to MCAO are studied using OMAG and DOMAG techniques. Fig. 4.7(b-c) show the blood flow changes in the penetrating arterioles during 60 min occlusion. When the MCA branches fails to support the penetrating arterioles, flow is reversed in the pial arterioles and the ACA branches take over some of the penetrating arterioles as shown in Fig. 4.7b. However, this collateral support fails in providing blood to some of the MCA connected penetrating arterioles which mainly reside in the weak AAA territory as pointed out in Fig. 4.7c. Moreover, in consistence with the previous literature (Shih et al. 2009), the blood flow in the penetrating arterioles are never reversed. On the other hand, T-junction locations may shift as in the case pointed out with a dashed circle in Fig. 4.7e. The average lumen diameter of the pial and the penetrating arterioles, corresponding to the baseline case, are decreased to 38.8μm and 24.2μm, respectively.

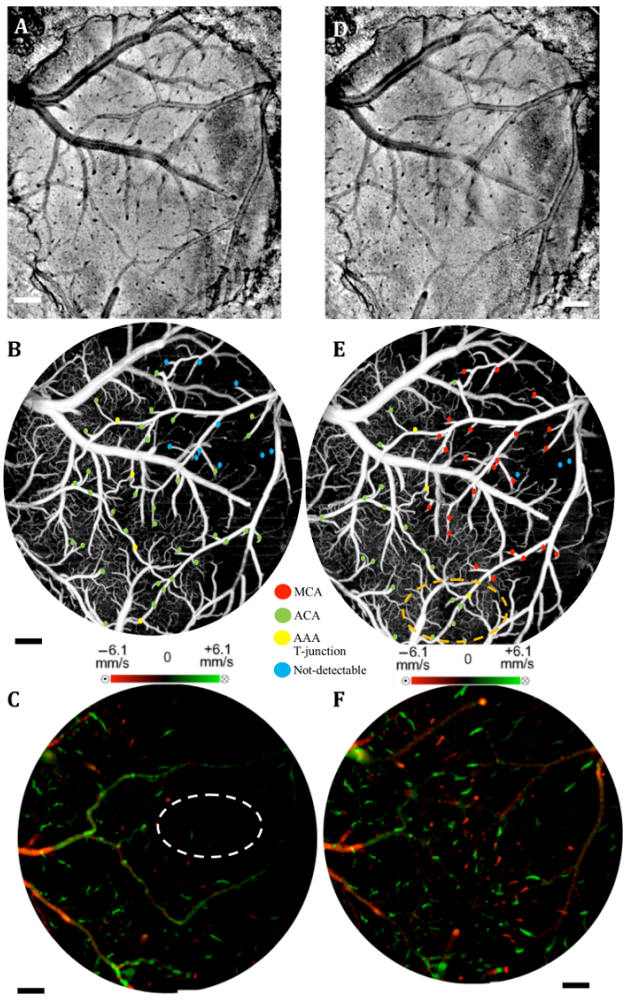

Figure 4.7. Pial and Penetrating Arteriole Vasodynamics during MCAO and reperfusion.

(a,d) En face AIP of the cortical structure through the cranial window during occlusion (a) and during reperfusion (d), respectively. (b,e) En face OMAG MIP of the microcirculation network within 100μm depth from the cortical surface during occlusion (b) and during reperfusion (e), respectively. Map of the diving arterioles on OMAG image are shown. Red, green and yellow dots correspond to MCA, ACA and AAA T-junction sourced arterioles. Yellow dots in (b) are showing the location of T-junctions in the baseline while they were supplied by MCA and ACA. Blue dots correspond to the diving arterioles that are at not-detectable level compared to basal condition. Dashed circle in (e) points out the shift in the location of T-junction point. (c,f) En face DOMAG MIP of velocity distribution within 500μm depth from cortical surface during occlusion (c) and during reperfusion (f), respectively. Dashed circle in (c) points out the area with failed collateral support. Scale bar represents 0.35 mm. (Baran et al. 2015e)

During the reperfusion, some of the AAAs stay active in supplying blood to four of the penetrating arterioles via ACA and three of the MCA connected penetrating arterioles remain inactive, as shown in Fig. 4.7e. On the other hand, the most of the capillaries distant from the AAA territory disappear during the occlusion and do not reappear after the reperfusion. The average

lumen diameters of the corresponding pial and penetrating arterioles return back to their baseline values with a slight increase, which are measured at 41.1 μm and 26.3μm, respectively. The comparison of the average lumen diameters among basal, occlusion and reperfusion conditions for the pial and the penetrating arterioles is shown in Fig. 4.10a.

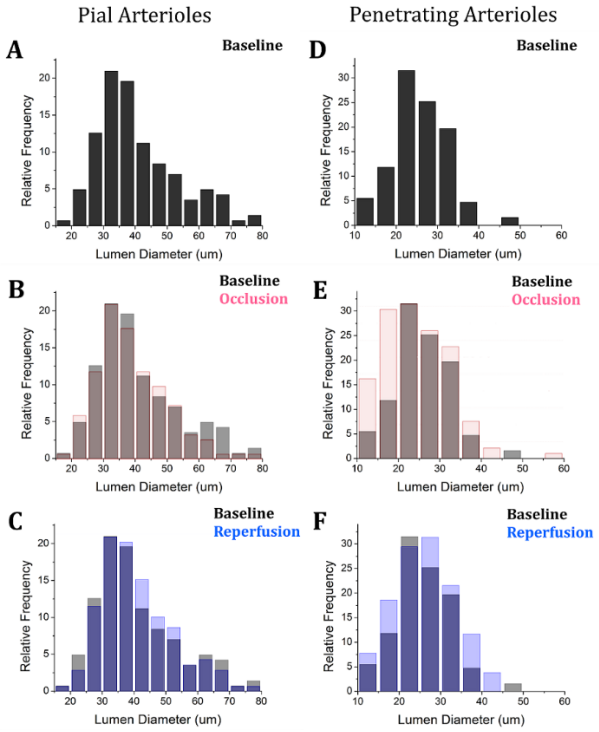

Figure 4.8. The lumen diameter changes in the pial arterioles during stroke.

(a) Basal condition, (b) basal and occlusion conditions (overlaid) and (c) basal and reperfusion conditions (overlaid); and the penetrating arterioles under (d) basal condition, (e) basal and occlusion conditions (overlaid) and (f) basal and reperfusion conditions (overlaid), respectively. (Baran et al. 2015e)

The MCAO model used in this study generates incomplete recovery during reperfusion due to the sustained blocking of CCA branch vessels. This can be observed in Fig. 4.10b, where the velocity and the flow changes in the penetrating arterioles during the occlusion and the reperfusion with respect to the baseline are compared. Relative larger decrease in the total blood flow compared to the mean RBC axial velocity can be explained by the disappearance of some of the penetrating arterioles during the occlusion and the reperfusion as shown in Fig 4.9. Moreover, the lumen diameter changes of the penetrating arterioles (shrink or dilate) occur in response to the

stroke whereas the lumen diameters of the pial arterioles are only slightly affected as demonstrated in Fig. 4.8.

4.3.3.3 Pial Arteriole Vasodynamics in relation to AAA formation

AAA's role in the response of the pial and the penetrating arterioles to MCAO is analyzed using both the OMAG and the DOMAG results. Two ROIs are selected in the DOMAG images for all cases where the presence of AAAs is either strong or weak (Fig 4.9a-c). These regions are also located in the OMAG images and corresponding penetrating arterioles are marked in Fig. 4.9d-f.

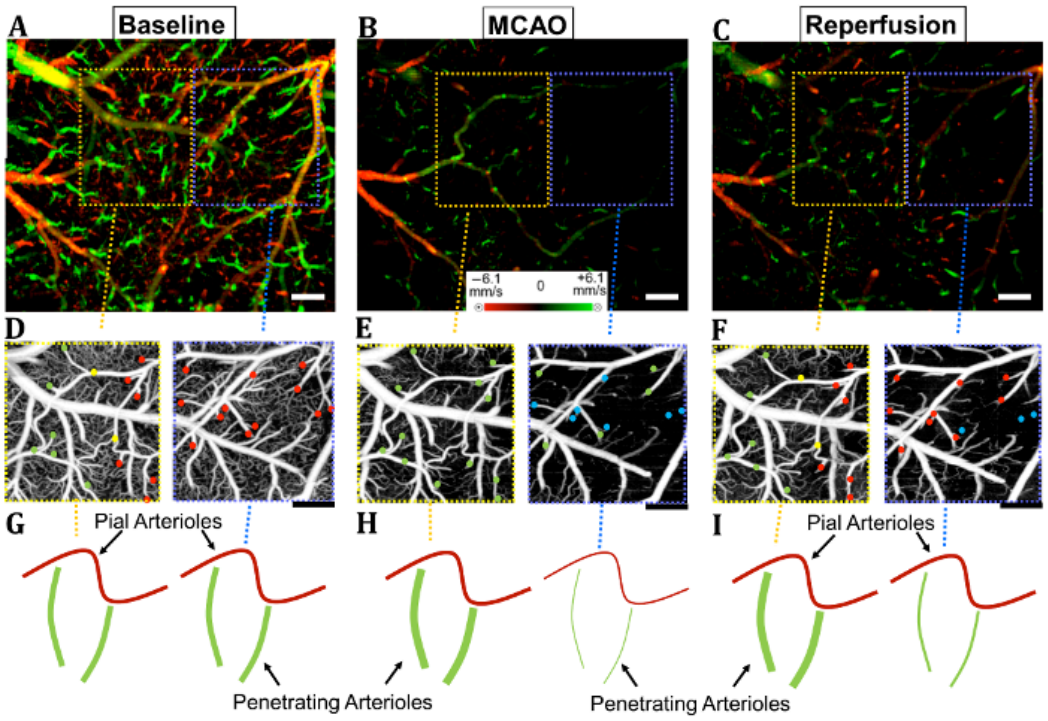

Figure 4.9. Comparison between regions where AAA is relatively stronger or weaker.

(a-c) DOMAG results for (a) basal (b) during MCAO and (c) after reperfusion conditions, respectively. Strong AAA area is marked with a yellow dashed box and weak AAA area with a blue dashed box. (d-f) OMAG comparison between strong and weak AAA ROIs for (d) basal, (e) during MCAO, and (f) after reperfusion conditions, respectively. (g-i) Red, green and yellow dots correspond to MCA, ACA and AAA T-junction sourced arterioles. Blue dots correspond to the diving arterioles that are at not-detectable level compared to basal condition. Cartoon representations of the lumen diameters of pial and penetrating arterioles for (g) basal, (h) during MCAO, and (i) after reperfusion conditions, respectively. Scale bar is 0.3 mm. (Baran et al. 2015e)

Then, the mean lumen diameter, the total blood flow and the RBC axial velocity in the penetrating arterioles and the pial arterioles within these regions are compared. Fig. 4.10b shows that the penetrating arterioles that are close to the strong AAA territories dilate whereas the pial arterioles do not, which is consistent with the previous finding (Shih et al. 2009). Although the dilation effect in the average lumen diameter is subtle, it is statistically significant. On the other hand, the penetrating arterioles constrict significantly in the weaker AAA territories as shown in Fig. 4.10c. Moreover, the total blood flow and the RBC mean axial velocity in the penetrating arterioles close to a weak AAA suffered from a significantly larger drop compared to the ones close to a strong AAA (Fig. 4.10e-f).

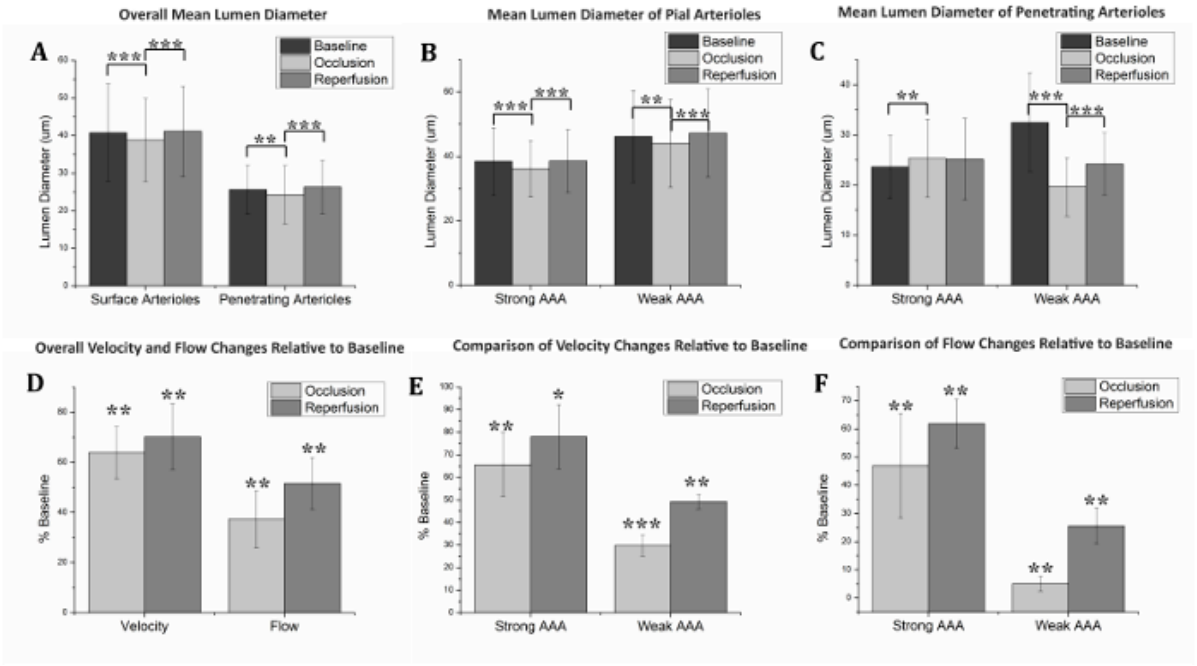

Figure 4.10. Lumen diameter, RBC velocity and total blood flow comparison.

(a) The mean lumen diameters of 143 pial and 127 penetrating arterioles for basal, occlusion and reperfusion cases (n=6 animals). (b, c) Comparison of mean lumen diameters of pial and penetrating arterioles, respectively, between strong and weak AAA areas. ***P<10-3 and **P<0.05 significantly different data sets (paired t-test). (d) The mean total blood flow and RBC velocity changes compared to baseline among 127 penetrating arterioles during occlusion and reperfusion (n=6). (d, e) Comparison of velocity and flow changes, respectively, in penetrating arterioles, between strong and weak AAA areas. ***P<10-3 and **P<0.05 significantly different data sets from baseline (paired t-test). (Baran et al. 2015e)

4.3.4 *Discussion and Conclusion*

Stroke is a major disease that has been heavily researched on. The severity and the duration of ischemia are the two major biomarkers for the assessment of ischemic damage during stroke. The impairment of physiological properties of neurons caused by an ischemia can be reversible depending on the severity of the ischemia and the time duration without proper reperfusion. The tissue surrounding the infarct core with a salvageable status is called penumbra. The penumbra dies as the infarct core expands over time.

To reveal the role of cerebral pial arteriole network in the local hemodynamic homeostasis during ischemia, we evaluated diameter and flow fluctuations in total 143 pial and 127 penetrating arterioles overlaying the stroke penumbra from six animals during MCAO. Three main findings are highlighted: (1) The flow reversals occur in the pial arterioles through anastomosis, and ACA takes over blood supply to the penetrating arterioles attaching to MCA side. (2) The penetrating arterioles near strong AAA territory dilate, and sufficiently restore the flow to the ischemic region. (3) The flow compensation decreases with the increase of the distance away from the AAA territory, resulting in poorly recovered penetrating arterioles residing away from the AAA connections during reperfusion.

Pial and penetrating arterioles respond differently to an occlusion, and they act together to compensate blood flow to an ischemic region. Reversible blood flow in the pial arterioles occurs according to a pressure gradient. When the brain is subjected to an ischemic event by MCAO, the flow balance in AAAs is immediately disrupted and the retrograde blood flow appears in MCA, as found by (Toriumi et al. 2009). However, no dilation events are observed among the pial arterioles in the experiment. In contrast, the penetrating arterioles can actively dilate to deliver blood to the ischemic region, but no reversal flow occurs in the penetrating arterioles, which is

consistent with the previous finding by (Shih et al. 2009). In addition, an interesting fact found in our study is that the distribution of the arteriole dilations is not homogenous across the ROI. The penetrating arterioles close to a strong AAA connection dilate despite of the overall decrease in mean lumen diameter. In other words, the penetrating arterioles constrict significantly in the areas further away from AAAs. To summarize, in order to have active dilations of the penetrating arterioles during severe ischemia, the pial arterioles must be kept flowing due to the regulation of AAAs. Moreover, the lack of blood supply on the pial arterioles also affects the recovery of the penetrating arterioles during reperfusion. Our data reports a higher restoration of RBC velocity in the penetrating arterioles near a strong AAA territory in comparison with a weak one, which is critical for the survival of the tissue during stroke recovery.

Besides the CBF images, the en face AIP of 3D OCT structural images from 60 min of occlusion and reperfusion (Figure 4.7(a,d)) also lead to an interesting observation: regions in the areas far from the AAA territory appear darker compared to the uniform looking baseline. The increased light scattering due to the changes in cell morphology in the infract region (Kawauchi et al. 2011) is suspected to be responsible for the non-uniform intensity distribution in the cortex after stroke. This phenomenon was also observed by mapping light attenuation coefficients and correlated with histology in a similar MCAO model (Srinivasan et al. 2013b).

Label-free OMAG technique offers a unique ability to quickly image a relatively large area in time-sensitive stroke experiments. However, it comes with some limitations. Firstly, the lateral resolution of our system is ~7 μm with a depth of focus of 0.12 mm. This makes the diameter measurement inaccurate for the pial vessels, especially for those smaller than 20 μm. Secondly, since only the axial velocity is measured, it is difficult, if not impossible, to detect the RBC velocities and flow in the pial vessels perpendicular to the optical axis, due to their very small axial

velocities, hence a slightly tilted stage is needed to solve this problem. Moreover, the absolute flow information is hard to derive accurately, due to the resolution and the light intensity deterioration with depth. Hence, this technique is best suited for comparison studies where errors in the measurements do not affect the differential conclusions. In this study, we tried our best to keep all the crucial parameters, such as the focus of the probe beam and positioning and orientation of the sample to be the same among all the imaging sessions. To check if there is a systematic error in the determination of total blood flow in penetrating arterioles, the total blood flow conservation rule is applied. The average velocity and flow in the 127 pairs of penetrating arterioles and rising venules are similar within %10 margin.

In summary, our methods enable us to discover AAA's role in the collateral blood perfusion dynamics in the mouse cerebral cortex after focal stroke. Thanks to the high sensitivity and the large field of view provided by OMAG, we compare regions in cerebral cortex, either closer to or further away from AAA territory during MCAO. The conclusions suggest that AAA plays a major role in active regulation of the pial and penetrating arterioles during stroke, providing blood flow to actively dilate the penetrating arterioles in order to rescue the tissue in the penumbra region.

Chapter 5. SUMMARY AND FUTURE WORK

In this dissertation, the emerging applications of functional OCT in dermatology and neuroscience are studied. In addition, new methods are proposed for label-free visualization of tissue injury and lymphatic network *in vivo* using OCT. After an introduction to OCT technology and OCT-based microangiography methods in Chapter 1, new functional OCT methods are detailed in Chapter 2. Then, the capabilities and potential of functional OCT in clinical dermatology is demonstrated in Chapter 3. Finally, Chapter 4 provides overview of the current developments of OCT for neuroscience applications.

Emerging digital imaging methods take place of classical "cold light" examination by providing the superior ability of visualizing, monitoring, quantifying, and classifying morphologic changes during various cutaneous processes. However, most of these methods are used only in characterizing structural changes in tissue beds and are difficult to provide blood perfusion maps at a capillary level. OCT-based microangiography provides additional information about the extent of injury by providing a high resolution map of functional microvasculature. Utilizing OMAG features along with OCT structural images promises a better strategy for assessing the condition of abnormal skin condition than just relying on structural images.

Despite of its presented advantages, OCT has not been widely adopted in clinical dermatology yet. The reasons may be summarized as the difficulty of articulating functional properties of OCT on human subjects and its relatively high cost compared to simple and well-established techniques used in dermatology. Recent developments of high-speed reliable swept laser sources and novel OCT angiography methods such as OMAG would make the OCT system more user friendly with lower cost, attractive to clinicians.

On the other hand, an accurate visualization and quantification of the microvascular networks in the cerebral cortex are critical for evaluating therapies that are aimed to treat neurovascular diseases, such as stroke, traumatic brain injury, vascular dementia, inflammation, and cancer. Intensity or complex signal based OMAG methods are superior to Doppler methods for in vivo visualization of microvasculature at capillary level in cortex. However, the OCT angiography signal is nonlinearly depended on the blood flow rate, and hence it is difficult to quantify blood perfusion by only looking at OCT angiography images. Moreover, RBC flux measurement in capillaries is still a challenging task using currently available methods. New methods applicable to OCT systems with improved development of both hardware and algorithm are in need. Combined OCT flux maps with OCT angiography images, including velocity measurement using Doppler approach, would provide critical information for a comprehensive understanding of microvascular dynamics in brain.

Although OCT technology has made great progress over the last decade, there are still some caveats. Firstly, the lateral resolution of typical systems is ~10 μm with a depth of focus of ~0.15 mm. This makes the diameter measurements inaccurate for those vessels smaller than 20 μm. This problem may be mitigated by a cost effective higher resolution system with sufficient depth of focus to cover entire cortical layer. In addition, cranial window techniques can be implemented to increase the penetration depth and the quality of the OCT angiograms. An alternative solution would be to combine OCT with other imaging tools that can provide higher resolution, such as confocal microscopy and two-photon microscopy. The combination of OCT with these techniques may provide additional information that is useful to investigate the vascular involvement in neurological diseases. One limitation of using other techniques would be the administration of

exogenous contrast agents that requires additional safety screening and can produce cytotoxic by-products.

Secondly, Doppler methods can only measure axial velocity and typically fail to detect the RBC velocities and the flow in the pial vessels perpendicular to the optical axis, due to their very small axial velocities. The absolute flow information is difficult to derive accurately, due to the resolution and the light intensity deterioration along the depth. Hence, current OCT angiography is best suited for comparative studies where errors in the measurements do not affect the differential conclusions.

Furthermore, the motion induced noise can deteriorate the quality of OCT angiograms significantly. Motion tracking systems should be employed for awake animal experiments. In addition, ~1.5 mm penetration depth of OCT limits its applications to cortex, typically with a cranial window. Luckily, the development of catheter probes using MEMS scanners are surging and it can extend the use of OCT in deeper layers of brain.

Recent advancements in swept-source lasers pushed the OCT speed into ~MHz line rate era, and volumetric OCT microstructure and microvascular imaging at video rate has been demonstrated. At these high speeds, resonant scanners have to be utilized instead of non-resonant galvo scanners to scan the probe beam. Moreover, the sensitivity of system drops with the increase of system speed since the number of photons available for each A-line decrease with the increase of imaging speed. These lead to new challenges for achieving high quality 4D OCT angiograms. However, 4D OCT angiograms with high resolution capabilities would be a great help for understanding the ecosystem of rapidly changing brain.

OCT is a surging imaging modality that has applications for several clinical and basic research investigations and has been witnessed as a revolutionary tool in clinical ophthalmology. In this

dissertation, the main focus is to explore OCT's imaging capabilities of highly complicated functional dynamics in mouse brain and in human skin to show its potential in neuroscience research and clinical dermatology. Here, functional OCT is defined as the extension of structural OCT where in vivo dynamics in non-static tissue components, such as blood vessels, are monitored using various methods: OCT angiography, OLAG and TIM. The main capability that OCT angiography offers for the understanding of the animal models of medical conditions and clinical management of these conditions is to differentiate and compare the healthy functioning microvasculature to ischemic or abnormal microvascular network by looking at various parameters such as total blood flow and vessel density within the region of interest. This way, angiogenesis and other vascular phenomenon can be monitored and studied in vivo, without the necessity of administration of contrast agents. Moreover, OLAG brings the unique ability of non-invasive visualization of lymphatic network within in vivo human skin. Although this first time achievement has a long way to go before becoming clinically viable, in the future, it could enable monitoring lymphatic dynamics that occur in several cancerous or inflammatory diseases with a truly non-invasive manner. Lastly, TIM can be used for accurate visualization of *in vivo* structural changes following an injury, which can be an important alternative non-invasive method in applications, such as stroke, where histology is the only way to determine the extent of the injury at the end of a longitudinal study. Overall, I believe that functional OCT will become an indispensable, yet cost effective tool to monitor changes in tissue morphology and hemodynamics for diagnosis of various diseases or for following pharmacological interventions.

BIBLIOGRAPHY

Abramovits W, Stevenson LC. Changing paradigms in dermatology: new ways to examine the skin using noninvasive imaging methods. Clin Dermatol 2003;21:353–8.

Akamatsu Y, Nishijima Y, Lee CC, Yang SY, Shi L, An L, et al. Impaired Leptomeningeal Collateral Flow Contributes to the Poor Outcome following Experimental Stroke in the Type 2 Diabetic Mice. J Neurosci 2015;35:3851–64.

An L, Qin J, Wang RK. Ultrahigh sensitive optical microangiography for in vivo imaging of microcirculations within human skin tissue beds. Opt Express Osa; 2010a;18:8220–8.

An L, Qin J, Wang RK. Ultrahigh sensitive optical microangiography for in vivo imaging of microcirculations within human skin tissue beds. Opt Express 2010b;18:8220–8.

An L, Shen TT, Wang RK. Using ultrahigh sensitive optical microangiography to achieve comprehensive depth resolved microvasculature mapping for human retina. J Biomed Opt 2011;16:106013.

Arumi-Uria M, McNutt NS, Finnerty B. Grading of Atypia in Nevi: Correlation with Melanoma Risk. Mod Pathol 2003;16:764–71.

Baran U, Choi WJ, Wang RK. Potential use of OCT-based microangiography in clinical dermatology. Ski Res Technol 2015a;:238–46.

Baran U, Li Y, Choi WJ, Kalkan G, Wang RK. High resolution imaging of acne lesion development and scarring in human facial skin using OCT-based microangiography. Lasers Surg Med 2015b;47:231–8.

Baran U, Li Y, Wang RK. In vivo tissue injury mapping using optical coherence tomography based methods. Appl Opt Optical Society of America; 2015c;54:6448.

Baran U, Li Y, Wang RK. In vivo tissue injury mapping using optical coherence tomography based methods. Appl Opt 2015d;54:6448.

Baran U, Li Y, Wang RK. Vasodynamics of pial and penetrating arterioles in relation to arteriolo-arteriolar anastomosis after focal stroke. Neurophotonics 2015e;2:025006.

Baran U, Qin W, Qi X, Kalkan G, Wang RK. OCT-based label-free in vivo lymphangiography within human skin and areola. Sci Rep 2016;6:21122.

Baran U, Wang RK. Review of optical coherence tomography based angiography in

neuroscience. Neurophotonics 2016;3:010902.

Barton J, Stromski S. Flow measurement without phase information in optical coherence tomography images. Opt Express 2005;13:5234–9.

Berger G, Laugier P, Thalabard JC, Perrin J. Global Breast Attenuation: Control Group and Benign Breast Diseases. Ultrason Imaging 1990;12:47–57.

Berny-Lang MA, Hurst S, Tucker EI, Pelc LA, Wang RK, Hurn PD, et al. Thrombin Mutant W215A/E217A Treatment Improves Neurological Outcome and Reduces Cerebral Infarct Size in a Mouse Model of Ischemic Stroke. Stroke 2011;42:1736–41.

Bollinger A, Amann-Vesti B. FLUORESCENCE MICROLYMPHOGRAPHY: DIAGNOSTIC POTENTIAL IN LYMPHEDEMA AND BASIS FOR THE MEASUREMENT OF LYMPHATIC PRESSURE AND FLOW VELOCITY. Lymphology 2013;40:52–62.

Bracewell RN. The Fourier Transform and Its Applications [Internet]. Vol. McGraw-Hil, McGrawHillNew Yorkpp 2000.

Braverman IM. The Cutaneous Microcirculation. J Investig Dermatology Symp Proc 2000;5:3–9.

Cetas JS, Lee DR, Alkayed NJ, Wang R, Iliff JJ, Heinricher MM. Brainstem control of cerebral blood flow and application to acute vasospasm following experimental subarachnoid hemorrhage. Neuroscience 2009;163:719–29.

Chen Z, Milner TE, Srinivas S, Wang X, Malekafzali a, van Gemert MJ, et al. Noninvasive imaging of in vivo blood flow velocity using optical Doppler tomography. Opt Lett 1997;22:1119–21.

Choi WJ, Reif R, Yousefi S, Wang RK. Improved microcirculation imaging of human skin *in vivo* using optical microangiography with a correlation mapping mask. J Biomed Opt 2014a;19:036010.

Choi WJ, Zhi Z, Wang RK. In vivo OCT microangiography of rodent iris. Opt Lett 2014b;39:2455.

Choma M, Sarunic M, Yang C, Izatt J. Sensitivity advantage of swept source and Fourier domain optical coherence tomography. Opt Express 2003;11:2183–9.

Cipolla MJ. The Cerebral Circulation. Colloq Ser Integr Syst Physiol From Mol to Funct 2009;1:1–59.

Clark S, Campbell F, Moore T, Jayson MIV, King TA, Herrick AL. Laser Doppler Imaging—A

New Technique for Quantifying Microcirculatory Flow in Patients with Primary Raynaud's Phenomenon and Systemic Sclerosis. Microvasc Res 1999;57:284–91.

Cobb MJ, Chen Y, Underwood RA, Usui ML, Olerud J, Li X. Noninvasive assessment of cutaneous wound healing using ultrahigh-resolution optical coherence tomography. J Biomed Opt International Society for Optics and Photonics; 2006;11:064002.

Cracowski J-L, Minson CT, Salvat-Melis M, Halliwill JR. Methodological issues in the assessment of skin microvascular endothelial function in humans. Trends Pharmacol Sci 2006;27:503–8.

Cutolo M, Grassi W, Matucci Cerinic M. Raynaud's phenomenon and the role of capillaroscopy. Arthritis Rheum Wiley Subscription Services, Inc., A Wiley Company; 2003;48:3023–30.

Denk W, Delaney KR, Gelperin A, Kleinfeld D, Strowbridge BW, Tank DW, et al. Anatomical and functional imaging of neurons using 2-photon laser scanning microscopy. J Neurosci Methods 1994;54:151–62.

Drew PJ, Shih AY, Driscoll JD, Knutsen PM, Blinder P, Davalos D, et al. Chronic optical access through a polished and reinforced thinned skull. Nat Methods 2010;7:981–4.

Drexler W, Morgner U, Kärtner FX, Pitris C, Boppart S a, Li XD, et al. In vivo ultrahigh-resolution optical coherence tomography. Opt Lett 1999;24:1221–3.

Dziennis S, Qin J, Shi L, Wang RK. Macro-to-micro cortical vascular imaging underlies regional differences in ischemic brain. Sci Rep 2015;5:10051.

Frank S, H bner G, Breier G, Longaker MT, Greenhalgh DG, Werner S. Regulation of Vascular Endothelial Growth Factor Expression in Cultured Keratinocytes. J Biol Chem 1995;270:12607–13.

Gagnon L, Sakadžic S, Lesage F, Mandeville ET, Fang Q, Yaseen MA, et al. Multimodal reconstruction of microvascular-flow distributions using combined two-photon microscopy and Doppler optical coherence tomography. Neurophotonics 2015;2:015008.

Gambichler T, Orlikov A, Vasa R, Moussa G, Hoffmann K, Stücker M, et al. In vivo optical coherence tomography of basal cell carcinoma. J Dermatol Sci 2007;45:167–73.

van Gijn J, Kerr RS, Rinkel GJ. Subarachnoid haemorrhage. Lancet 2007;369:306–18.

Gill RW. Measurement of blood flow by ultrasound: Accuracy and sources of error. Ultrasound Med Biol 1985;11:625–41.

Girard MJA, Strouthidis NG, Ethier CR, Mari JM, MC L, IA S, et al. Shadow Removal and

Contrast Enhancement in Optical Coherence Tomography Images of the Human Optic Nerve Head. Investig Opthalmology Vis Sci The Association for Research in Vision and Ophthalmology; 2011;52:7738.

Gong P, McLaughlin RA, Liew YM, Munro PRT, Wood FM, Sampson DD. Assessment of human burn scars with optical coherence tomography by imaging the attenuation coefficient of tissue after vascular masking. J Biomed Opt 2013;19:21111.

González S, Swindells K, Rajadhyaksha M, Torres A. Changing paradigms in dermatology: confocal microscopy in clinical and surgical dermatology. Clin Dermatol 2003;21:359–69.

Greaves NS, Benatar B, Whiteside S, Alonso-Rasgado T, Baguneid M, Bayat A. Optical coherence tomography: a reliable alternative to invasive histological assessment of acute wound healing in human skin? Br J Dermatol 2014;170:840–50.

Harrison R V. Blood Capillary Distribution Correlates with Hemodynamic-based Functional Imaging in Cerebral Cortex. Cereb Cortex 2002;12:225–33.

Holmstrom STS, Baran U, Urey H. MEMS Laser Scanners: A Review. J Microelectromechanical Syst 2014;23:259–75.

Holtmaat A, Bonhoeffer T, Chow DK, Chuckowree J, De Paola V, Hofer SB, et al. Long-term, high-resolution imaging in the mouse neocortex through a chronic cranial window. Nat Protoc 2009;4:1128–44.

Holtmaat A, de Paola V, Wilbrecht L, Trachtenberg JT, Svoboda K, Portera-Cailliau C. Imaging Neocortical Neurons through a Chronic Cranial Window. Cold Spring Harb Protoc 2012;2012:pdb.prot069617 – pdb.prot069617.

Hossmann K-A. Pathophysiology and Therapy of Experimental Stroke. Cell Mol Neurobiol 2006;26:1055–81.

Huang D, Swanson E, Lin C, Schuman J, Stinson W, Chang W, et al. Optical coherence tomography. Science (80-) 1991a;254:1178–81.

Huang D, Swanson EA, Lin CP, Schuman JS, Stinson WG, Chang W, et al. Optical coherence tomography. Science (80-) 1991b;254:1178–81.

Jia Y, Alkayed N, Wang RK. Potential of optical microangiography to monitor cerebral blood perfusion and vascular plasticity following traumatic brain injury in mice in vivo. J Biomed Opt 2009;14:040505.

Jia Y, An L, Wang RK. Label-free and highly sensitive optical imaging of detailed

microcirculation within meninges and cortex in mice with the cranium left intact. J Biomed Opt 2010;15:030510.

Jia Y, Grafe MR, Gruber A, Alkayed NJ, Wang RK. In vivo optical imaging of revascularization after brain trauma in mice. Microvasc Res Elsevier B.V.; 2011a;81:73–80.

Jia Y, Li P, Wang RK. Optical microangiography provides an ability to monitor responses of cerebral microcirculation to hypoxia and hyperoxia in mice. J Biomed Opt 2011b;16:096019.

Jia Y, Tan O, Tokayer J, Potsaid B, Wang Y, Liu JJ, et al. Split-spectrum amplitude-decorrelation angiography with optical coherence tomography. Opt Express 2012;20:4710–25.

Jia Y, Wang RK. Label-free in vivo optical imaging of functional microcirculations within meninges and cortex in mice. J Neurosci Methods 2010;194:108–15.

Jia Y, Wang RK. Optical micro-angiography images structural and functional cerebral blood perfusion in mice with cranium left intact. J Biophotonics 2011;4:57–63.

Johanson CE, Duncan JA, Klinge PM, Brinker T, Stopa EG, Silverberg GD. Multiplicity of cerebrospinal fluid functions: New challenges in health and disease. Cerebrospinal Fluid Res 2008;5:10.

Johnson KE, Wilgus TA. Multiple Roles for VEGF in Non-Melanoma Skin Cancer: Angiogenesis and Beyond. J Skin Cancer 2012;2012:1–6.

Jonathan E, Enfield J, Leahy MJ. Correlation mapping method for generating microcirculation morphology from optical coherence tomography (OCT) intensity images. Vol. 4, Journal of Biophotonics 2011. p. 583–7.

Jones EG. On the mode of entry of blood vessels into the cerebral cortex. J Anat 1970;106:507–20.

Kawauchi S, Sato S, Uozumi Y, Nawashiro H, Ishihara M, Kikuchi M. Light-scattering signal may indicate critical time zone to rescue brain tissue after hypoxia. J Biomed Opt 2011;16:027002.

Kim DY, Fingler J, Werner JS, Schwartz DM, Fraser SE, Zawadzki RJ. In vivo volumetric imaging of human retinal circulation with phase-variance optical coherence tomography. BiomedOptExpress 2011;2:1504–13.

Kittler H, Pehamberger H, Wolff K, Binder M. Diagnostic accuracy of dermoscopy. Lancet

Oncol 2002;3:159–65.

Kleinfeld D, Mitra PP, Helmchen F, Denk W. Fluctuations and stimulus-induced changes in blood flow observed in individual capillaries in layers 2 through 4 of rat neocortex. Proc Natl Acad Sci U S A 1998;95:15741–6.

Koizumi J, Yoshida Y, Nakazawa T, Ooneda G. Experimental studies of ischemic brain edema. Nosotchu 1986;8:1–8.

Kos S, Haueisen H, Lachmund U, Roeren T. Lymphangiography: Forgotten Tool or Rising Star in the Diagnosis and Therapy of Postoperative Lymphatic Vessel Leakage. Cardiovasc Intervent Radiol Springer-Verlag; 2007;30:968–73.

Krichevsky O, Bonnet G. Fluorescence correlation spectroscopy: the technique and its applications. Reports Prog Phys 2002;65:251–97.

Kuc R. Clinical Application of an Ultrasound Attenuation Coefficient Estimation Technique for Liver Pathology Characterization. IEEE Trans Biomed Eng IEEE; 1980;BME-27:312–9.

Kumagai K, Koike H, Nagaoka R, Sakai S, Kobayashi K, Saijo Y. High-Resolution Ultrasound Imaging of Human Skin In Vivo by Using Three-Dimensional Ultrasound Microscopy. Vol. 38, Ultrasound in Medicine & Biology 2012.

Kurokawa K, Sasaki K, Makita S, Hong Y-J, Yasuno Y. Three-dimensional retinal and choroidal capillary imaging by power Doppler optical coherence angiography with adaptive optics. Opt Express 2012;20:22796.

Lee ES, Kim TS, Kim S-K, Vorst J van der, Schaafsma B, Hutteman M, et al. Current Status of Optical Imaging for Evaluating Lymph Nodes and Lymphatic System. Korean J Radiol 2015;16:21.

Lee J, Jiang JY, Wu W, Lesage F, Boas D a. Statistical intensity variation analysis for rapid volumetric imaging of capillary network flux. Biomed Opt Express 2014;5:1160–72.

Lee J, Wu W, Lesage F, Boas D a. Multiple-capillary measurement of RBC speed, flux, and density with optical coherence tomography. J Cereb blood flow Metab Off J Int Soc Cereb Blood Flow Metab Nature Publishing Group; 2013;1–4.

Leitgeb R, Hitzenberger CK, Fercher AF. Performance of fourier domain vs. time domain optical coherence tomography. Opt Express 2003;11:889–94.

Li Y, Baran U, Wang RK. Application of thinned-skull cranial window to mouse cerebral blood flow imaging using optical microangiography. PLoS One 2014;9.

Liebeskind DS. Collateral Circulation. Stroke 2003;34:2279–84.

Liu G, Jia W, Nelson JS, Chen Z. In vivo, high-resolution, three-dimensional imaging of port wine stain microvasculature in human skin. Lasers Surg Med 2013;45:628–32.

Liu G, Lin AJ, Tromberg BJ, Chen Z. A comparison of Doppler optical coherence tomography methods. Biomed Opt Express 2012;3:2669–80.

Liu N-F, Lu Q, Jiang Z-H, Wang C-G, Zhou J-G. Anatomic and functional evaluation of the lymphatics and lymph nodes in diagnosis of lymphatic circulation disorders with contrast magnetic resonance lymphangiography. J Vasc Surg 2009;49:980–7.

Lizzi FL, Ostromogilsky M, Feleppa EJ, Rorke MC, Yaremko MM. Relationship of Ultrasonic Spectral Parameters to Features of Tissue Microstructure. IEEE Trans Ultrason Ferroelectr Freq Control IEEE; 1987;34:319–29.

Longa EZ, Weinstein PR, Carlson S, Cummins R. Reversible middle cerebral artery occlusion without craniectomy in rats. Stroke 1989;20:84–91.

LUBACH D, LUDEMANN W, BERENS VON RAUTENFELD D. Recent findings on the angioarchitecture of the lymph vessel system of human skin. Br J Dermatol Blackwell Publishing Ltd; 1996;135:733–7.

Makita S, Hong Y, Yamanari M, Yatagai T, Yasuno Y. Optical coherence angiography. Opt Express 2006;14:7821–40.

Mariampillai A, Leung MKK, Jarvi M, Standish B a, Lee K, Wilson BC, et al. Optimized speckle variance OCT imaging of microvasculature. Opt Lett 2010;35:1257–9.

Martín JM, Rubio M, Bella R, Jordá E, Monteagudo C. Regresión completa de nevos melanocíticos: correlación clínica, dermatoscópica e histológica de una serie de 13 casos. Actas Dermosifiliogr 2012;103:401–10.

Martinez-Corral I, Olmeda D, Dieguez-Hurtado R, Tammela T, Alitalo K, Ortega S. In vivo imaging of lymphatic vessels in development, wound healing, inflammation, and tumor metastasis. Proc Natl Acad Sci National Acad Sciences; 2012;109:6223–8.

McCaslin AFH, Chen BR, Radosevich AJ, Cauli B, Hillman EMC. In vivo 3D morphology of astrocyte–vasculature interactions in the somatosensory cortex: implications for neurovascular coupling. J Cereb Blood Flow Metab 2011;31:795–806.

Menke NB, Ward KR, Witten TM, Bonchev DG, Diegelmann RF. Impaired wound healing. Clin Dermatol 2007;25:19–25.

Minson CT. Thermal provocation to evaluate microvascular reactivity in human skin. J Appl Physiol 2010;109:1239–46.

Mogensen M, Nürnberg BM, Forman JL, Thomsen JB, Thrane L, Jemec GBE. *In vivo* thickness measurement of basal cell carcinoma and actinic keratosis with optical coherence tomography and 20-MHz ultrasound. Br J Dermatol Blackwell Publishing Ltd; 2009;160:1026–33.

Morcos SK. Acute serious and fatal reactions to contrast media: our current understanding. Br J Radiol 2005;78:686–93.

Nakao Y, Itoh Y, Kuang T-Y, Cook M, Jehle J, Sokoloff L. Effects of anesthesia on functional activation of cerebral blood flow and metabolism. Proc Natl Acad Sci 2001;98:7593–8.

Nam AS, Chico-Calero I, Vakoc BJ. Complex differential variance algorithm for optical coherence tomography angiography. Biomed Opt Express 2014;5:3822.

Polom K, Murawa D, Rho Y, Nowaczyk P, Hünerbein M, Murawa P. Current trends and emerging future of indocyanine green usage in surgery and oncology. Cancer Wiley Subscription Services, Inc., A Wiley Company; 2011;117:4812–22.

Potsaid B, Baumann B, Huang D, Barry S, Cable AE, Schuman JS, et al. Ultrahigh speed 1050nm swept source/Fourier domain OCT retinal and anterior segment imaging at 100,000 to 400,000 axial scans per second. Opt Express 2010;18:20029–48.

Qin J, Jiang J, An L, Gareau D, Wang RK. In vivo volumetric imaging of microcirculation within human skin under psoriatic conditions using optical microangiography. Lasers Surg Med Wiley Subscription Services, Inc., A Wiley Company; 2011;43:122–9.

Qin W, Baran U, Wang R. Lymphatic response to depilation-induced inflammation in mouse ear assessed with label-free optical lymphangiography. Lasers Surg Med 2015;47:669–76.

Reif R, Baran U, Wang RK. Motion artifact and background noise suppression on optical microangiography frames using a naïve Bayes mask. Appl Opt 2014;53:4164.

Reif R, Qin J, An L, Zhi Z, Dziennis S, Wang R. Quantifying Optical Microangiography Images Obtained from a Spectral Domain Optical Coherence Tomography System. Int J Biomed Imaging 2012;2012:509783.

Ren H, Du C, Park K, Volkow ND, Pan Y. Quantitative imaging of red blood cell velocity invivo using optical coherence Doppler tomography. Appl Phys Lett 2012;100.

Roustit M, Millet C, Blaise S, Dufournet B, Cracowski JL. Excellent reproducibility of laser

speckle contrast imaging to assess skin microvascular reactivity. Microvasc Res 2010;80:505–11.

Schaffer CB, Friedman B, Nishimura N, Schroeder LF, Tsai PS, Ebner FF, et al. Two-Photon Imaging of Cortical Surface Microvessels Reveals a Robust Redistribution in Blood Flow after Vascular Occlusion. Corbetta M, editor. PLoS Biol 2006;4:e22.

Sevick-Muraca EM, Kwon S, Rasmussen JC, Jaffer F, Libby P, Weissleder R, et al. Emerging lymphatic imaging technologies for mouse and man. J Clin Invest American Society for Clinical Investigation; 2014;124:905–14.

Shi L, Qin J, Reif R, Wang RK. Wide velocity range Doppler optical microangiography using optimized step-scanning protocol with phase variance mask. J Biomed Opt 2013;18:106015.

Shih AY, Blinder P, Tsai PS, Friedman B, Stanley G, Lyden PD, et al. The smallest stroke: occlusion of one penetrating vessel leads to infarction and a cognitive deficit. Nat Neurosci 2012;16:55–63.

Shih AY, Friedman B, Drew PJ, Tsai PS, Lyden PD, Kleinfeld D. Active dilation of penetrating arterioles restores red blood cell flux to penumbral neocortex after focal stroke. J Cereb Blood Flow Metab 2009;29:738–51.

Siler DA, Gonzalez JA, Wang RK, Cetas JS, Alkayed NJ. Intracisternal Administration of Tissue Plasminogen Activator Improves Cerebrospinal Fluid Flow and Cortical Perfusion After Subarachnoid Hemorrhage in Mice. Transl Stroke Res 2014;5:227–37.

Smith V, Riccieri V, Pizzorni C, Decuman S, Deschepper E, Bonroy C, et al. Nailfold Capillaroscopy for Prediction of Novel Future Severe Organ Involvement in Systemic Sclerosis. J Rheumatol 2013;40:2023–8.

Srinivasan VJ, Atochin DN, Radhakrishnan H, Jiang JY, Ruvinskaya S, Wu W, et al. Optical coherence tomography for the quantitative study of cerebrovascular physiology. J Cereb Blood Flow Metab Nature Publishing Group; 2011;31:1339–45.

Srinivasan VJ, Jiang JY, Yaseen MA, Radhakrishnan H, Wu W, Barry S, et al. Rapid volumetric angiography of cortical microvasculature with optical coherence tomography. Opt Lett 2010a;35:43–5.

Srinivasan VJ, Mandeville ET, Can A, Blasi F, Climov M, Daneshmand A, et al. Multiparametric, Longitudinal Optical Coherence Tomography Imaging Reveals Acute Injury and Chronic Recovery in Experimental Ischemic Stroke. PLoS One 2013a;8.

Srinivasan VJ, Mandeville ET, Can A, Blasi F, Climov M, Daneshmand A, et al. Multiparametric, Longitudinal Optical Coherence Tomography Imaging Reveals Acute Injury and Chronic Recovery in Experimental Ischemic Stroke. Georgakoudi I, editor. PLoS One Public Library of Science; 2013b;8:e71478.

Srinivasan VJ, Radhakrishnan H, Lo EH, Mandeville ET, Jiang JY, Barry S, et al. OCT methods for capillary velocimetry. Biomed Opt Express 2012;3:612.

Srinivasan VJ, Sakadžić S, Gorczynska I, Ruvinskaya S, Wu W, Fujimoto JG, et al. Quantitative cerebral blood flow with Optical Coherence Tomography. Opt Express 2010b;18:2477.

Stefanovic B, Hutchinson E, Yakovleva V, Schram V, Russell JT, Belluscio L, et al. Functional reactivity of cerebral capillaries. J Cereb Blood Flow Metab 2008a;28:961–72.

Stefanovic B, Hutchinson E, Yakovleva V, Schram V, Russell JT, Belluscio L, et al. Functional reactivity of cerebral capillaries. J Cereb Blood Flow Metab 2008b;28:961–72.

Stetter C, Hirschberg M, Nieswandt B, Ernestus R-I, Heckmann M, Sirén A-L. An experimental protocol for in vivo imaging of neuronal structural plasticity with 2-photon microscopy in mice. Exp Transl Stroke Med 2013;5:9.

Sulli A, Secchi ME, Pizzorni C, Cutolo M. Scoring the nailfold microvascular changes during the capillaroscopic analysis in systemic sclerosis patients. Ann Rheum Dis 2008;67:885–7.

Sun C, Sun H, Wu S, Lee CC, Akamatsu Y, Wang RK, et al. Conditional Ablation of Neuroprogenitor Cells in Adult Mice Impedes Recovery of Poststroke Cognitive Function and Reduces Synaptic Connectivity in the Perforant Pathway. J Neurosci 2013;33:17314–25.

Szu JI, Eberle MM, Reynolds CL, Hsu MS, Wang Y, Oh CM, et al. Thinned-skull Cortical Window Technique for In Vivo Optical Coherence Tomography Imaging. J Vis Exp 2012;

Tomlins PH, Wang RK. Theory, developments and applications of optical coherence tomography. J Phys D Appl Phys 2005;38:2519–35.

Tooke JE. Microvascular Function in Human Diabetes: A Physiological Perspective. Diabetes 1995;44:721–6.

Toriumi H, Tatarishvili J, Tomita M, Tomita Y, Unekawa M, Suzuki N. Dually Supplied T-Junctions in Arteriolo-Arteriolar Anastomosis in Mice: Key to Local Hemodynamic Homeostasis in Normal and Ischemic States? Stroke 2009;40:3378–83.

Tsai M-T, Chi T-T, Liu H-L, Chang F-Y, Yang C-H, Lee C-K, et al. Microvascular Imaging Using Swept-Source Optical Coherence Tomography with Single-Channel Acquisition. Appl Phys Express 2011;4:097001.

Vakoc BJ, Lanning RM, Tyrrell J a, Padera TP, Bartlett L a, Stylianopoulos T, et al. Three-dimensional microscopy of the tumor microenvironment in vivo using optical frequency domain imaging. Nat Med 2009a;15:1219–23.

Vakoc BJ, Lanning RM, Tyrrell JA, Padera TP, Bartlett LA, Stylianopoulos T, et al. Three-dimensional microscopy of the tumor microenvironment in vivo using optical frequency domain imaging. Nat Med Nature Publishing Group; 2009b;15:1219–23.

Vermeer KA, Mo J, Weda JJA, Lemij HG, de Boer JF. Depth-resolved model-based reconstruction of attenuation coefficients in optical coherence tomography. Biomed Opt Express 2014;5:322.

Wang H, Baran U, Li Y, Qin W, Wang W, Zeng H, et al. Does optical microangiography provide accurate imaging of capillary vessels?: validation using multiphoton microscopy. J Biomed Opt 2014;19:106011.

Wang RK. Signal degradation by multiple scattering in optical coherence tomography of dense tissue: a Monte Carlo study towards optical clearing of biotissues. Phys Med Biol 2002;47:307.

Wang RK, An L. Doppler optical micro-angiography for volumetric imaging of vascular perfusion in vivo. Opt Express 2009;17:8926–40.

Wang RK, An L, Francis P, Wilson DJ. Depth-resolved imaging of capillary networks in retina and choroid using ultrahigh sensitive optical microangiography. Opt Lett Osa; 2010;35:1467–9.

Wang RK, Hurst S. Mapping of cerebro-vascular blood perfusion in mice with skin and skull intact by Optical Micro-AngioGraphy at 13μm wavelength. Opt Express 2007;15:11402.

Wang RK, Jacques SL, Ma Z, Hurst S, Hanson SR, Gruber A. Three dimensional optical angiography. Opt Express 2007a;15:4083–97.

Wang RK, Jacques SL, Ma Z, Hurst S, Hanson SR, Gruber A. Three dimensional optical angiography. Opt Express Osa; 2007b;15:4083–97.

Wang RK, Ma Z. Real-time flow imaging by removing texture pattern artifacts in spectral-domain optical Doppler tomography. Opt Lett 2006;31:3001–3.

Wang Y, Wang R. Autocorrelation optical coherence tomography for mapping transverse particle-flow velocity. Opt Lett 2010;35:3538–40.

Wang Y, Wang RK. Measurement of particle concentration in flow by statistical analyses of optical coherence tomography signals. Opt Lett 2011;36:2143–5.

Wieser W, Draxinger W, Klein T, Karpf S, Pfeiffer T, Huber R. High definition live 3D-OCT in vivo: design and evaluation of a 4D OCT engine with 1 GVoxel/s. Biomed Opt Express 2014;5:2963.

Wojtkowski M, Srinivasan V, Ko T, Fujimoto J, Kowalczyk A, Duker J. Ultrahigh-resolution, high-speed, Fourier domain optical coherence tomography and methods for dispersion compensation. Opt Express 2004;12:2404–22.

Xu C, Schmitt JM, Carlier SG, Virmani R. Characterization of atherosclerosis plaques by measuring both backscattering and attenuation coefficients in optical coherence tomography. J Biomed Opt International Society for Optics and Photonics; 2008;13:034003.

Yano K, Kajiya K, Ishiwata M, Hong Y-K, Miyakawa T, Detmar M. Ultraviolet B-induced skin angiogenesis is associated with a switch in the balance of vascular endothelial growth factor and thrombospondin-1 expression. J Invest Dermatol 2004;122:201–8.

You J, Du C, Volkow ND, Pan Y. Optical coherence Doppler tomography for quantitative cerebral blood flow imaging. Biomed Opt Express 2014;5:3217.

Yousefi S, Qin J, Zhi Z, Wang RK. Uniform enhancement of optical micro-angiography images using Rayleigh contrast-limited adaptive histogram equalization. Quant Imaging Med Surg 2013;3:5–17.

Yousefi S, Wang RK. Simultaneous estimation of bidirectional particle flow and relative flux using MUSIC-OCT: phantom studies. Phys Med Biol 2014;59:6693–708.

Yousefi S, Zhi Z, Wang RK. Eigendecomposition-Based Clutter Filtering Technique for Optical Microangiography. IEEE Trans Biomed Eng Ieee; 2011;58:2316–23.

Yousefi S, Zhongwei Zhi Z, Wang RK. Label-Free Optical Imaging of Lymphatic Vessels Within Tissue Beds IN VIVO. IEEE J Sel Top Quantum Electron IEEE; 2014;20:15–24.

Yu L, Nguyen E, Liu G, Choi B, Chen Z. Spectral Doppler optical coherence tomography imaging of localized ischemic stroke in a mouse model. J Biomed Opt 2010;15:066006.

Yun SH, Tearney G, de Boer J, Bouma B. Motion artifacts in optical coherence tomography with frequency-domain ranging. Opt Express 2004;12:2977–98.

Zhang A, Zhang Q, Chen C-L, Wang RK. Methods and algorithms for optical coherence tomography-based angiography: a review and comparison. J Biomed Opt 2015;20:100901.

VITA

Utku Baran received the B.Sc. and M.Sc. degrees in electrical engineering from Koc University, Istanbul/Turkey, in 2010 and 2012, respectively. He received his Ph.D. in electrical engineering from University of Washington, Seattle/USA, in 2016, working under supervision of Prof. Ruikang Wang. He is the author/co-author of more than 20 journal articles, and the co-inventor of 2 pending and 1 granted US patents. His research interests include MEMS, OCT, biomedical optics, dermatology and neuroscience. He is a recipient of multiple awards, including College of Engineering Award for Research, SPIE Optics and Photonics Education Scholarship, and Newport Research Excellence Travel Award.